Development of CRONE reset control

Y.Y.L. Chen

Master of Science Thesis

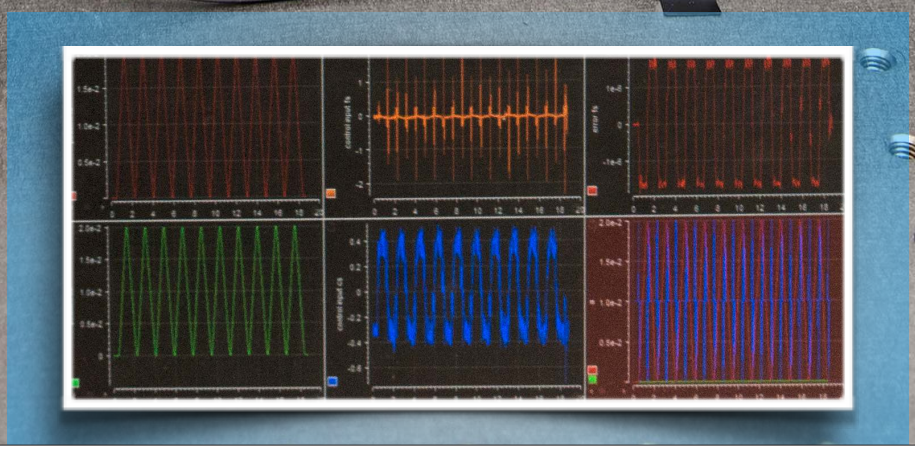

TU Delft Delft University of Technology

Delft Center for Systems and Control

Challenge the future

Development of CRONE reset control

by

Y.Y.L. Chen

to obtain the degree of Master of Science at the Delft University of Technology,
to be defended publicly on Tuesday October 17, 2017 at 10:00 AM.

Student number:	4176820	
Date:	October 3, 2017	
Thesis committee:	Dr. ir. N. Saikumar	TU Delft, co-supervisor
	Dr. ir. S.H. HosseinNia,	TU Delft, supervisor
	Dr. ir. S. Baldi	TU Delft, MSc Thesis advisor
	Dr. ir. J.W. Van Wingerden	TU Delft, chairman

TU Delft

Summary

In high-tech industry (sub)nanometre precision motion control is essential. For example wafer scanners, used for production of integrated circuits, have to provide (sub)nanometre precision positioning whilst satisfying challenging requirements on speed at the same time. It is in demanding cases like this that different requirements begin to conflict with each other. A fundamental trade-off between robustness and performance exists as an inevitable result of the waterbed effect in linear control. PID controllers, which have been an industry-standard for many years, do not satisfy the ever increasing demands.

In this MSc thesis a novel reset control synthesis method is proposed: CRONE reset control, which combines a robust fractional CRONE controller (Commande Robuste d'Ordre Non-Entier) with non-linear reset control to overcome waterbed effect. In CRONE control, robustness is achieved against gain deviations by creation of constant phase behaviour around bandwidth with the use of fractional operators. The use of fractional operators also introduces more freedom in shaping the open-loop frequency response, allowing fractional factors in Bode's gain-phase relation. However, waterbed effect remains, which motivates introduction of non-linear reset control in the CRONE design. In reset control, controller states are reset when the error between output- and reference- signal is zero. In frequency domain, using describing function analysis it is predicted that reset filters generate less phase lag for similar gain behaviour. For instance, a reset integrator gives a phase lag of about 38 degrees, which is 52 degrees less compared to the linear integrator. This allows for relief from Bode's gain-phase relation, breaking aforementioned trade-offs.

In the new controller design, reset phase advantage is approximated using describing function analysis and used to achieve better open-loop shape. New design rules for CRONE reset control have been developed in this thesis. Three different reset control strategies have been investigated: integrator reset, lag reset and lead-lag/lag-lead reset. For these controllers, a two-degree-of-freedom non-linearity tuning CRONE reset control structure has been developed. This control structure has been implemented digitally within a MATLAB/Simulink environment and implemented on a Lorentz-actuated (dual) precision stage via a real-time dSPACE DS1103 controller interface. For the implemented controllers sufficient quadratic stability has been shown using the H_β-condition.

It has been shown that simulated frequency responses using describing function correspond well to experimental identified frequency responses. Moreover, frequency domain measurements have shown that better performance for CRONE reset control can be achieved for same phase margin compared to linear CRONE. Relief from both

waterbed effect and Bode's gain-phase relation has been accomplished. Furthermore, for the same bandwidth, average noise reduction between 1.79 dB and 3.93 dB has been attained at a number of distinct frequencies above bandwidth. Some challenges still remain. Step disturbances in the CRONE reset controlled system caused secondary peaks, which showed to be able to demote settling times. For Gaussian disturbances no conclusive remark could be given as the cumulative power spectral density (CPSD) of the output position showed no correlation between disturbance rejection performance and increasing non-linearity in the CRONE reset control design. The topic of disturbance rejection thus requires further research.

In the fine stage separately and also in dual stage configuration, tracking of a fourth-order input-shaped reference signal (with second-order- and fourth-order feedforward respectively) showed improvement in CRONE reset control compared to linear CRONE. In the dual stage configuration, after decoupling fine stage and coarse stage, tracking performance of a linear CRONE controller has been compared to a CRONE reset controller. In both cases the same linear CRONE-2 controller with a bandwidth of 80 Hz and phase margin of 50° was applied to the coarse stage. On the fine stage a CRONE-1 lag-lead controller was applied with a bandwidth of 150 Hz and a phase margin of 55°. RMS error for a triangular scanning wave with maximal acceleration of $0.25\,\mathrm{m/s^2}$ and maximal velocity of 75 mm/s over a stroke of 2 cm, was reduced from 929.8 nm to 443.7 nm.

Preface

This report is the final part of the MSc Systems and Control program at the Delft University of Technology: the result of a challenging and exciting graduation period at the department of Precision and Microsystems Engineering (PME). At PME I received the opportunity to apply knowledge gained in the first year of the Systems and Control master in practice. During this time, I have not only learned about scientific research, writing, presenting and engineering in general, but even more importantly about sharing ideas, learning by doing and not to be afraid of making mistakes. I am thankful that I was encouraged and challenged to be part of the "PME experience", that hosts many passionate, inspiring and supportive people. This work could never have been realized without the help of following people, who I want to thank in particular:

Niranjan Saikumar, for your infinite source of patience, the innumerable times you provided a helping hand when needed and the positive vibe that you brought to every single meeting. Your insights have been invaluable.

Hassan HosseinNia, for your amazing support and encouragements: your excitement and enthusiasm for every small step made along the way has been a huge motivation. Thank you for always being willing to free time, when possible, to provide me with the most thorough feedback. Without your guidance and expertise we would not have gotten the results we got. The freedom that you gave me in shaping and structuring my thesis work has been amazing.

Simone Baldi, for sharing your utmost helpful and always honest opinions. The eye for detail you have while correcting work has really improved the works I have written. I am very grateful for the given advices and the given liberty during the project. Also the encouragements to do more of the practical work that I liked has made the project a pleasant experience.

Jo Spronck, for encouraging me to always take responsibility and be proactive. The open environment that you create with your wide collection of jokes and the passion you have for teaching students the ins and outs of engineering is truly inspiring.

All the graduate(d) students, PhDs, postdocs and staff members at PME
Andres, Arjan, Arnoud, Gijs, Joost, Jordan, Kars, Len, Mark, Mirte, Nils, Qi, Raoul, Silvan, Wan, Wouter (and some I might forgot to mention), thank you for all the

remarks and contributions to the discussions. Bart, for taking the time to give a splendid introduction to dSPACE and getting me familiarized with the setup. Arun, for the easy communication in planning time-slots to use the setup and the moments that we worked together on the setup. Rob, Patrick and Harry, thank you for providing all necessary means that allowed me to run the practical experiments successfully.

My dear friends and fellow students

Bart, for the endless support, many fancy cooking moments and trilogies watched throughout the years. Gokul and Ronald, for always being prepared to try and relieve stress by any means possible. All of you, Atindriyo, Bingyu, Nikolaos, Peter, Ruben, Valentina, William and Wouter for every activity we did with the "Thesis Motivation Group". It has been a great encouragement to get through thesis time together, regardless whether we were working, lunching together or doing sports/karoaoke (which is also a kind of sport). Irene, Iris, Mariska, Niels, for the delightful coffee breaks, enjoyable lunches and dinners during this time.

My family

My lovely sisters, Sophia and Alida, you have supported me through every step of the way. Thank you for believing in me whenever I could not. My uncle, Yun Li, for encouraging me to be curious and courageous to learn new things. Finally, my parents, for their endless and loving support. 爸爸，妈妈，多谢你们一直以来对我的关心，一直的支持，鼓励，帮助。

Y.Y.L. Chen
Delft, October 2017

" Nothing in life is to be feared, it is only to be understood. Now is the time to understand more, so that we may fear less." — *Marie Curie*

Contents

1
Introduction

In this chapter, an introductory text is given that explains the motivation of this MSc thesis, leading towards the objective of the thesis. This chapter provides a technical overview of how a CRONE reset controller can achieve behaviour in terms of robustness and performance that cannot be realized using linear control. It is assumed that the reader is fairly acquainted with the topics of linear feedback control design and loop shaping methods. A summary of relevant notions within these topics can be found in Appendix A.

1.1. Introduction

In high-tech industry, (sub)nanometre precision positioning is essential. Examples where (sub)nanometre precision mechanisms play a significant role include: manufacturing processes of integrated circuits (IC) (shown in figure 1.1a), scanning of atomic force microscopes and printing of three-dimensional nano-structures. Improvement of aforementioned processes helps advancement in technology on the one hand, but can have huge socio-economic impact as well. Especially in the case of IC production, higher throughput allows for drastic cost savings on large scale, which in turn can decrease price per IC and make high-end electronic devices more affordable.

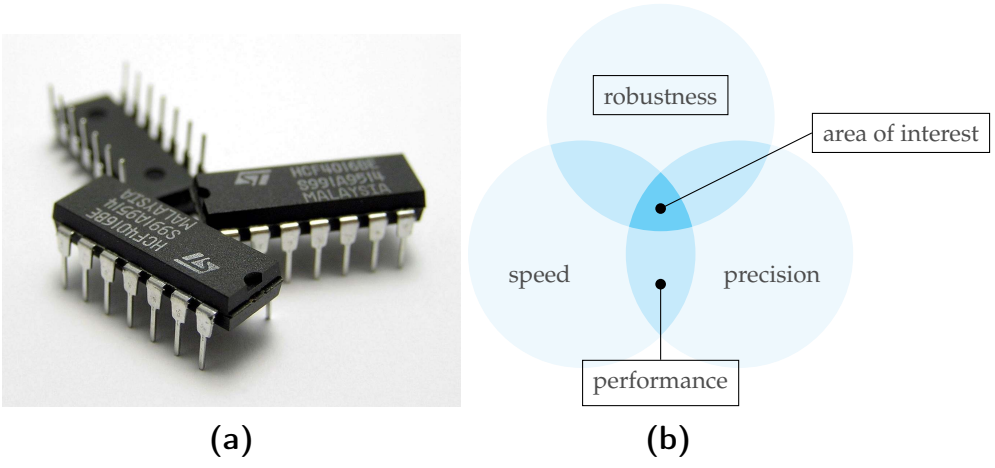

Figure 1.1: (a) ICs for which high precision positioning is essential in production [1]. (b) Venn diagram highlighting the area of interest in design of high precision positioning systems.

From a technical perspective, there are some challenges when going to (sub)nanometre scales. Environmental disturbances and noisy measurements start to play a larger and larger role. Often, this becomes problematic when also high demands exist on speed and thus bandwidth of the controlled system. Higher bandwidth inevitably increases high-frequency noise, thus degrading precision.

To complicate realization of a fast, (sub)nanometre positioning system even more, requirements on robustness have to be considered as well. As there are always deviations between practical systems and modelled plants, some room is left for modelling errors and changes in parameters. Ideally a system is robust against all of these deviations, leaving system performance unchanged in presence of irregularities. In practice, making a system more robust means that some concessions have to be made for precision and speed. These trade-offs are summarized in the Venn-diagram in figure 1.1b and are inevitable in conventional linear controllers.

To break aforementioned trade-offs, a novel robust non-linear fractional order reset controller, CRONE reset controller, is proposed. It combines the robust fractional order CRONE controller (*Commande Robuste d'Ordre Non-Entier*) as formalized by [2] with non-linear reset. Within control design, loop shaping methods are used for simplicity and intuitiveness.

Below a summary is given of the fundamental limits in linear control, then it is explained how fractional order control can provide more tunability in getting a better loop shape, followed by an introduction to reset control which can be used to break fundamental limits. Finally, the concept of CRONE reset control is introduced as a way of combining tunability and non-linearity to get a robustness and performance trade-off that cannot be attained using linear control.

1.1.1. Fundamental limits in linear control

Approximate Bode gain-phase relation

Taking the open loop $L(j\omega)$, assuming it is minimum-phase (all zeros and poles in the left half plane), a relation exists between its phase and slope of its gain curve:

$$\arg\Big(L(j\omega)\Big) \approx \frac{\pi}{2} n(j\omega) \tag{1.1}$$

where the slope $n(j\omega)$ is defined as:

$$n(j\omega) = \frac{d \log |L(j\omega)|}{d \log \omega} \tag{1.2}$$

Additional phase around bandwidth leads to a more robust system, but inevitably raises open-loop gain slope for this range of frequencies, creating lower open-loop gain at low frequency and higher open-loop gain at high frequency. This is depicted in figure 1.2. As modulus margin increases for the open-loop response with additional phase around bandwidth $L^*(j\omega)$, this system is more robust. However, the price for

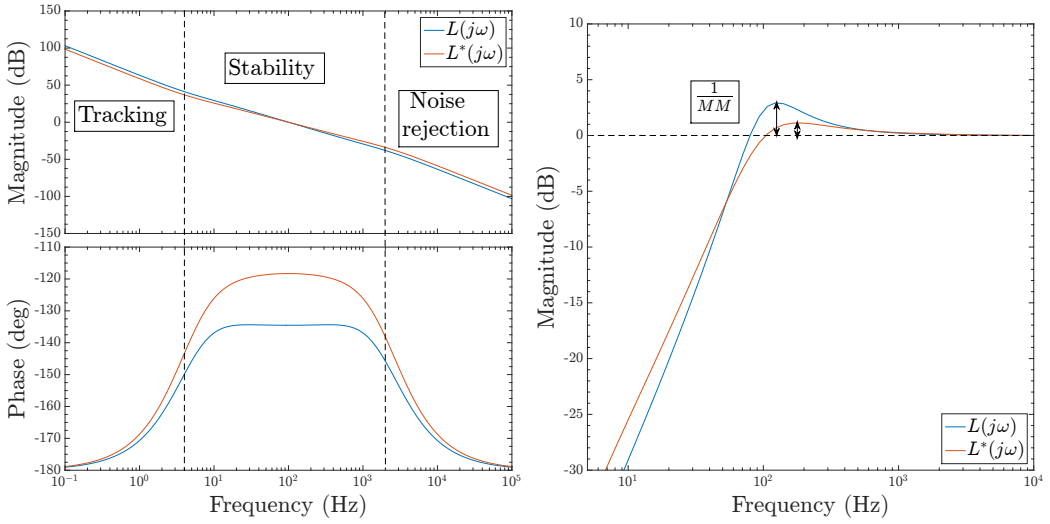

Figure 1.2: (a) Open-loop response $L(j\omega)$ showing three regions that determine system properties in terms of: reference-tracking, stability and noise rejection. In open-loop response $L^*(j\omega)$ more phase is added around bandwidth leading to larger modulus margin MM in (b)corresponding sensitivity function $S(j\omega)$ but degrading tracking and noise rejection performance.

additional robustness is poorer tracking, disturbance rejection and noise attenuation performance: this is the robustness performance trade-off addressed in this thesis.

Relation between sensitivity and complementary sensitivity function

The constraint between sensitivity function $S(j\omega)$ and complementary $T(j\omega)$ is described by:

$$S(j\omega) + T(j\omega) = 1, \forall\omega \tag{1.3}$$

As $S(j\omega)$ is the transfer of noise to output and $T(j\omega)$ is the transfer of reference to output, from (1.3) one can deduce that design of $S(j\omega)$ and $T(j\omega)$ is inevitably an intertwined process. If the design target is to decrease the value of complementary sensitivity peak for example, as a result the noise sensitivity will increase in the same frequency region.

Waterbed effect

Noise transfer in a system can be described by its sensitivity function. The sensitivity function is given in terms of open loop by the equation:

$$S(j\omega) = \frac{1}{1 + L(j\omega)} \tag{1.4}$$

Tuning the open-loop therefore can alter system noise performance. Bode's sensitivity integral puts a quantitative constraint on achievable performance, given by:

$$\int_0^\infty \ln|S(j\omega)|d\omega = \pi \sum_k \mathrm{Re}(p_k) - \frac{\pi}{2} \lim_{s\to\infty} sL(s) \tag{1.5}$$

in which p_k are the RHP poles of $L(s)$. When there are no RHP poles and relative degree of $L(s) \geq 2$ then this constraint simplifies to:

$$\int_0^\infty \ln|S(j\omega)|d\omega = 0 \tag{1.6}$$

This integral implies that if the noise transfer is decreased within one frequency range, it has to increase within another. This is called the waterbed effect. As a more robust system is realized when a smaller maximum sensitivity peak is present, which means that the sensitivity has to increase at other frequencies. If sensitivity increases at low frequences, complementary sensitivity function decreases given the relation in (1.3), reducing disturbance rejection and degrading reference tracking accuracy. On the other hand, if sensitivity increases at high frequencies, noise attenuation will become worse.

1.1.2. Tunability with fractional order control

The slope in Bode's gain-phase relation $n(j\omega)$ can take on integer values for integer order controllers lik the industry-standard PID controller. Fractional order controllers on the other hand, allow for more freedom: instead of integer values, they can be fractional as well. Let us consider a fractional integrator $s^{-\nu}$ with fractional order $\nu \in [0,1] \cap \mathbb{R}$. Tt means that slopes of $-\nu 20\mathrm{dB/decade}$ and phases of $-\nu\frac{\pi}{2}\mathrm{rad}$ can be achieved. This can be observed in figure 1.3. Fractional order control gives more freedom in shaping open-loop compared to integer order control. This tunability is used in the CRONE design methodology through which robust fractional order controllers can be designed. However, as fractional order controllers also belong to the class of linear controllers, fundamental limits in linear control remain.

1.1.3. Non-linear reset control

After introducing the basics of reset control, it is shown how a reset controller overcomes fundamental limitations of linear controllers.

Reset control

In reset control, controller states are reset if a certain reset condition is satisfied. A common reset condition is when the error signal is zero; $e(t) = 0$. Consider a sinusoidal error signal $e(t) = \sin(\omega t)$, controller $C(s) = \frac{1}{s}$ and controller state being reset with the zero-error reset condition. In figure 1.4 it can be seen that the controller state is reset to zero at every zero-crossing of the error. This reset

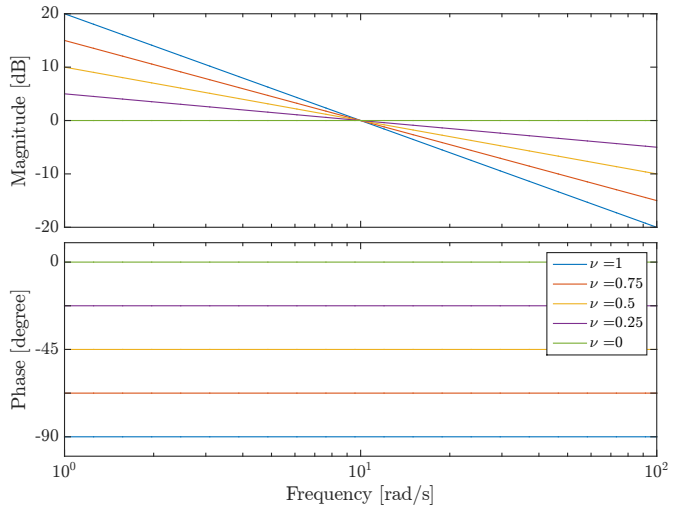

Figure 1.3: Frequency response of $C(s) = \left(\frac{\omega_{cg}}{s}\right)^{\nu}$ with $\nu \in [0,1]$ for $\omega_{cg} = 10\text{rad/s}$.

integrator is also known as Clegg integrator (CI) and can be described by following impulsive differential equation:

$$\begin{cases} \dot{u}(t) = e(t) & \text{if } e(t) \neq 0, \\ u(t^+) = 0 & \text{if } e(t) = 0 \end{cases} \tag{1.7}$$

with $e(t)$ being the error signal and $u(t)$ the control input.

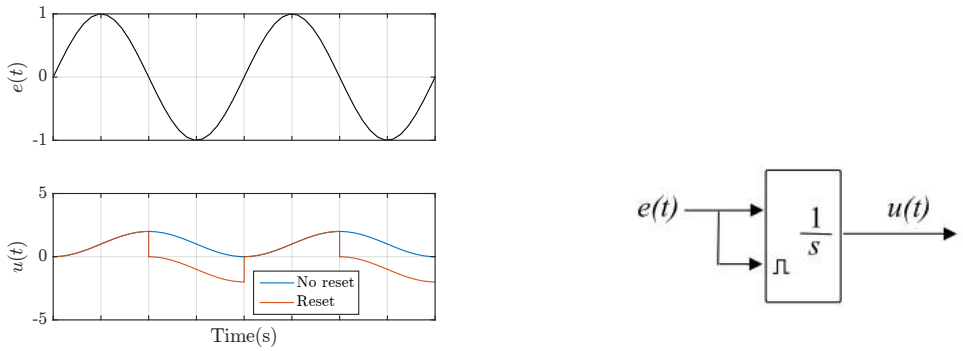

(a) **(b)**

Figure 1.4: Reset of integrator with error signal $e(t) = \sin(\omega t)$ and controller output $u(t)$ and reset condition $e(t) = 0$ (a) with and without reset. (b) Diagram of the control block of the reset integrator. Image courtesy of [3].

Describing function analysis shows less phase lag in reset systems

Describing function analysis can be used to approximate transfer from input to output of a non-linear system in frequency domain. Under the assumption that no

higher harmonics are induced in the system, the transfer is analysed using arbitrary sine input with frequency ω and amplitude E, given by:

$$x(t) = E\sin(\omega t). \tag{1.8}$$

System output is described by:

$$y(t) = f(E\sin(\omega t), t). \tag{1.9}$$

Mathematically, the describing function of a non-linear system can be expressed as in [4]:

$$K(E,\omega) = \frac{2}{TE}\int_0^T f(E\sin(\omega t), t)\{\sin(\omega t) + j\cos(\omega t)\}dt \tag{1.10}$$

where T is the period of the sine signal. Note that this essentially is the first coefficient of the Fourier Transform.

The describing function of a Clegg integrator is given by:

$$CI(j\omega) := \frac{1.62e^{-j38^\circ}}{\omega} = \frac{1.62}{j\omega}e^{j52^\circ} \tag{1.11}$$

which shows a 52 degree phase advantage with respect to a linear integrator.

The frequency response of a conventional integrator and of a Clegg integrator are depicted in figure 1.5. For a similar slope, the Clegg integrator gives less phase lag. This means that the reset integrator has a gain-phase relation that is not subjected to the fundamental Bode gain-phase relation. This beneficial gain-phase relation potentially contributes to improvements on the trade-off between robustness and performance fundamentally present in linear controllers.

1.1.4. CRONE reset control concept

CRONE control is a fractional order controller in which robustness against gain deviations is achieved by designing a flat phase behaviour around bandwidth. As a robust controller the system may under-perform in terms of tracking, disturbance rejection and noise attenuation because of fundamental trade-offs. This is where non-linear reset can be advantageous. The CRONE reset control concept can be described in three steps:

1. Design robust fractional CRONE controller
2. Add phase around bandwidth with non-linear reset
3. Retune open-loop slope around bandwidth to improve open-loop shape for same phase margin

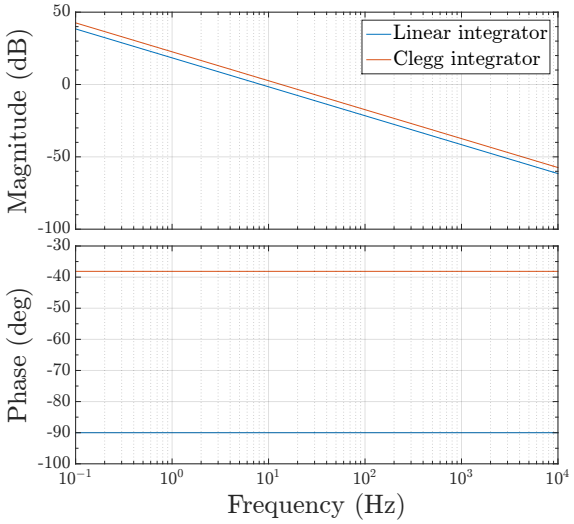

Figure 1.5: Frequency response of a conventional integrator and a Clegg integrator (using its describing function).

This is summarized in the open-loop frequency responses depicted in figure 1.6. Because phase lead can be created for almost similar gain, the open-loop shape can be improved. By having a new fractional order ν^* that is larger than ν, making the slope around bandwidth steeper, open-loop gain increases at low frequencies and open-loop gain decreases at high frequencies. In this way, with CRONE reset control a level of combined performance and robustness can be achieved that cannot be attained with linear control.

1.2. Research objective

In last section it became clear that CRONE reset control can potentially result in a robust and well-performing system, overcoming fundamental limitations in linear control. A methodology for CRONE reset control design is missing, which leads to the objective of this MSc Thesis:

Develop the CRONE reset control framework for a mechatronic system application.

The sub-objectives are threefold:

1. Design of a CRONE reset controller. This consists of a methodology of computing controller parameters that ensure stability margins and specifications.
2. Proof of stability.
3. Validation of the methodology on a mechatronic system.

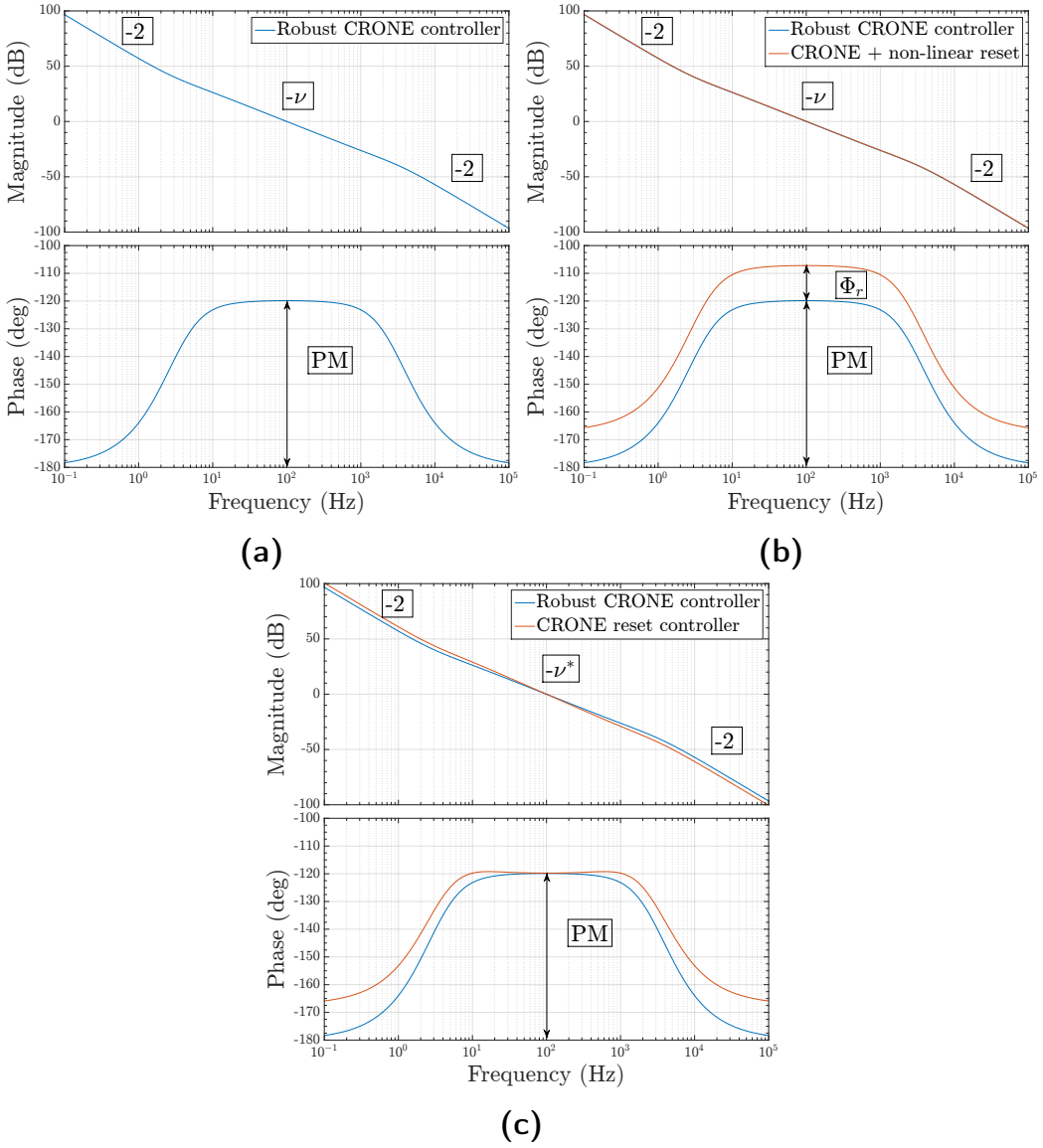

Figure 1.6: Frequency domain open-loop responses showing CRONE reset control concept. Open-loop with indication of open-loop slopes for (a) step 1: robust CRONE controller, (b) step 2: additional non-linear reset adds phase Φ_r, (c) step 3: improved open-loop shape with new fractional slope $\nu^* > \nu$.

1.3. Outline

This report is structured as follows: in chapter 2: State of the art the current state of the art CRONE control and reset control are introduced. Subsequently, the developed methodology for CRONE reset control design is given in chapter 3: CRONE reset control. This chapter is followed by a system overview of the experimental Lorentz-actuated precision stage in chapter 4: System overview. An introduction to

experimental methods and validated simulation method is presented in chapter 5: Methods. Then a preliminary comparison between different CRONE reset control strategies is provided in chapter 6: Preliminary reset strategy selection, using developed simulation methods and preliminary practical results. In chapter 7: Experimental validation: fine stage selected CRONE reset controllers are applied on the setup and performance with respect to reference-tracking, noise attenuation, disturbance rejection are investigated in both frequency- and time domain. Proceeding from this, a practical CRONE reset control design example for dual precision stage application is shown in chapter 8: Practical CRONE reset design: dual precision stage. Finally, a toolbox with design considerations is given in chapter 9: Toolbox and conclusions are given in chapter 10: Conclusion.

2

State of the art

This chapter gives an overview of current state of the art within CRONE control and reset control. An introduction to CRONE control and reset control will be given, followed by a summary of state of the art in both CRONE and reset control.

2.1. CRONE control

CRONE control is a robust fractional order control method that achieves robustness through creating flat phase behaviour around bandwidth. This can be seen in figure 2.1. If bandwidth frequency moves as a consequence of an inaccuracy in gain, the flat phase behaviour limits decrease of phase margin. In this way robustness against gain deviations is assured. Three generations of SISO CRONE control exist today. The controller definitions below are as introduced in [2]. Third generation CRONE is not realizable in practice and is therefore not discussed. In this thesis the focus is on first- and second generation CRONE.

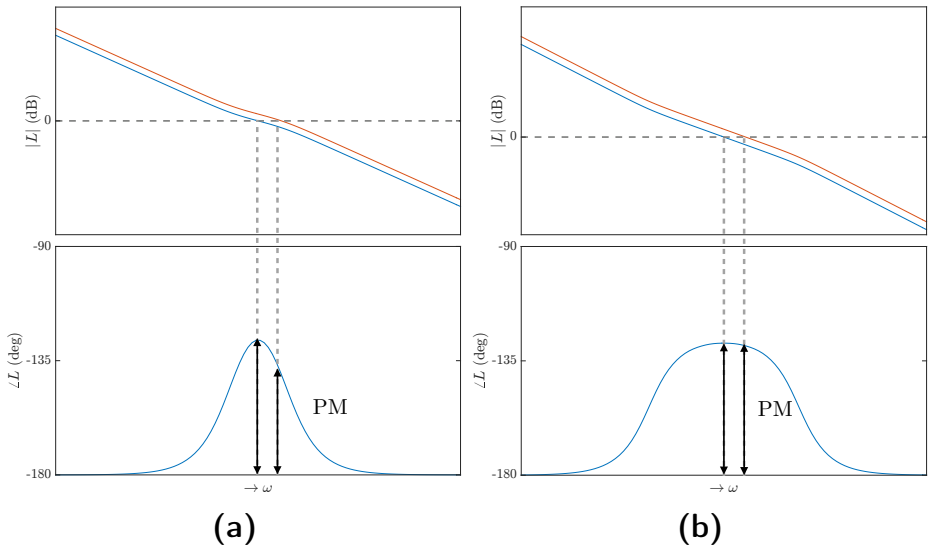

Figure 2.1: Bode plot of (a) common open-loop response and (b) open-loop under CRONE control. Flat phase around bandwidth provides robustness against gain deviations.

2.1.1. First generation CRONE

A first generation CRONE controller has a similar transfer function to an integer order series PID controller:

$$C_F(s) = C_0(1+\frac{\omega_I}{s})^{n_I}\left(\frac{1+\frac{s}{\omega_b}}{1+\frac{s}{\omega_h}}\right)^{\nu}\frac{1}{(1+\frac{s}{\omega_F})^{n_F}},\quad \nu\in\mathbb{R},\quad n_I,n_F\in\mathbb{N} \tag{2.1}$$

with ω_I and ω_F being the integrator- and low-pass filter corner frequencies, ω_b and ω_h the corner frequencies of the band-limited derivative action and ν the fractional order. The difference between a series integer order PID controller and a first generation CRONE controller is that order ν is fractional instead of integer, making first generation CRONE a fractional PID controller. The Bode plot of this controller can be found in figure 2.2. The controller can be implemented using an N-th order Oustaloup approximation of the middle term as:

$$C_F(s) = C_0(1+\frac{\omega_I}{s})^{n_I}\prod_{k=1}^{N}\left(\frac{1+\frac{s}{\omega_{k'}}}{1+\frac{s}{\omega_k}}\right)\frac{1}{(1+\frac{s}{\omega_F})^{n_F}} \tag{2.2}$$

where N is the order of approximation to approximate fractional filter in the frequency band between ω_b and ω_h. ω_k and ω'_k are corner frequencies chosen iteratively in the band $[\omega_b, \omega_h]$:

$$\omega'_{k+1} = \alpha\eta\omega'_k, \tag{2.3}$$
$$\omega_{k+1} = \alpha\eta\omega_k \tag{2.4}$$

and the initial corner frequencies are:

$$\omega_1 = \eta^{1/2}\omega_b, \tag{2.5}$$
$$\omega'_1 = \alpha\omega_1 \tag{2.6}$$

with α and η determined by the fractional order ν and approximation order N:

$$\nu = \frac{\log\alpha}{\log(\alpha\eta)}, \tag{2.7}$$
$$N = \frac{\log(\omega_h/\omega_b)}{\log(\alpha\eta)}. \tag{2.8}$$

The fractional order ν can be calculated from the required nominal phase margin M_Φ, bandwidth ω_{cg} and other available values:

$$\nu = \frac{-\pi + M_\Phi - \arg G(j\omega_{cg}) + n_F\arctan\frac{\omega_{cg}}{\omega_F} + n_I(\frac{\pi}{2}-\arctan\frac{\omega_{cg}}{\omega_I})}{\arctan\frac{\omega_{cg}}{\omega_b}-\arctan\frac{\omega_{cg}}{\omega_h}}. \tag{2.9}$$

C_0 can be determined using chosen values:

$$C_0 = \frac{\left(1 + \left(\frac{\omega_{cg}}{\omega_F}\right)^2\right)^{\frac{n_F}{2}}}{|G(j\omega_{cg})|\left(\frac{\omega_h}{\omega_b}\right)^{\frac{n}{2}}\left(1 + \left(\frac{\omega_I}{\omega_{cg}}\right)^2\right)^{\frac{n_I}{2}})}. \tag{2.10}$$

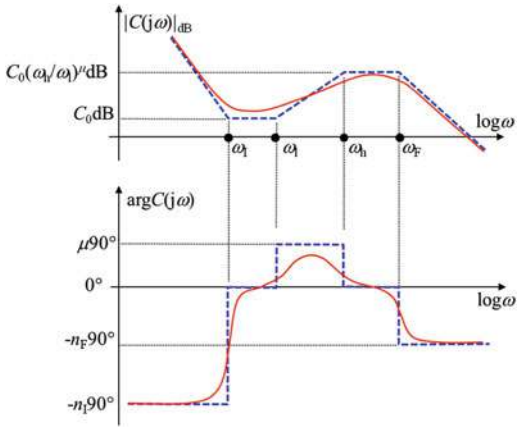

Figure 2.2: Bode plot of a PID$^\mu$ controller, similar to a First Generation CRONE controller described in (2.1)with $\nu = \mu$. Corner frequencies are marked in which lower derivative filter corner frequency $\omega_b = \omega_l$. Image courtesy of [2].

2.1.2. Second generation CRONE

Second generation CRONE can be applied to systems that do not have a flat phase behaviour in the region around bandwidth. The approach is such that a flat phase behaviour is created in the open-loop by using the inverse of the plant. The desired open-loop is determined by function $\beta_0(s)$:

$$\beta_0(s) = (\frac{\omega_{cg}}{s})^\nu, \quad \nu \in \mathbb{R} \cap [1,2] \tag{2.11}$$

where the order ν is again fractional. The approximated Second Generation CRONE controller including n_I-th order band-limited integrator and n_F-th order low-pass filter is given by:

$$\beta_0(s) = K(1 + \frac{\omega_I}{s})^{n_I}(\frac{1 + \frac{s}{\omega_b}}{1 + \frac{s}{\omega_h}})^{-\nu}\frac{1}{(1 + \frac{s}{\omega_F})^{n_F}}, \quad \nu \in \mathbb{R} \cap [1,2]. \tag{2.12}$$

The second generation CRONE controller finally has the following structure:

$$C_S(s) = G_0^{-1}(s)\beta_0(s). \tag{2.13}$$

Fractional order ν can be calculated using:

$$\nu = \frac{-\pi + M_\Phi + n_F \arctan\frac{\omega_{cg}}{\omega_F} + n_I(\frac{\pi}{2} - \arctan\frac{\omega_{cg}}{\omega_I})}{\arctan\frac{\omega_{cg}}{\omega_h} - \arctan\frac{\omega_{cg}}{\omega_b}} \tag{2.14}$$

and constant K is given by:

$$K = \frac{\left(1 + \frac{\omega_{cg}^2}{\omega_F^2}\right)^{\frac{n_F}{2}}}{\left(\frac{\omega_b}{\omega_h}\right)^{\frac{\nu}{2}}\left(1 + \frac{\omega_I^2}{\omega_{cg}^2}\right)^{\frac{n_I}{2}}}. \tag{2.15}$$

Furthermore, to have integral action and a strictly proper controller, n_I and n_F both have to be chosen at least larger than the plant asymptotes.

2.2. Reset control

A general reset controller can be described by the following impulsive differential equations, using the formalism in [3]:

$$\Sigma_r := \begin{cases} \dot{x}_r(t) = A_r x_r(t) + B_r e(t) & \text{if } e(t) \neq 0, \\ x_r(t^+) = A_\rho x_r(t) & \text{if } e(t) = 0, \\ u(t) = C_r x_r(t) + D_r e(t) \end{cases} \tag{2.16}$$

where matrices A_r, B_r, C_r, D_r are the base linear state-space matrices of the reset controller, $e(t)$ is the error between output and reference, $u(t)$ is the control input signal, $x_r(t)$ is the state with $x_r(t^+)$ being the after-reset state and A_ρ is the reset matrix. The reset condition in this structure is given by $e(t) = 0$ and full reset takes place when A_ρ is a null-matrix.

As in this thesis describing function is used for CRONE reset control design, only constant reset condition will be used. Other concepts that are relevant are introduced below: reset approaches, for which a summary is presented of reset control parameters, set-point regularization to get rid of limit cycles and time-regularization to avoid parasitic non-linear behaviour. Also the existence of higher harmonics is addressed.

2.2.1. Reset approaches

Partial reset

In partial reset the controller state(s) is/are not reset to zero, but to a fraction of the state value(s). Instead of A_ρ being a null-matrix, it can be taken as $A_\rho = \gamma I$ instead. Additionally, selected controller states can be reset, with $A_\rho = \text{diag}(\gamma I_{nr}, I_{nnr})$ with nr being the number of reset states and nnr being the number of non-reset states.

Reset percentage

In the PI+CI controller a convex combination is made between a linear integrator and a reset integrator. A measure of degree of non-linearity in the system is established using a reset percentage p_{reset}. The PI+CI structure can be seen in figure 2.3.

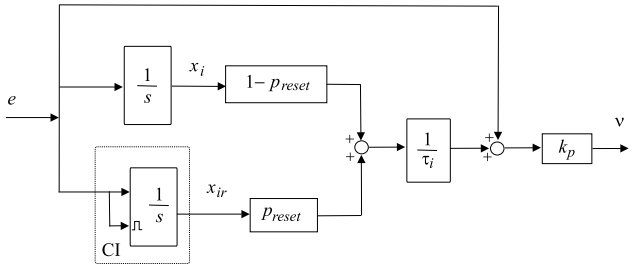

Figure 2.3: Block diagram of the PI+CI controller, adapted from [5].

Reset band

Because in a practical system noise is always present, a reset band can be introduced. This means that the reset condition is not $e(t) = 0$ but it changes into: $(e, \delta < 0 \cap \dot{e} > 0) \cup (e, \delta > 0 \cap \dot{e} < 0)$ with $\delta \in \mathbb{R}^+$. Only when the absolute error becomes smaller than δ, namely when the error enters the reset band, a reset takes place. This is depicted in figure 2.4. If the noise level of the measured quantity error is within this band no reset will occur.

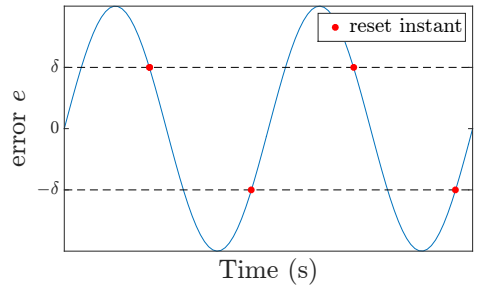

Figure 2.4: Error signal with reset band value δ. Resets are performed at entering of this band: in this figure marked by red dots.

2.2.2. Set-point regularization to prevent limit cycles

Integrators ensure zero steady-state error. In reset systems however, this property does not hold true [5]. In [6] it was shown that a feedforward controller with inverse plant DC-gain can be used to avoid limit cycles. Feedforward controller F is given

by:

$$F = \begin{cases} -\frac{1}{C_p A_p^{-1} B_p}, & \text{if } A_p \text{ is invertible} \\ 0, & \text{otherwise} \end{cases} \tag{2.17}$$

in which A_p, C_p, B_p are state-space matrices of the considered SISO plant (in which D-matrix is equal to zero).

This result can be shown using the final value theorem:

Theorem 1. *Final Value Theorem*

$$\lim_{s \to 0} sE(s) = \lim_{t \to \infty} e(t)$$

Consider a two-degree-of-freedom control diagram with feedforward controller $F(s)$ and feedback controller $C(s)$. The Laplace transform of the error $E(s)$ for plant $P(s)$ can be expressed as:

$$E(s) = R(s) - Y(s) \tag{2.18}$$

$$= R(s)\left(1 - \frac{P(s)(C(s) + F(s))}{1 + P(s)C(s)}\right) \tag{2.19}$$

$$= \frac{1}{s}\frac{1 - P(s)F(s)}{1 + P(s)C(s)}. \tag{2.20}$$

Then according to the final value theorem the error for time going to infinity becomes:

$$\lim_{t \to \infty} e(t) = \lim_{s \to 0} \frac{1 - P(s)F(s)}{1 + P(s)C(s)} \tag{2.21}$$

Zero steady-state error is achieved when the denominator at $s = 0$ is infinite, which is the case when the open loop $P(s)C(s)$ contains the excess integrator. Unsurprisingly, when the linear controller is replaced with a reset controller this condition does not hold. However, this analysis helps motivating the feedforward gain used in the set-point regulator in (eq:setregulator). As can be seen in (2.21), when $P(0)F(0) = 1$, the error signal goes to zero when time goes to infinity. Therefore, when $F(s)$ is chosen as $F(s) = 1/P(0)$, zero steady-state error can be achieved.

2.2.3. Time-regularization to avoid parasitic non-linear effects

Some parasitic behaviour might appear in non-linear systems such as deadlock, beating and and Zeno effects. In order to avoid these, time-regularization can be used [5]. This means that an additional reset condition is present: the duration between two consecutive reset instants has to be larger than an assigned time interval larger than zero. In practical applications this is always the case. Therefore named parasitic effects are neglected.

2.2.4. Higher harmonics induced by non-linearity

Discontinuities in control input can cause higher-order effects, that are disregarded in describing function analysis. The contribution of these harmonics may limit the achievable system performance, robustness and even stability of the system. As in most systems high frequencies are attenuated, this effect might be slightly weakened. Still it is necessary to be aware of the possible difficulties and problems that these discontinuities present to the control design.

2.3. Literature review

In separate research fields of fractional order control and reset control numerous works already exist.

In fractional order control, the additional degree of freedom in choosing fractional order allows for more tunability. With these fractional order operators, robustness can be achieved as is done in CRONE control. Because fractional order control is compatible with classical loop shaping methods, many applications of CRONE exist, such as in fields of: temperature control [7], [8], hydraulic/pneumatic systems [9], [10] and electro-mechanical systems [11], [12], [13] . To counter the fundamental trade-offs in linear control, several works address inclusion of non-linear control methods within CRONE, such as extension of CRONE to Linear Parameter-Varying systems (LPV systems)[14] and Linear Time-Periodic systems [15]. For fractional order control in general also methods of Sliding-mode control [16], reset control [17] and Model Reference Adaptive Control (MRAC) [18] have been explored. Another interesting topic within CRONE is third generation CRONE control, in which the fractional order is a complex number [2]. Theoretically a CRONE-3 controlled system is robust against plant uncertainties in both gain and phase. Although complex fractional order cannot be realized practically, some approximations in are investigated and applied in for instance [19] and [20].

One of the challenges in fractional order control is implementation. In continuous time, fractional order transfer functions require higher order approximation, like Oustaloup's recursive approximation [2] or continued fraction expansion approximation [21]. In discrete time, some direct- and indirect discretization schemes exist. A detailed summary of both continuous-time and discrete-time implementations can be found in [21]. As central processing units (CPUs) are becoming both faster and more affordable, use of fractional order controllers becomes increasingly more compelling.

In reset control, numerous works exist today with practical applications ranging from: hard-drive disk control [22], [23], positioning stages [24],[25] and process control [26],[27]. Reset control design and stability of reset systems remain actively researched topics. An interesting development is the PI+CI compensator (PI controller with a Clegg integrator) for which a control design framework has been developed in [3]. Different reset laws for this compensator and other reset systems have been studied: partial reset, reset band, variable reset band, variable reset percentage, re-

set at fixed time-instants (for which asymptotic stability has been guaranteed in [5]) which can be found in [3] and quadratic resetting conditions in [28]. A very different approach is opted in [29] where the after reset-state is computed in an optimization problem.

Stability of reset control systems studies can roughly be divided into two categories: Lyapunov-based and passivity-based [30]. In the former, the H_β-condition [3] is one of the conditions with which one can proof stability for reset systems with stable linear base. In a recent work, sufficient stability conditions based on measured frequency responses are given [28], which aims to elevate the need for solving linear matrix inequalities (LMI) present in most of the previous stability conditions and thus making reset controllers more accessible to control engineers in industry.

In the field of fractional reset control several results of integer reset control have been generalized to arbitrary order. These include generalizations of the CI, PI+CI and FORE to CI^α [31], PI^α+CI^α [31] and GFrORE [32] respectively. Also Lyapunov stability, satisfied by H_β-condition, has been generalized to fractional order systems in [31]. The only application of fractional reset control found in literature is application of a proportional CI^α controller on a servomotor in [33].

In context of previous mentioned works in reset control, the existence of limit cycles remains a challenge [3]. In [6] it was shown that a feedforward controller with inverse plant DC-gain could be used to avoid limit cycles. In order to increase robustness in the presence of model uncertainties, the work of [34] proposes an iterative learning algorithm to fractional order reset systems.

Although there are works in literature using fractional order reset control, no work has been found for reset control in CRONE specifically. Despite the fact that in many papers describing functions are used to shape open-loop, no controller has been found that directly relates required phase margin and reset phase lead to fractional order. Also few results have been found on practical implementation of fractional reset controllers. Therefore this thesis will focus on combining CRONE control with reset control, for which new design rules will be developed.

3

CRONE reset control

In this chapter, firstly possible CRONE reset control strategies are explained and most promising CRONE reset control strategies are selected. This reduces the strategies to lag-lead reset, lag reset and integrator reset for both first and second generation CRONE. Then the chosen control structure is presented. General design rules are developed and specific design rules are derived from these for the selected CRONE reset controllers.

3.1. CRONE reset strategies

Several CRONE reset strategies are possible. A reset strategy in this context is defined as the unique combination of the choices for: base controller, part of transfer function to be reset, the order of the part to be reset and the selection of reset approach(es). A table summarizing possible strategies can be found in table 3.1.

Table 3.1: CRONE reset strategies. Different CRONE reset strategies are possible by making combinations of choices per category/column. In the last column multiple choices are allowed.

Base controller	**Reset part**	**Reset order n**	**Reset approaches**
1. CRONE-1 2. CRONE-2	1. integrator $\frac{\omega_I}{s}$ 2. lead-lag $\frac{1+\frac{s}{\omega_b}}{1+\frac{s}{\omega_h}}$ 3. lag-lead $\frac{1+\frac{s}{\omega_h}}{1+\frac{s}{\omega_b}}$ 4. lag (ω_b) $\frac{1}{1+\frac{s}{\omega_b}}$ 5. lag (ω_h) $\frac{1}{1+\frac{s}{\omega_h}}$ 6. low-pass filter $\frac{1}{1+\frac{s}{\omega_F}}$	1. first order 2. second order 3. higher order	• partial reset • reset percentage • variable reset • reset band

Below the possible choices are explained in more detail. At the end of this section a reduced table (table 3.2) is given that contains selected choices that will be explored further in the thesis.

3.1.1. Selection base controller

For the base controller either first generation CRONE or second generation CRONE can be chosen. Depending on whether the required system bandwidth is within an asymptotic phase behaviour region, CRONE-1 can or cannot be used. First generation CRONE is used for plants with asymptotic phase behaviour in the bandwidth region. CRONE-2 is applicable in either case. Both controllers provide robustness against gain deviations.

3.1.2. Selection reset part of transfer function

A typical reset control structure can be found in figure 3.1. The reset control system Σ_R consists of a reset element Σ_r and a linear system part Σ_{nr}. In this section taking the transfer function of CRONE and choosing different parts of this transfer function to be reset (Σ_r) and to remain linear (Σ_{nr}) are investigated. A CRONE-1 controller in (2.1) consists of an integrator, lead-lag filter and low-pass filter. A CRONE-2 controller as given in (2.12) and (2.13), consists of an integrator, lag-lead filter and low-pass filter.

The choice of which part of transfer function to reset has great impact on the frequency response phase behaviour. For integrator reset the describing function predicts equal phase addition of 52° across all frequencies. In the case of lead-lag-, lag-lead- and lag reset it is expected to achieve phase lead around bandwidth. Low-pass filter with reset adds phase at frequencies after its corner frequency. As the target for CRONE reset is to have additional phase a bandwidth frequency, all the aforementioned transfer functions, excluding low-pass filter, are considered as they are much more interesting for resetting.

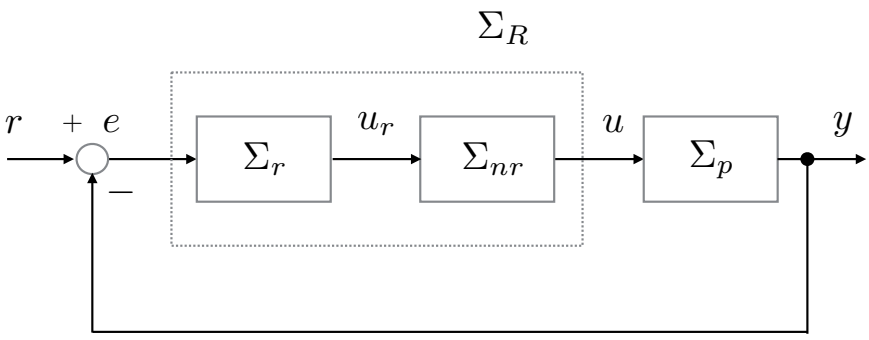

Figure 3.1: Control diagram of feedback control with a reset controller Σ_R, which contains a linear system Σ_{nr} and a non-linear reset system Σ_r.

CRONE-1 transfer function $C_F(s)$ is given by:

$$C_F(s) = C_0(1+\frac{\omega_I}{s})^{n_I}\Big(\frac{1+\frac{s}{\omega_b}}{1+\frac{s}{\omega_h}}\Big)^{\nu}\frac{1}{(1+\frac{s}{\omega_F})^{n_F}}. \tag{3.1}$$

Again assume a general n-th order reset of the reset part. Then the reset and non-reset part of the CRONE-1 transfer functions are:

CRONE-1 n-th order integrator reset

$$C_{F,\text{int}}(s) = \underbrace{(\frac{\omega_I}{s})^{n_I-n}(\frac{s}{\omega_I}+1)^{n_I}C_0\Big(\frac{1+\frac{s}{\omega_b}}{1+\frac{s}{\omega_h}}\Big)^{\nu}\frac{1}{(1+\frac{s}{\omega_F})^{n_F}}}_{\Sigma_{nr}}\underbrace{(\frac{\omega_I}{s})^{n}}_{\Sigma_r} \tag{3.2}$$

CRONE-1 n-th order lead-lag reset

A n-th order lead-lag reset has the following reset-/ non-reset part:

$$C_{F,\text{leadlag}}(s) = \underbrace{C_0(1+\frac{\omega_I}{s})^{n_I}\frac{1}{(1+\frac{s}{\omega_F})^{n_F}}\Big(\frac{1+\frac{s}{\omega_b}}{1+\frac{s}{\omega_h}}\Big)^{\nu-n})}_{\Sigma_{nr}}\underbrace{\Big(\frac{1+\frac{s}{\omega_b}}{1+\frac{s}{\omega_h}}\Big)^{n}}_{\Sigma_r} \tag{3.3}$$

CRONE-1 n-th order lag (ω_h) reset

$$\beta_{0,\text{lag}}(s) = \underbrace{C_0(1+\frac{\omega_I}{s})^{n_I}(1+\frac{s}{\omega_h})^{\nu}\frac{1}{(1+\frac{s}{\omega_F})^{n_F}}\frac{1}{(1+\frac{s}{\omega_h})^{\nu-n}}}_{\Sigma_{nr}}\underbrace{\frac{1}{(1+\frac{s}{\omega_h})^{n}}}_{\Sigma_r} \tag{3.4}$$

CRONE-1 n-th order low-pass filter reset

$$C_{F,\text{lpf}}(s) = \underbrace{C_0(1+\frac{\omega_I}{s})^{n_I}\Big(\frac{1+\frac{s}{\omega_b}}{1+\frac{s}{\omega_h}}\Big)^{\nu}\frac{1}{(1+\frac{s}{\omega_F})^{n_F-n}}}_{\Sigma_{nr}}\underbrace{\frac{1}{(1+\frac{s}{\omega_F})^{n}}}_{\Sigma_r} \tag{3.5}$$

The CRONE-2 desired open loop transfer $\beta_0(s)$ is:

$$\beta_0(s) = C_0(1+\frac{\omega_I}{s})^{n_I}\Big(\frac{1+\frac{s}{\omega_b}}{1+\frac{s}{\omega_h}}\Big)^{-\nu}\frac{1}{(1+\frac{s}{\omega_F})^{n_F}}. \tag{3.6}$$

Let us assume a general n-th order reset of the reset part. Then the reset and non-reset part of the CRONE-2 transfer functions are as below:

CRONE-2 n-th order integrator reset

A n-th order integrator reset has the following reset part and non-reset part:

$$\beta_{0,\text{int}}(s) = \underbrace{(\frac{\omega_I}{s})^{n_I-n}(\frac{s}{\omega_I}+1)^{n_I}C_0\Big(\frac{1+\frac{s}{\omega_b}}{1+\frac{s}{\omega_h}}\Big)^{-\nu}\frac{1}{(1+\frac{s}{\omega_F})^{n_F}}}_{\Sigma_{nr}}\underbrace{(\frac{\omega_I}{s})^{n}}_{\Sigma_r}. \tag{3.7}$$

CRONE-2 n-th order lag-lead reset

A n-th order lag-lead reset has the following reset-/ non-reset part:

$$\beta_{0,\text{laglead}}(s) = \underbrace{C_0(1+\frac{\omega_I}{s})^{n_I}\frac{1}{(1+\frac{s}{\omega_F})^{n_F}}\left(\frac{1+\frac{s}{\omega_b}}{1+\frac{s}{\omega_h}}\right)^{-(\nu-n)})}_{\Sigma_{nr}}\underbrace{\left(\frac{1+\frac{s}{\omega_h}}{1+\frac{s}{\omega_b}}\right)^{n}}_{\Sigma_r}. \tag{3.8}$$

CRONE-2 n-th order lag (ω_b) reset

$$\beta_{0,\text{lag}}(s) = \underbrace{C_0(1+\frac{\omega_I}{s})^{n_I}(1+\frac{s}{\omega_h})^{\nu}\frac{1}{(1+\frac{s}{\omega_F})^{n_F}}\frac{1}{(1+\frac{s}{\omega_b})^{\nu-n}}}_{\Sigma_{nr}}\underbrace{\frac{1}{(1+\frac{s}{\omega_b})^{n}}}_{\Sigma_r} \tag{3.9}$$

CRONE-2 n-th order low-pass filter reset

$$\beta_{0,\text{lpf}}(s) = \underbrace{C_0(1+\frac{\omega_I}{s})^{n_I}\left(\frac{1+\frac{s}{\omega_b}}{1+\frac{s}{\omega_h}}\right)^{-\nu}\frac{1}{(1+\frac{s}{\omega_F})^{n_F-n}}}_{\Sigma_{nr}}\underbrace{\frac{1}{(1+\frac{s}{\omega_F})^{n}}}_{\Sigma_r} \tag{3.10}$$

3.1.3. Selection reset order n

In the introduction it was mentioned that the Clegg integrator gives a phase addition of 52 degrees with respect to a linear integrator according to its describing function. An intuitive reasoning then is that with reset of a second order integrator or even higher order even higher phase addition can be achieved. However, this introduces additional non-linearity and thus higher harmonic effects will become more evident. As stability issues might arise as a result, for simplicity only first-order reset filters will be considered in this thesis.

3.1.4. Selection reset approach

In chapter 2, several existing reset approaches in literature were introduced. These are the reset parameters that can be tuned. Multiple of these approaches can be chosen at the same time. The approaches that were found are: partial reset, reset percentage (PI+CI structure), variable reset and reset band.

Only reset approaches are used for CRONE reset design that can tune the non-linearity in the system directly. This leaves the partial reset parameter γ in the reset matrix and reset percentage p such as in the PI+CI approach. This choice is made such that this tuning can bring freedom in limiting higher harmonics in the system.

Table 3.2: Reduced table CRONE reset strategies of combinations investigated in the thesis. Different CRONE reset strategies are possible by making combinations of choices per category/column. In the last column multiple choices are allowed.

Base controller	Reset part	Reset order	Reset approaches
1 CRONE-1 2 CRONE-2	1 integrator 2 lead-lag 3 lag-lead 4 lag (ω_b) 5 lag (ω_h)	first order	• partial reset • reset percentage

3.2. Control structure

The chosen reset approaches, partial reset and reset percentage, result in a CRONE reset controller with two degrees of freedom in tuning non-linearity. Firstly, the general structure of a CRONE reset controller is given. Then follows an adaptation of this structure is to include the non-linearity tuning parameters.

3.2.1. General structure

The CRONE reset control system Σ_R consists of two parts: a part that is reset Σ_r and a part that is not reset Σ_{nr}. The state-space representations are as follows:

$$\Sigma_r := \begin{cases} \dot{x}_r(t) = A_r x_r(t) + B_r e(t) & \text{if } e(t) \neq 0, \\ x_r(t^+) = A_\rho x_r(t) & \text{if } e(t) = 0, \\ u_r(t) = C_r x_r(t) + D_r e(t) \end{cases} \tag{3.11}$$

$$\Sigma_{nr} := \begin{cases} \dot{x}_{nr}(t) = A_{nr} x_{nr}(t) + B_{nr} u_r(t) \\ u_{nr}(t) = C_{nr} x_{nr}(t) + D_{nr} u_r(t) \end{cases} \tag{3.12}$$

$$\Sigma_R := \begin{cases} \dot{x}_R(t) = A_R x_R(t) + B_R e(t) & \text{if } e(t) \neq 0, \\ x_R(t^+) = \bar{A}_\rho x_R(t) & \text{if } e(t) = 0, \\ u(t) = C_R x_R(t) + D_R e(t) \end{cases} \tag{3.13}$$

where $e(t)$ is the error signal, $u_r(t)$ is the input signal to the non-reset controller, $x_r(t)$, $x_{nr}(t)$ and $x_R(t) = \begin{bmatrix} x_r^T & x_{nr}^T \end{bmatrix}^T$ are the reset-controller states, non-reset controller states and CRONE reset controller states respectively and A_ρ, $\bar{A}_\rho$ are the reset matrices. Matrices A_R, B_R, C_R, D_R are the base linear state-space matrices of

the reset system, defined as:

$$A_R = \begin{bmatrix} A_r & O \\ B_{nr}C_r & A_{nr} \end{bmatrix}, \tag{3.14}$$

$$B_R = \begin{bmatrix} B_r \\ B_{nr}D_r \end{bmatrix}, \tag{3.15}$$

$$C_R = \begin{bmatrix} D_{nr}C_r & C_{nr} \end{bmatrix}, \tag{3.16}$$

$$D_R = D_{nr}D_r \tag{3.17}$$

and reset matrix $\bar{A}_\rho$ is defined as:

$$\bar{A}_\rho = \text{diag}(A_\rho, I_{n_{nr}}) \tag{3.18}$$

where n_{nr} is the number of non-reset controller states.

The structure of this controller Σ_R is shown in figure 3.1.

3.2.2. Two-degree-of-freedom non-linearity tunable structure

Slight alterations are made to the system definitions from in (3.11) to (3.13) to obtain two degrees of freedom in tuning non-linearity within the system. The first chosen reset approach of partial reset establishes the first degree of freedom; reset matrix A_ρ is taken as:

$$A_\rho = \gamma I_{n_r} \tag{3.19}$$

where n_r is the number of reset states. With this reset matrix the after-reset state $x_R(t^+)$ is a fraction γ of the before-reset state $x_R(t)$ when error hits zero. When $\gamma = 0$ a full reset occurs, whereas the system simplifies to a full linear system when $\gamma = 1$.

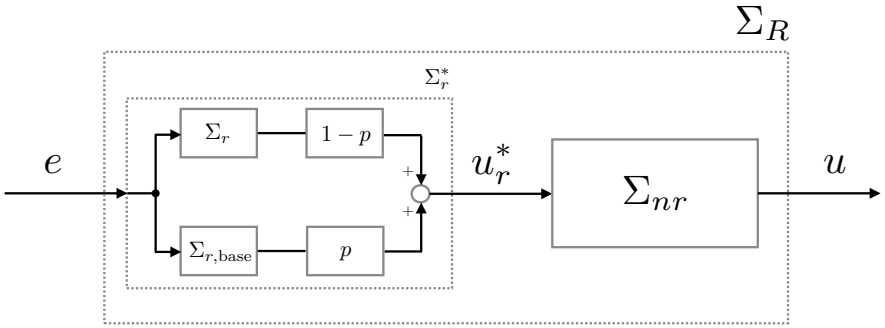

Figure 3.2: Diagram of the CRONE reset controller Σ_R with two-degree-of-freedom non-linearity tuning, which contains a linear system Σ_{nr} and a non-linear reset system Σ_r with $A_\rho = \gamma I$. $\Sigma_{r,\text{base}}$ is the base linear system of Σ_r.

The second chosen reset approach of reset percentage forms the second degree of freedom in tuning non-linearity in the system. A convex combination between the reset part Σ_r and its linear base system $\Sigma_{r,\text{base}}$ is taken as shown in figure 3.2 in Σ_r^*. p is the percentage of linearity in the system. When $p = 0$, Σ_r^* is equivalent to Σ_r and when $p = 1$ the system becomes fully linear.

3.3. New design rules

In this section new design rules are developed for first and second generation CRONE. Firstly, a general design is given in which new fractional order calculation is formulated. This is followed by specific design for CRONE-1 reset control and for CRONE-2 reset control.

3.3.1. General design

Using the describing function of the reset part of the initial CRONE controller, the obtained phase lead with respect to the controller without reset is quantified. This phase lead is used for the calculation of a new fractional order of the lead-lag/lag-lead filter that gives the same phase margin. The new fractional order can be computed as:

$$\nu^* = \frac{-\pi + M_\Phi - \angle G(j\omega_{cg}) + n_F \arctan\frac{\omega_{cg}}{\omega_F} + n_I(\frac{\pi}{2} - \arctan\frac{\omega_{cg}}{\omega_I}) - \Phi_r(\omega_{cg})}{\arctan\frac{\omega_{cg}}{\omega_h} - \arctan\frac{\omega_{cg}}{\omega_b}} \tag{3.20}$$

with $\nu^* \in [0, 1]$ for first generation CRONE and

$$\nu^* = \frac{-\pi + M_\Phi + n_F \arctan\frac{\omega_{cg}}{\omega_F} + n_I(\frac{\pi}{2} - \arctan\frac{\omega_{cg}}{\omega_I}) - \Phi_r(\omega_{cg})}{\arctan\frac{\omega_{cg}}{\omega_h} - \arctan\frac{\omega_{cg}}{\omega_b}} \tag{3.21}$$

with $\nu^* \in [1, 2]$ for second generation CRONE, in which $\Phi_r(\omega_{cg})$ is the reset phase lead at bandwidth frequency. Below it will firstly be explained how this formula is found. Then the calculation of phase lead achieved by reset control as a function of frequency is derived for the different CRONE reset strategies.

As validation of the found equations open-loop for CRONE-2 reset controllers are plot in figure 3.3. As expected, similar phase margin is found for different values of p and open loop shape has improved.

Formulation of adjusted fractional order

A general frequency response $H(j\omega)$ can be written in terms of its system poles and zeros:

$$H(j\omega) = K\frac{\prod_{i=1}^{m}(j\omega - z_i)}{\prod_{j=1}^{n}(j\omega - p_j)} \tag{3.22}$$

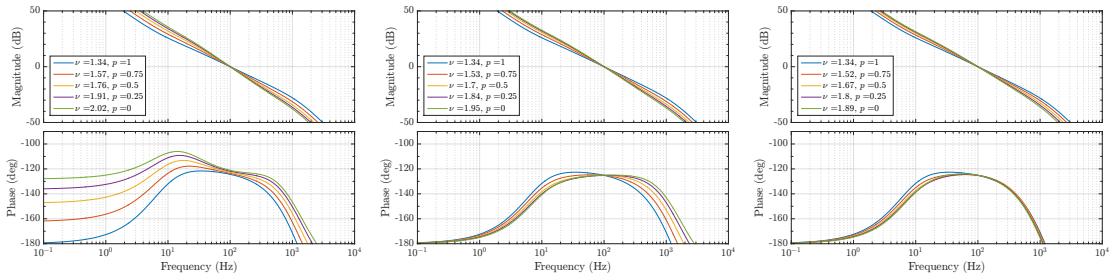

Figure 3.3: Open-loop for second generation CRONE reset controller for $\gamma = 0$ and different p-values with (a) integrator reset, (b) lag reset and (c) lag-lead reset. For the same phase margin the open loop gain behaviour with reset is favourable.

in which K is a constant, z_i are the system zeros and p_j are the system poles. m and n are the number of zeros and poles respectively. The phase angle can be calculated from:

$$\angle H(j\omega) = \sum_{i=1}^{m} \angle(j\omega - z_i) - \sum_{j=1}^{n} \angle(j\omega - p_i) \tag{3.23}$$

in which the phase angle of an arbitrary point in phase plane $g = \sigma_g + j\omega_g$ is given by:

$$\angle(j\omega - g) = \arctan\left(\frac{\omega - \omega_g}{-\sigma_g}\right) \tag{3.24}$$

Using (3.23) and (3.24) the phase of the CRONE-1 controller $C_F(j\omega)$ is:

$$\angle C_F(j\omega) = n_i(\arctan\frac{\omega}{\omega_I} - \frac{\pi}{2}) + \nu(\arctan\frac{\omega}{\omega_b} - \arctan\frac{\omega}{\omega_h}) - n_F \arctan\frac{\omega}{\omega_F}. \tag{3.25}$$

As additional reset creates phase lead $\Phi_r(\omega)$, the new CRONE-1 reset controller phase will be:

$$\angle C_F^*(j\omega) = n_i(\arctan\frac{\omega}{\omega_I} - \frac{\pi}{2}) + \nu(\arctan\frac{\omega}{\omega_b} - \arctan\frac{\omega}{\omega_h}) - n_F \arctan\frac{\omega}{\omega_F} + \Phi_r(\omega). \tag{3.26}$$

To ensure phase margin M_ϕ at bandwidth frequency ω_{cg} the open-loop phase has to be equal to $-\pi + M_\Phi$. Solving (3.26) for this value at $\omega = \omega_{cg}$ results in a new fractional order:

$$\nu^* = \frac{-\pi + M_\Phi - \angle G(j\omega_{cg}) + n_F \arctan\frac{\omega_{cg}}{\omega_F} + n_I(\frac{\pi}{2} - \arctan\frac{\omega_{cg}}{\omega_I}) - \Phi_r(\omega_{cg})}{\arctan\frac{\omega_{cg}}{\omega_h} - \arctan\frac{\omega_{cg}}{\omega_b}}. \tag{3.27}$$

For second generation CRONE reset the same approach yields:

$$\nu^* = \frac{-\pi + M_\Phi + n_F \arctan\frac{\omega_{cg}}{\omega_F} + n_I(\frac{\pi}{2} - \arctan\frac{\omega_{cg}}{\omega_I}) - \Phi_r(\omega_{cg})}{\arctan\frac{\omega_{cg}}{\omega_h} - \arctan\frac{\omega_{cg}}{\omega_b}}. \tag{3.28}$$

Phase lead for CRONE reset

The general describing function of a reset system as defined in [35] is given by:

$$G_{\text{DF}}(j\omega) = C(j\omega I - A)^{-1}B(I + j\Theta_D(\omega)) + D \tag{3.29}$$

where A, B, C, D are the base state-space matrices and $\Theta_D(\omega)$ is defined as:

$$\Theta_D(\omega) = -\frac{2\omega^2}{\pi}\Delta(\omega)[\Gamma_D(\omega) - \Lambda^{-1}(\omega)]. \tag{3.30}$$

The definitions of the set of equations used are given below:

$$\begin{cases} \Lambda(\omega) = \omega^2 I + A^2 \\ \Delta(\omega) = I + e^{\frac{\pi}{\omega}A} \\ \Delta_D(\omega) = I + A_\rho e^{\frac{\pi}{\omega}A} \\ \Gamma_D(\omega) = \Delta_D^{-1}(\omega)A_\rho\Delta(\omega)\Lambda^{-1}(\omega) \end{cases}$$

A linear combination is made between describing function of the reset system and its linear base equivalent to include the convex-combination structure with reset percentage p:

$$G^*_{\text{DF}}(j\omega) = p\Big(C(j\omega I - A)^{-1}B + D\Big) + (1-p)\Big(C(j\omega I - A)^{-1}B(I + j\Theta_D(\omega)) + D\Big). \tag{3.31}$$

The additional phase at bandwidth is given by $\Phi_r(\omega_{cg})$, which is retrieved by filling in $\omega = \omega_{cg}$ in:

$$\Phi_r(\omega) = \angle G^*_{\text{DF}}(j\omega) - \angle G(j\omega). \tag{3.32}$$

CRONE lead-lag/lag-lead reset Consider a first order lead-lag/lag-lead filter:

$$H_{\text{ll}}(s) = \frac{1 + \frac{s}{a}}{1 + \frac{s}{b}} \tag{3.33}$$

where a and b are the corner frequencies. For such first order filters $\Theta_D(\omega)$ is expressed as:

$$\Theta_D(\omega, b, \gamma) = \frac{2}{\pi}\frac{1 + e^{-\pi\frac{b}{\omega}}}{1 + (\frac{b}{\omega})^2}\frac{1-\gamma}{1+\gamma e^{-\pi\frac{b}{\omega}}} \tag{3.34}$$

Then the phase lead for $H_{\text{ll}}(s)$ in (3.33) with partial reset γ and reset percentage p can be computed as:

$$\Phi_{r,\text{ll}}(\omega,a,b,\gamma,p) = \arctan\left(\frac{(1-p)\Theta_D(\omega,b,\gamma)(1-\frac{b}{a})}{1+(\frac{\omega}{a})^2+(1-p)\frac{\omega}{a}\Theta_D(\omega,b,\gamma)(1-\frac{b}{a})}\right). \tag{3.35}$$

The derivation of both $\Theta_D(\omega)$ and this phase lead can be found in Appendix B.

CRONE lag reset When in (3.33) $a \to \infty$ $H_{ll}(s)$ simplifies to a lag filter. Therefore the phase lead of (3.35) becomes:

$$\Phi_{r,\text{lag}}(\omega,b,\gamma,p) = \arctan\Big((1-p)\Theta_D(\omega,b,\gamma)\Big). \tag{3.36}$$

CRONE integrator reset The reset phase lead for an integrator reset is:

$$\Phi_{r,\text{int}}(\gamma,p) = \arctan\left(\frac{4}{\pi}(1-p)\frac{1-\gamma}{1+\gamma}\right) \tag{3.37}$$

which is frequency-independent.

3.3.2. First generation CRONE reset

In this subsection, design for first generation CRONE reset control is given. The controller structure in terms of reset part of the controller and non-reset part of the controller is given below for integrator reset, lag-lead reset and lag-reset.

CRONE-1 integrator reset

$$C_{\text{int}}(s) = \underbrace{(\frac{\omega_I}{s})^{n_I-1}C_0(\frac{s}{\omega_I}+1)^{n_I}\left(\frac{1+\frac{s}{\omega_b}}{1+\frac{s}{\omega_h}}\right)^{\nu}\frac{1}{(1+\frac{s}{\omega_F})^{n_F}}}_{\Sigma_{nr}}\underbrace{\frac{\omega_I}{s}}_{\Sigma_r} \tag{3.38}$$

and phase lead with integrator reset is given by (3.37).

CRONE-1 lag-lead reset

$$C_{\text{laglead}}(s) = \underbrace{\left(\frac{1+\frac{s}{\omega_b}}{1+\frac{s}{\omega_h}}\right)^{\nu+1}C_0(1+\frac{\omega_I}{s})^{n_I}\frac{1}{(1+\frac{s}{\omega_F})^{n_F}}}_{\Sigma_{nr}}\underbrace{\frac{1+\frac{s}{\omega_h}}{1+\frac{s}{\omega_b}}}_{\Sigma_r} \tag{3.39}$$

and phase lead with lag-lead reset is given by (3.35) with $b=\omega_b$ and $a=\omega_h$.

CRONE-1 lag (ω_b) reset

$$C_{\text{lag}}(s) = \underbrace{\frac{(1+\frac{s}{\omega_b})^{\nu+1}}{(1+\frac{s}{\omega_h})^{\nu}} C_0 (1+\frac{\omega_I}{s})^{n_I} \frac{1}{(1+\frac{s}{\omega_F})^{n_F}}}_{\Sigma_{nr}} \underbrace{\frac{1}{1+\frac{s}{\omega_b}}}_{\Sigma_r} \tag{3.40}$$

and phase lead with lag reset is given by (3.36) with $b = \omega_b$.

The controller structure for integrator reset follows directly from (3.37). The choice for lag-lead reset and lag reset structure requires a more extensive explanation and derivation, which follows below.

Comparison lead-lag reset and lag-lead reset In section 2.1 the transfer functions of CRONE-1 and CRONE-2 were formulated. It can be seen in (2.1) that the CRONE-1 transfer function includes a lead-lag filter, whereas CRONE-2 has a lag-lead filter in (2.12). This motivates investigation of the differences between resetting lead-lag and lag-lead.

In table 3.3 frequency responses using describing function are shown together with their linear base transfer functions, comparing reset within transfer functions for lead-lag filter $\frac{1+\frac{s}{\omega_b}}{1+\frac{s}{\omega_h}}$ and within the lag-lead filter $\frac{1+\frac{s}{\omega_h}}{1+\frac{s}{\omega_b}}$ (in which $\omega_h > \omega_b$). These frequency responses are computed for scaling factor 3 such that $\omega_b = \frac{\omega_{cg}}{3}$, $\omega_h = 3\omega_{cg}$ and bandwidth of 100 Hz but for other values similar results are expected.

It becomes evident that in the frequency responses in the second column, which displays reset within lag-lead filter, significantly more phase around bandwidth is achieved compared to reset within lead-lag filter. In case of resetting complete lead-lag filter, reset even creates unwanted phase lag. Thus reset within lag-lead filter appears to be a better solution compared to reset within lead-lag filter. This is due to the fact that reset phase lead is mostly dependent on the reset pole. Consider a FORE, in which the reset pole is the corner frequency of a first order filter. Small phase lead can be achieved before the corner frequency and phase lead increases for increasing frequency. This implies that in the case of resetting a filter with reset pole ω_h, the approximated phase lead at bandwidth frequency is small.

Although CRONE-1 transfer function has a lead-lag filter, it is possible to rewrite the transfer function such that reset occurs in a lag-lead filter. The fractional CRONE-1 lead-lag filter can be rewritten as follows:

$$\left(\frac{1+\frac{s}{\omega_b}}{1+\frac{s}{\omega_h}}\right)^{\nu} = \left(\frac{1+\frac{s}{\omega_b}}{1+\frac{s}{\omega_h}}\right)^{-1} \left(\frac{1+\frac{s}{\omega_b}}{1+\frac{s}{\omega_h}}\right)^{\nu+1} = \frac{1+\frac{s}{\omega_h}}{1+\frac{s}{\omega_b}} \left(\frac{1+\frac{s}{\omega_b}}{1+\frac{s}{\omega_h}}\right)^{\nu+1}. \tag{3.41}$$

From this the controller structures for CRONE-1 lag-lead reset and CRONE-1 lag-reset directly follow.

Table 3.3: Describing function for resetting denominator and resetting complete transfer function of lead-lag filter and lag-lead filter.

Reset part	lead-lag $\left(\frac{1+\frac{s}{\omega_l}}{1+\frac{s}{\omega_h}}\right)$	lag-lead $\left(\frac{1+\frac{s}{\omega_h}}{1+\frac{s}{\omega_l}}\right)$
lag reset	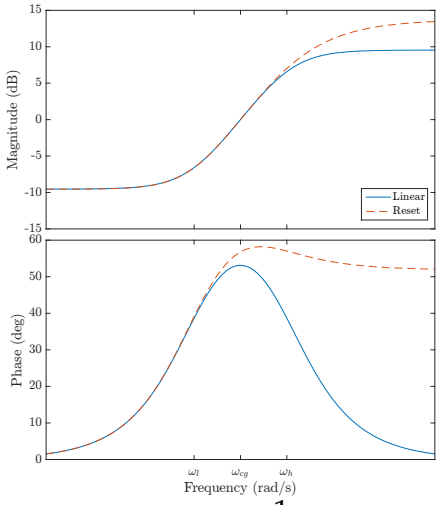 $\underbrace{(1+\frac{s}{\omega_l})}_{\Sigma_{nr}}\underbrace{\frac{1}{1+\frac{s}{\omega_h}}}_{\Sigma_r}$	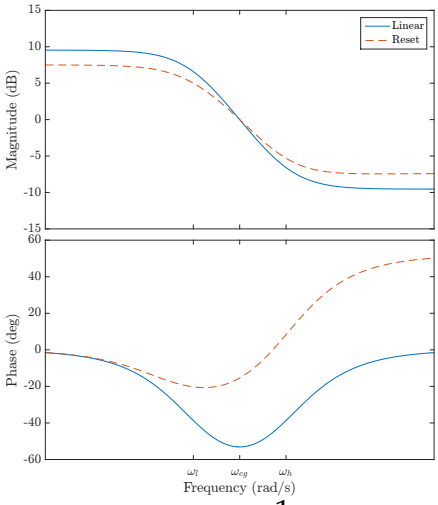 $\underbrace{(1+\frac{s}{\omega_h})}_{\Sigma_{nr}}\underbrace{\frac{1}{1+\frac{s}{\omega_l}}}_{\Sigma_r}$
full lead-lag-/lag-lead reset	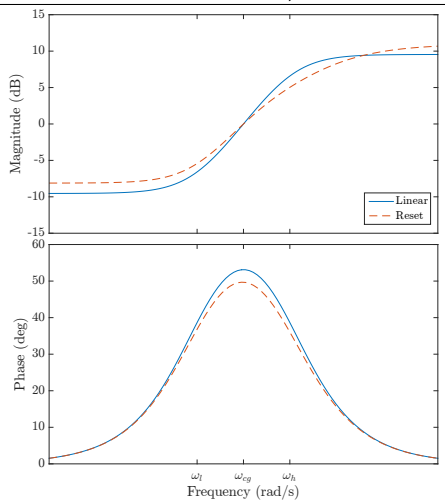 $\underbrace{\frac{1+\frac{s}{\omega_l}}{1+\frac{s}{\omega_h}}}_{\Sigma_r}$	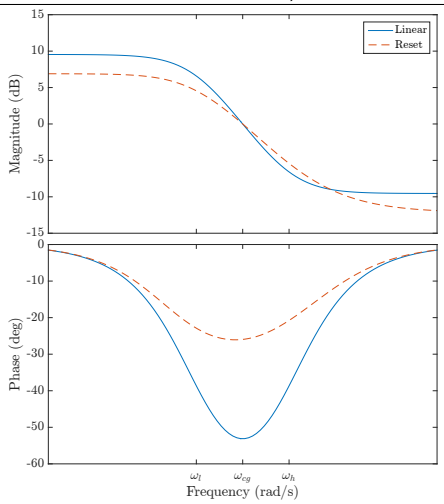 $\underbrace{\frac{1+\frac{s}{\omega_h}}{1+\frac{s}{\omega_l}}}_{\Sigma_r}$

3.3.3. Second generation CRONE reset

In this subsection design for second generation CRONE reset control is given. The desired open-loop $\beta_0(s)$ structure in terms of reset part and non-reset part is given below for integrator reset, lag-lead reset and lag-reset. CRONE-2 controller is then computed as $C_S(s) = \beta_0(s)G_0^{-1}(s)$ with nominal plant $G_0(s)$.

CRONE-2 integrator reset

$$\beta_{0,\text{int}}(s) = \underbrace{(\frac{\omega_I}{s})^{n_I-1}C_0(\frac{s}{\omega_I}+1)^{n_I}\left(\frac{1+\frac{s}{\omega_b}}{1+\frac{s}{\omega_h}}\right)^{-\nu}\frac{1}{(1+\frac{s}{\omega_F})^{n_F}}}_{\Sigma_{nr}}\underbrace{\frac{\omega_I}{s}}_{\Sigma_r} \tag{3.42}$$

and phase lead with integrator reset is given by (3.37).

CRONE-2 lag-lead reset

$$\beta_{0,\text{laglead}}(s) = \underbrace{\left(\frac{1+\frac{s}{\omega_b}}{1+\frac{s}{\omega_h}}\right)^{-(\nu-1)}C_0(1+\frac{\omega_I}{s})^{n_I}\frac{1}{(1+\frac{s}{\omega_F})^{n_F}}}_{\Sigma_{nr}}\underbrace{\frac{1+\frac{s}{\omega_h}}{1+\frac{s}{\omega_b}}}_{\Sigma_r} \tag{3.43}$$

and phase lead with lag-lead reset is given by (3.35) with $b = \omega_b$ and $a = \omega_h$.

CRONE-2 lag (ω_b) reset

$$\beta_{0,\text{lag}}(s) = \underbrace{\frac{(1+\frac{s}{\omega_b})^{-(\nu-1)}}{(1+\frac{s}{\omega_h})^{-\nu}}C_0(1+\frac{\omega_I}{s})^{n_I}\frac{1}{(1+\frac{s}{\omega_F})^{n_F}}}_{\Sigma_{nr}}\underbrace{\frac{1}{1+\frac{s}{\omega_b}}}_{\Sigma_r} \tag{3.44}$$

and phase lead with lag reset is given by (3.36) with $b = \omega_b$.

3.4. Stability analysis

3.4.1. Global asymptotic periodic solution open-loop

The stability condition of [35] is sufficient and necessary for a global asymptotically converging periodic solution. This condition computes the eigenvalues for the open loop state-space matrix A_{ol} and reset matrix A_ρ as follows:

$$|\lambda(A_\rho e^{\frac{\pi}{\omega}A_{ol}})| < 1 \tag{3.45}$$

where the open loop state-space matrix A_{ol} is given by a series interconnection between the plant and the controller:

$$A_{ol} = \begin{bmatrix} A_R & O \\ A_p & B_pC_R \end{bmatrix} \tag{3.46}$$

where A_p, B_p being plant state-space matrices and A_R, C_R being the reset control state-space matrices as defined in (3.14) and (3.16). Reset matrix A_ρ is defined as in (3.18).

3.4.2. Quadratic stability closed-loop system

Consider reset system Σ_R as in figure 3.2 in closed loop with a plant Σ_p. Then asymptotic stability is guaranteed when following conditions are true:

Theorem 2. *[3]. Let $V : \mathbb{R}^n \to \mathbb{R}^n$ be a continuously differentiable, positive-definite, radially unbounded function such that*

$$\dot{V}(x) := \left(\frac{\partial V}{\partial x}\right)^T A_{cl} x < 0, \quad \text{if } e(t) \neq 0, \tag{3.47}$$

$$\Delta V(x) := V(A_\rho^* x) - V(x) \leq 0, \quad \text{if } e(t) = 0 \tag{3.48}$$

where A_ρ^* is the reset matrix and A_{cl} is the closed-loop A-matrix:

$$A_{cl} = \begin{bmatrix} \bar{A} & \bar{B}C_{nrp} \\ -B_{nrp}\bar{C} & A_{nrp} \end{bmatrix} \tag{3.49}$$

where $(\bar{A}, \bar{B}, \bar{C}, \bar{D})$ are the state-space matrices of Σ_r^* and $(A_{nrp}, B_{nrp}, C_{nrp}, D_{nrp})$ are the state-space matrices of non-reset controller Σ_{nr} and plant Σ_p combined in series. $\bar{A}$ is defined as:

$$\bar{A} = \begin{bmatrix} A_r & 0 \\ 0 & A_r \end{bmatrix} \tag{3.50}$$

$\bar{B}$ is defined as:

$$\bar{B} = \begin{bmatrix} B_r \\ B_r \end{bmatrix} \tag{3.51}$$

and A_ρ^* is defined as:

$$A_\rho^* = \text{diag}(A_\rho, I_{n_r}, I_{n_{nrp}}) \tag{3.52}$$

where n_r is the number of reset states and n_{nrp} is sum of the number of states of non-reset controller n_{nr} and plant n_p.

Then the reset control system is asymptotically stable.

Quadratic stability is guaranteed when (3.47) and (3.48) hold true for a potential function $V(x) = x^T P x$ with $P > 0$. From this condition the authors of [3] obtained following theorem for proving quadratic stability:

Theorem 3. *[3]. There exists a constant $\beta \in \mathbb{R}^{n_r \times 1}$ and $P_\rho \in \mathbb{R}^{n_r \times n_r}, P_\rho > 0$ where n_r is the number of reset states, such that the restricted Lyapunov equation*

$$P > 0, \quad A_{cl}^T P + P A_{cl} < 0, \tag{3.53}$$

$$B_0^T P = C_0 \tag{3.54}$$

has a solution for P, where C_0 and B_0 are defined by:

$$C_0 = \begin{bmatrix} \beta C_{nrp} & O_{n_r \times n_{\text{rnr}}} & P_\rho \end{bmatrix}, B_0 = \begin{bmatrix} O_{n_{nrp} \times n_r} \\ O_{n_r \times n_r} \\ I_{n_r} \end{bmatrix}. \tag{3.55}$$

4

System overview

In this chapter the experimental setup is described. Firstly, an overview is given of both hardware and software. Secondly, a system identification is performed to identify the system parameters and transfer functions.

4.1. Experimental setup

4.1.1. General overview

The practical setup used for experimental validation is a one degree of freedom dual precision stage designed by Bart Joziasse, a former graduate student at the PME department. This setup consists of a coarse stage and a fine stage which can be actuated separately. A picture of the system can be found in figure 4.1a.

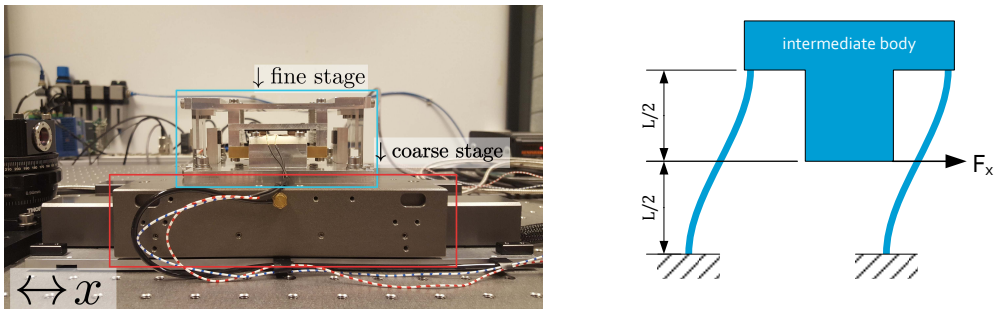

Figure 4.1: (a) Experimental setup: one degree of freedom precision dual stage. (b) Fine stage is attached to the coarse stage using flexure guiding. Image courtesy of [36].

The coarse stage is a *Aerotech ABL10100LT* linear stage. This air bearing-guided stage is driven by a linear motor. The fine stage is a custom-designed flexure-guided stage actuated by a Lorentz actuator. The configuration can be seen in figure 4.1b. The flexible strips connect both stages to one another and are actuated at the middle of the length of the strips. A dSPACE DS1103 real-time control system reads out position measurements from both stages and provides the required voltage signals to the system. These signals are computed by controllers designed in a MATLAB/Simulink environment and run on dSPACE in real-time.

A schematic diagram is shown in figure 4.2. The coarse stage is driven by an *Aerotech Soloist ML* drive which internally converts a voltage input to a current

signal. Similarly, the voltage signal for the fine stage is converted to a current signal that is fed to the Lorentz actuator.

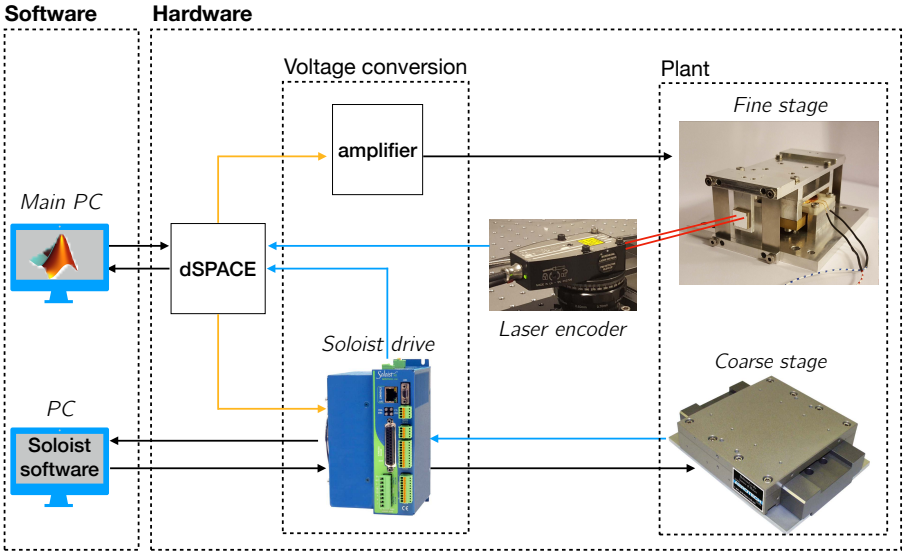

Figure 4.2: Schematic overview of the experimental setup. Orange lines show control input voltage supply to the current feedback amplifier and the Soloist drive. Blue arrows show the flow of position measurement signals.

4.1.2. Fine stage

All the fine stage components are introduced below and shown in table 4.1.

Table 4.1: Fine stage components per category

Category	Fine stage
Sensor	Renishaw RLE10 laser interferometer
Actuator	Lorentz actuator
Voltage conversion	Current feedback amplifier

Sensor

The Renishaw RLE10 laser interferometer has a Class 2 HeNe laser source with 633 nm wavelength. The output is a digital quadrature encoded signal from which a position measurement can be inferred. The resolution of this laser encoder is 10 nm.

Actuator

The Lorentz actuator is made of copper wire with a diameter of 0.5 mm wounded 140 times. The motor constant of the actuator is 1.61 N/A within $\pm$ 2 mm range [37].

Voltage conversion

A current feedback amplifier converts the analogue voltage output of the dSPACE control system to a current input for the Lorentz actuator.

4.1.3. Coarse stage

An overview of coarse stage components is given in table 4.2 and introduced in the next paragraphs.

Sensor

The Aerotech linear stage has an internal linear encoder that achieves 10 nm resolution. This sensor also provides a quadrature encoded signal that is converted to a position measurement.

Actuator and voltage conversion

The Aerotech stage has a stroke of 100 mm containing a linear motor with a motor constant of 3.29 N/A [38]. The stage is driven by a Soloist ML Drive in torque mode control. In this mode the control input voltage provided by dSPACE is converted to a current signal given to the motor that achieves corresponding torque.

Table 4.2: Coarse stage components per category

Category	Coarse stage
Sensor	Aerotech ABL10100LT internal linear encoder
Actuator	Aerotech ABL10100LT embedded linear motor
Voltage conversion	Aerotech Soloist ML drive

4.1.4. Controller implementation

Hardware

The encoder signals of both sensors are read out by a 24-bit encoder interface and provided to a dSPACE DS1103 real-time control system. This dSPACE system takes both digital and analogue inputs and can be programmed to send both digital and analogue outputs using 16 bit D/A- and A/D-converters.

Software

Simulink models can be exported to C-code and ran online on the dSPACE control system. Workspace variables as defined in MATLAB/Simulink can be changed real-time on the running program using dSPACE ControlDesk software. Furthermore, measurements can be visualized in the software and data can be recorded.

4.2. System identification

4.2.1. Dynamical system model

Single stage

When the stages are disconnected from one another, the individual stages are modelled as single mass systems. The transfer function of a single mass model is:

$$\frac{X(s)}{F(s)} = \frac{1}{ms^2 + cs + k} \tag{4.1}$$

where m is the mass, c the damping coefficient and k is the stiffness in the system. The transfer from control input voltage to force is modelled with a constant K:

$$\frac{X(s)}{V(s)} = \frac{K}{ms^2 + cs + k}. \tag{4.2}$$

Dual stage

The dual stage system is modelled as a double mass-spring-damper system, which is a fourth-order system. See figure 4.3. Performing the Laplace Transform on the equations of motion yields:

$$\begin{cases} \Big(m_{cs}s^2 + (c_{cs} + c_{fs})s + (k_{cs} + k_{fs})\Big)X_{cs}(s) - \Big(c_{fs}s + k_{fs}\Big)X_{fs}(s) & = F_{cs}(s) - F_{fs}(s) \\ \Big(m_{fs}s^2 + c_{fs}s + k_{fs}\Big)X_{fs}(s) - \Big(c_{fs}s + k_{fs}\Big)X_{cs}(s) & = F_{fs}(s) \end{cases} \tag{4.3}$$

Then the 2×2-MIMO system $G(s)$, which describes the transfer from inputs F_{cs} and F_{fs} to the outputs X_{cs} and X_{fs}, is given by:

$$\begin{bmatrix} X_{cs}(s) \\ X_{fs}(s) \end{bmatrix} = \begin{bmatrix} G_{11}(s) & G_{12}(s) \\ G_{21}(s) & G_{22}(s) \end{bmatrix} \begin{bmatrix} F_{cs}(s) \\ F_{fs}(s) \end{bmatrix} \tag{4.4}$$

in which the individual matrices $G_{ij}(s)$ are:

$$\begin{cases} G_{11}(s) = \frac{m_{fs}s^2+c_{fs}s+k_{fs}}{(m_{fs}s^2+c_{fs}s+k_{fs})(m_{cs}s^2+(c_{fs}+c_{cs})s+k_{fs}+k_{cs})-(c_{fs}s+k_{fs})^2} \\ G_{12}(s) = \frac{-m_{fs}s^2}{(m_{fs}s^2+c_{fs}s+k_{fs})(m_{cs}s^2+(c_{fs}+c_{cs})s+k_{fs}+k_{cs})-(c_{fs}s+k_{fs})^2} \\ G_{21}(s) = \frac{c_{fs}s+k_{fs}}{(m_{fs}s^2+c_{fs}s+k_{fs})(m_{cs}s^2+(c_{fs}+c_{cs})s+k_{fs}+k_{cs})-(c_{fs}s+k_{fs})^2} \\ G_{22}(s) = \frac{m_{cs}s^2+c_{cs}s+k_{cs}}{(m_{fs}s^2+c_{fs}s+k_{fs})(m_{cs}s^2+(c_{fs}+c_{cs})s+k_{fs}+k_{cs})-(c_{fs}s+k_{fs})^2} \end{cases} \tag{4.5}$$

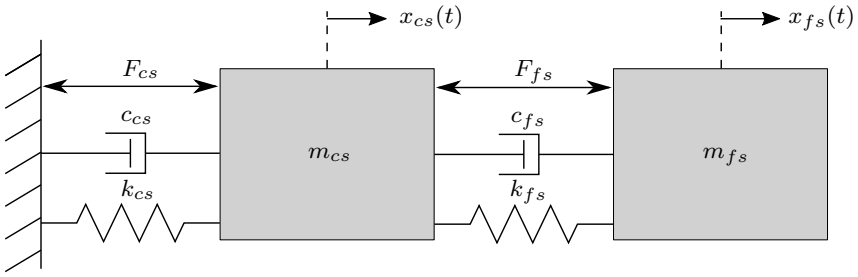

Figure 4.3: Dual precision stage modelled as a double mass model with spring and damping elements. Image courtesy of [37].

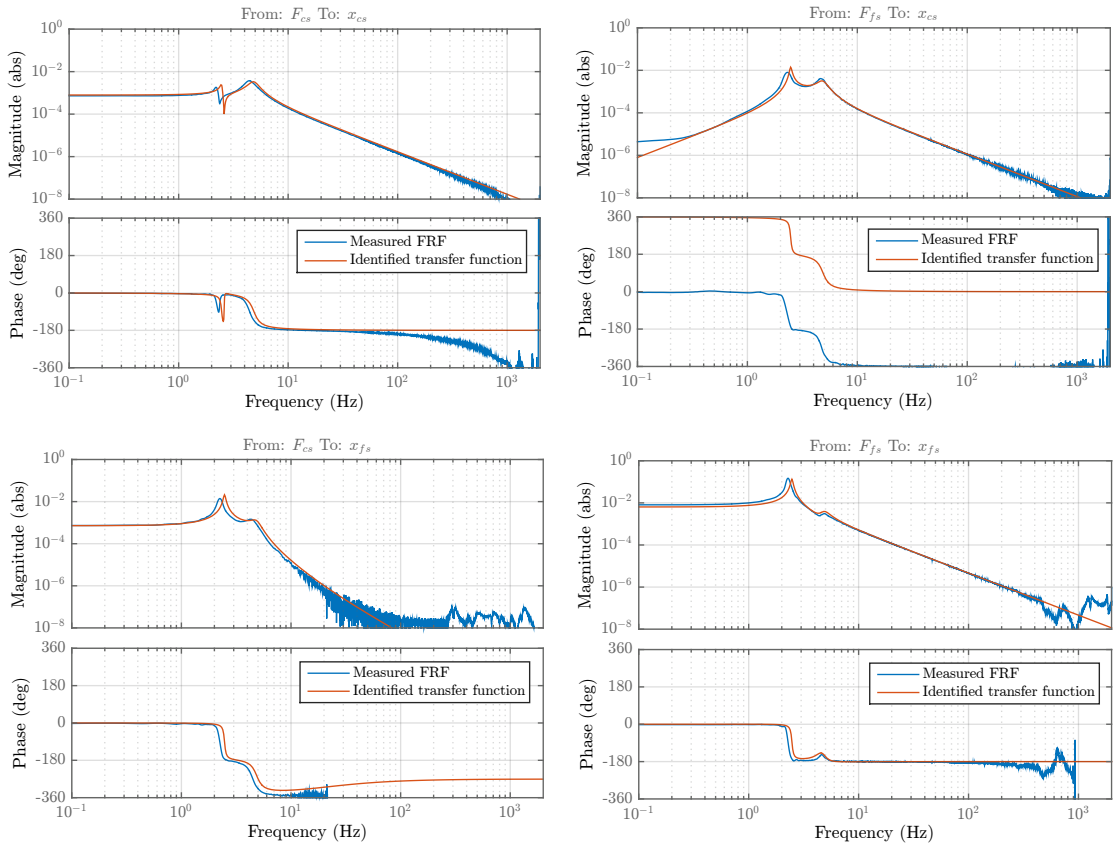

Figure 4.4: Measured frequency response function and identified transfer functions of the system.

4.2.2. Frequency response

In figure 4.4 the frequency response and the identified system can be found.

The resonance frequencies in the system are at 2.5 Hz and 4.5 Hz. To retrieve this frequency response, the system has been excited with a known control input

sequence and the system outputs signals have been measured. Using white noise and frequency sweeps a frequency response function is found using the `etfe` function in MATLAB. This function uses the Fast Fourier Transform algorithm to find an empirical transfer function.

4.2.3. Time domain identification

The identification of system parameters has been done by minimizing error between simulated output and measured output signals using an optimization problem. The algorithm used is the `lsqnonlin` algorithm from the Optimization Toolbox in MATLAB for which the objective function is the error. As optimization problems require initial values that are close to the ideal parameters, the problem has been solved in three steps: identification of the coarse stage parameters only, identification of the fine stage only and identification of all the system parameters.

All the identified systems have been validated using the recorded data from another dataset. For both datasets the variance account for (VAF) is calculated.

For the identification of the coarse stage, the identified parameters are optimized for a white noise signal. A VAF of 100.0 % has been calculated for the optimized parameters. These parameters have been validated on another dataset recorded for a white noise sequence. The VAF of this set is 100.0 % as well. See figure 4.5.

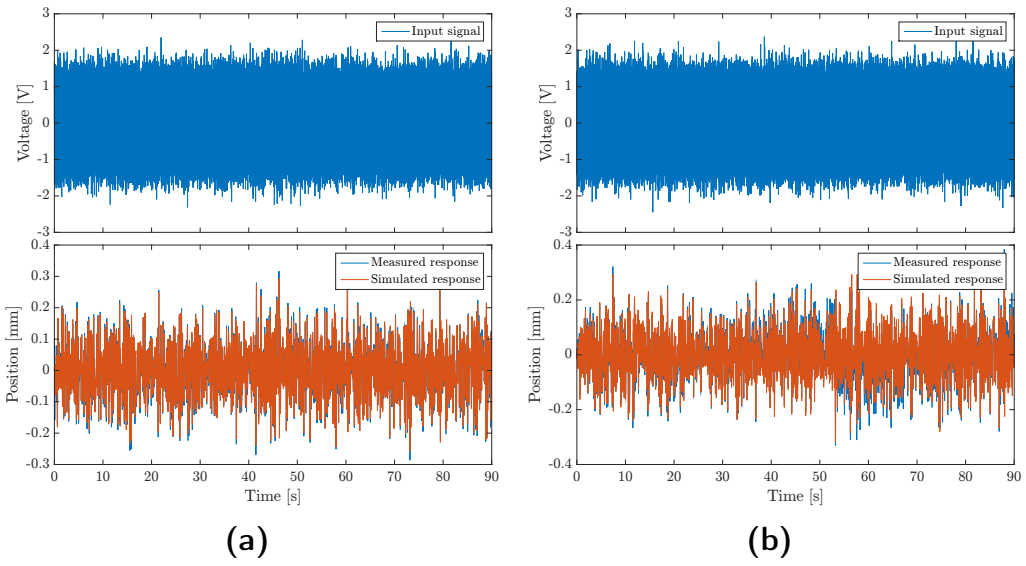

Figure 4.5: Simulated response versus measured position of coarse stage for (a) the identification set white noise signal and (b) validation set white noise signal. The calculated VAFs are 100.0 % in both cases.

For identification of fine stage parameters the identification set is the data measured for a filtered chirp signal. A VAF of 99.9 % has been found. For the validation set (white noise signal), the calculated VAF is 99.0 %. The measured and simulated

response can be found in figure 4.6.

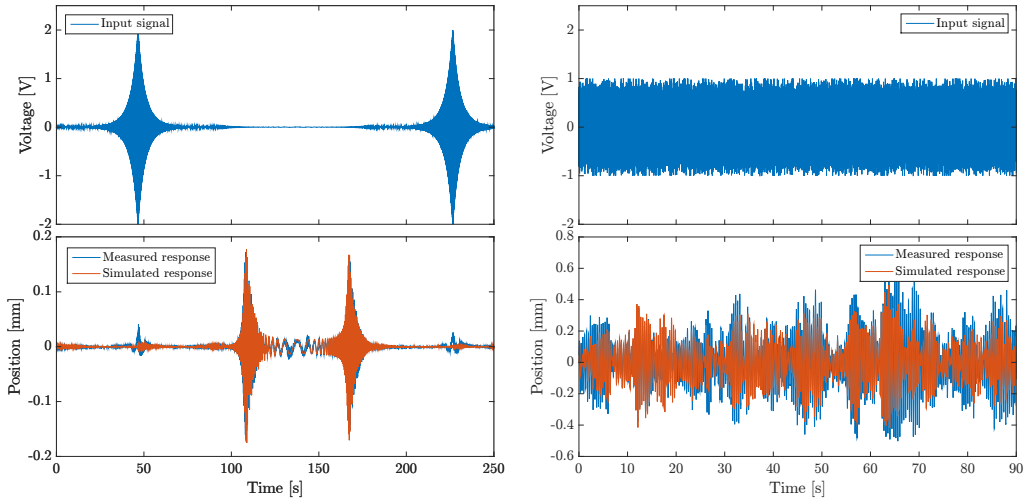

Figure 4.6: Simulated response versus measured position of fine stage for (a) the identification set chirp signal and (b) validation set white noise signal. The calculated VAF is 99.9 % and 99.0 % respectively.

4.2.4. Frequency domain identification

The identified parameters in the experiments aforementioned were put in another optimization cycle, but did not converge. Instead, a grey-box identification was performed and validated on several datasets. Using MATLAB function `tfest`, the transfer function of $G_{22}(s)$ was fitted. The denominator, containing information of the resonance peaks, was used for the other three transfer functions. The zeros of the unidentified transfer functions were chosen using the identified parameters enlisted in table 4.3 and the transfer function gains were manually adjusted. As systems have a unique frequency response, the identified system was expected to be close to the real system. This expectation was validated by simulating the response to a control signal and comparing this response to the measured one. For the dataset captured for a filtered chirp response, a VAF of 97.6 % was calculated. This can be seen in figure 4.7a. For a white noise input signal, the simulated response gave a VAF of 97.2 %. See figure 4.7b.

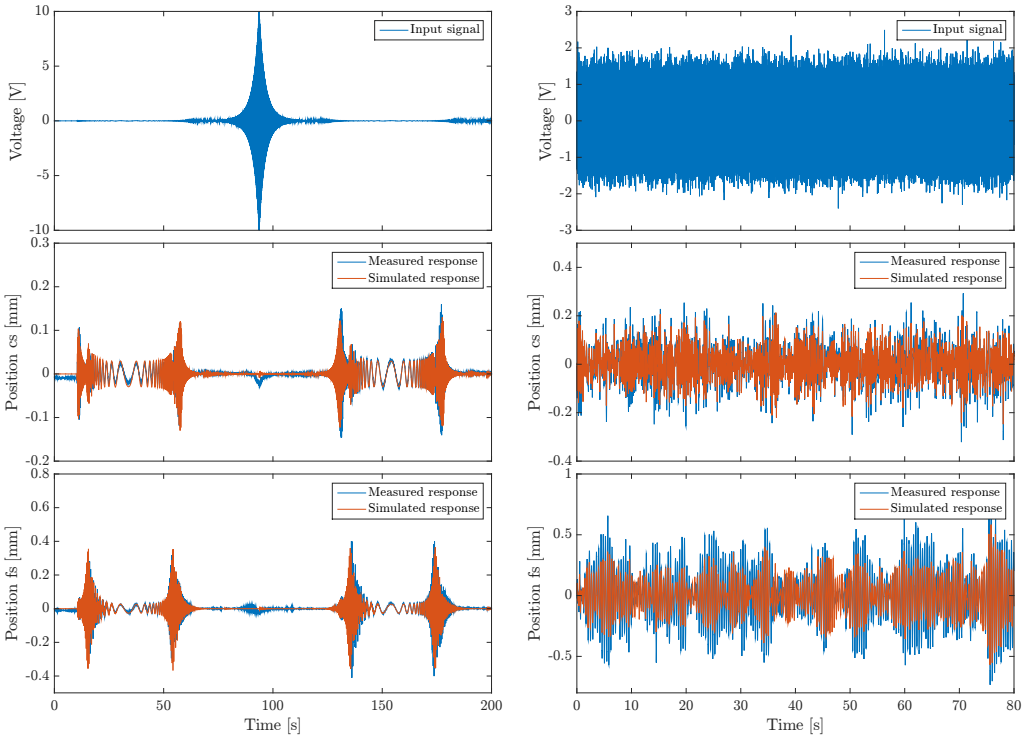

Figure 4.7: Validation of the identified system. Simulated response versus measured response of a (a) chirp signal and (b) white noise signal. The calculated VAF is 97.6 % and 97.2 % respectively.

Table 4.3: Identified parameters of (a) coarse stage and (b) fine stage.

(a)

Parameter	Value
m_{cs}	2.34 kg
c_{cs}	17 Ns/m
k_{cs}	2000 N m
K_{motor}	2.1 N/V

(b)

Parameter	Value
m_{fs}	0.57 kg
c_{fs}	0.28 Ns/m
k_{fs}	146 N m
$K_{Lorentz}$	0.55 N/V

5
Methods

In this chapter both experimental methods and simulation methods are presented. After introducing practical implementation of the CRONE reset controller, practical open-loop identification methods are presented. Then follows an explanation of the simulation method used for computing open-loop describing function. This method is validated using practical results retrieved from the separate fine stage system. Finally, the validated method is used to investigate sampling effects on the open-loop response.

5.1. Experimental methods

5.1.1. Control implementation

A generalized discrete state-space model of the combined reset- and non-reset controller is made for control implementation. It consists of a series interconnection between the reset controller and the non-reset controller and a parallel interconnection of the PI+CI approach-inspired convex combination structure such as is shown in figure 3.2. The discrete formulation of the implemented controller is taken as in [39]:

$$\Sigma_c : \begin{cases} x[k+1] = A_d x[k] + B_d e[k], & \text{if } e[k] \neq 0 \\ x[k+1] = A_d(A_\rho x[k]) + B_d e[k], & \text{if } e[k] = 0 \\ u[k] = C_d x[k] + D_d e[k] \end{cases} \tag{5.1}$$

in which A_d, B_d, C_d, D_d are the discrete state-space matrices of the generalized controller, A_ρ is the reset matrix and $e[k]$ and $u[k]$ are the error signal and control input signal respectively. When $A_\rho = I$, Σ_c will simplify to its linear base system. The discrete state-space matrices are found by using the MATLAB function `c2d` with an appropriate sampling frequency on the continuous state-space of the generalized

controller, given by:

$$A = \left[\begin{array}{cc|c} \begin{bmatrix} A_r & O \\ O & A_r \end{bmatrix} & & O \\ \hline B_{nr}\begin{bmatrix}(1-p)C_r & pC_r\end{bmatrix} & & A_{nr} \end{array}\right] \tag{5.2}$$

$$B = \left[\begin{array}{c} \begin{bmatrix} B_r \\ B_r \end{bmatrix} \\ \hline B_{nr}D_r \end{array}\right] \tag{5.3}$$

$$C = \left[\begin{array}{cc|c} D_{nr}\begin{bmatrix}(1-p)C_r & pC_r\end{bmatrix} & & C_{nr} \end{array}\right] \tag{5.4}$$

$$D = D_{nr}D_r \tag{5.5}$$

$$A_\rho = \begin{bmatrix} \gamma & O \\ O & I \end{bmatrix}. \tag{5.6}$$

The derivation can be found in appendix C.

5.1.2. Practical open-loop identification

The sensitivity function and complementary sensitivity function are estimated using experimental data recorded for different CRONE reset controllers using the MATLAB function `etfe`. A chirp signal is added at the measurement noise position in the control loop for identification of the sensitivity function $S(j\omega)$ and complementary sensitivity $T(j\omega)$ as can be found in figure 5.1. Sensitivity function is retrieved from the transfer from signal n to $y+n$ and complementary sensitivity function is retrieved from the transfer from $-n$ to y. In order to validate that increasing

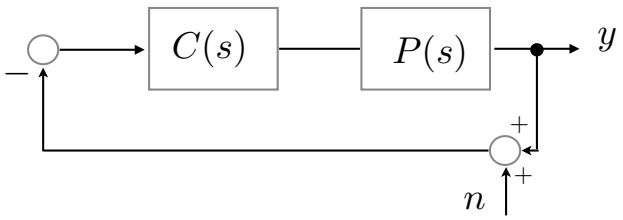

Figure 5.1: Block diagram showing signal n which is the frequency sweep used for identification of sensitivity function $S(j\omega$ and complementary sensitivity function $T(j\omega)$.

non-linearity in the controller adds phase in the open loop, the open-loop response is estimated using power spectral analysis methods as in [40]. The complementary sensitivity can be approximated using following power spectral densities (PSDs):

$$T(j\omega) = \frac{S_{y,-n}(j\omega}{S_{n,n}(j\omega)} \tag{5.7}$$

where $S_{y,u}(j\omega)$ is the power spectral density from a signal u to y. The sensitivity function can be approximated using:

$$S(j\omega) = \frac{S_{y+n,n}(j\omega)}{S_{n,n}(j\omega)}. \tag{5.8}$$

Then the open-loop is found by division of $T(j\omega)$ in (5.7) and $S(j\omega)$ in (5.8), given using division of following PSDs:

$$L(j\omega) = \frac{S_{y,-n}(j\omega)}{S_{y+n,n}(j\omega)}. \tag{5.9}$$

A chirp signal is used for identification and is composed of a bidirectional and logarithmic frequency sweep of 0.1 Hz to 2.5 kHz with a target time of 120 s for a time duration of 480 s and an amplitude of 1 μm. As the position sensor has a limited resolution, a filter $F(j\omega)$ is used such that the output response is kept larger than this minimal resolution. The gain of the transfer from n to y is given by complementary sensitivity function $T(j\omega)$. Then a 1:1 transfer is achieved if the filter is its inverse: $F(j\omega) = T^{-1}(j\omega)$. A second order filter is used to approximate $T(j\omega)$. Then to maintain a rational filter, $F(j\omega)$ is multiplied by a low pass filter.

5.2. Simulation method

5.2.1. Simulation of open-loop describing function

In [4] the describing function is computed using a Simulink model where the transfer from sine input to output of a non-linear system is approximated for a range of frequencies.

The describing function, mathematically given by the integral in (1.10), is computed with the Simulink model shown in figure 5.2.

In this model describing function is computed in open-loop, for which the CRONE reset controller and plant are placed in series at the location of *'Nonlinearity Under Test'*. However, practical results generally use closed-loop results to derive open-loop response. Thus the alternative model, shown in figure 5.3, is used that approximates the describing functions of the sensitivity function and complementary sensitivity function. Then the open-loop response is found as a division of these functions as in (5.9).

5.2.2. Validation of simulation method

For validation of the simulation method, several practical identified open-loop responses are compared to simulated describing function of the open-loop responses for the separate fine stage system. As for validation it is not relevant which base controller is used, following open-loop responses are shown for three different scenarios

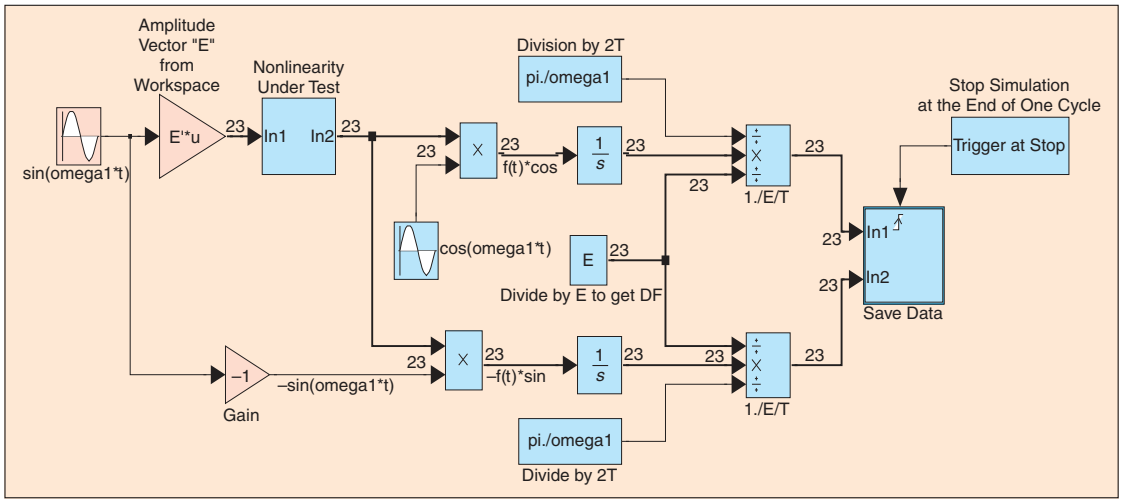

Figure 5.2: Simulink model for describing function generation. Adapted from [4].

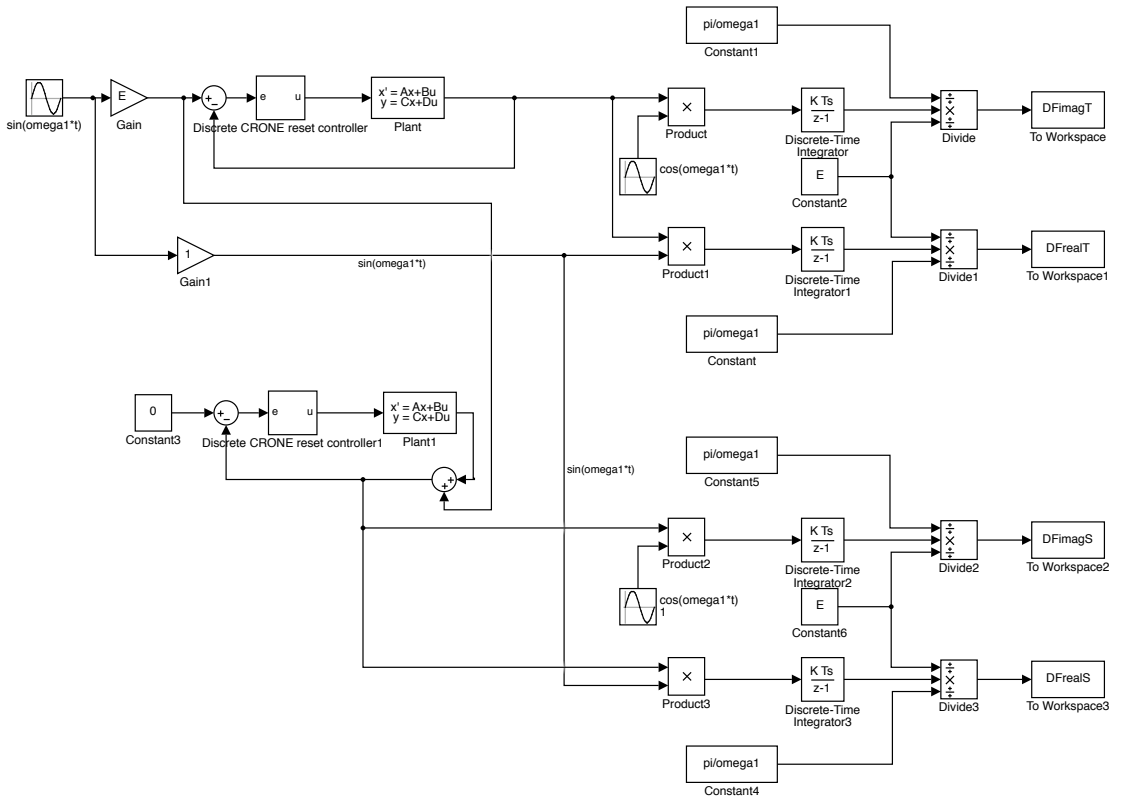

Figure 5.3: Proposed Simulink model for generation of describing function.

Table 5.1: Parameter values for CRONE-2 controllers.

Symbol	Parameter	Value
PM	phase margin	55°
ω_{cg}	bandwidth	100 Hz
ω_b	lag corner frequency	12.5 Hz
ω_h	lead corner frequency	800 Hz
ω_I	integrator corner frequency	8.33 Hz
ω_F	low-pass filter corner frequency	1200 Hz
n_I	integrator order	2
n_F	low-pass filter order	3

using second generation CRONE as a base controller. The control parameters are chosen as enlisted in table 5.1.

Open-loop responses for CRONE-2 lag-lead reset and CRONE-2 lag reset are shown in figures 5.4 and 5.5 for CRONE-2 lag-lead with p constant and varying γ and with γ constant and varying p respectively. Figure 5.6 shows the results for CRONE-2 lag reset for varying γ. In practical identification control effort increased for decreasing p and γ as a result of larger open-loop gain before bandwidth. As the position sensor is limited in resolution, chirp amplitude of 1 μm was chosen for identification. However, the increased control effort in case of smaller values for p and γ caused the controller to saturate. Thus $p = 0.5/\ \gamma = 0.5$ is used in all practical cases to avoid saturation. For comparability simulated open-loop responses are computed using the same values for p and γ.

The open-loop responses are shown in three cases. In the first, the analytical describing function is simulated, using (3.31). These responses are shown in subfigures (a). In the second case, simulated describing functions of open-loop response are computed as explained in 5.1.2. These are depicted in subfigures (b). In the third case, open-loop responses are identified using practical results with a sampling frequency of 10 kHz. It can be observed that the phase behaviours in subfigures (b) and (c) are very similar for frequencies above about 10 Hz. Below this frequency the coherence of the signals for identification of sensitivity function is very low, which makes the identified frequency response unreliable in this region. The similarity in simulated and identified open-loop validates the simulation method.

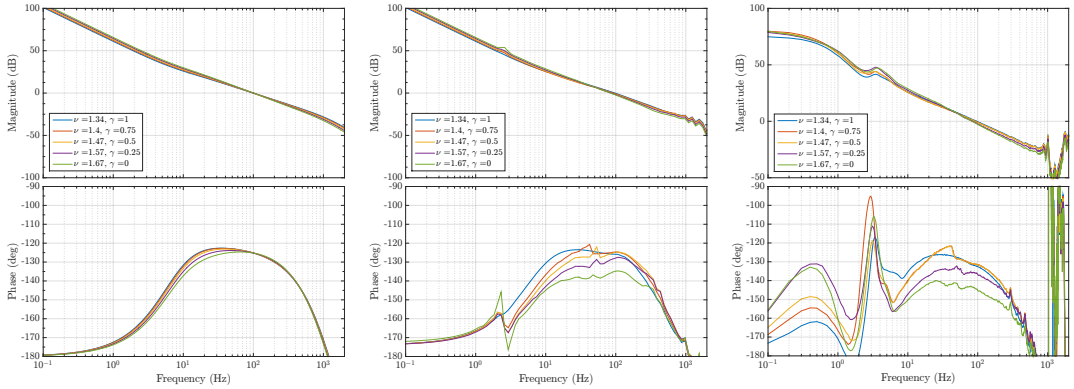

Figure 5.4: Open loop responses for CRONE-2 lag-lead reset for $p = 0.5$ and different values for γ. (a) Ideal case, (b) from simulated system response, (c) from experimental measurements.

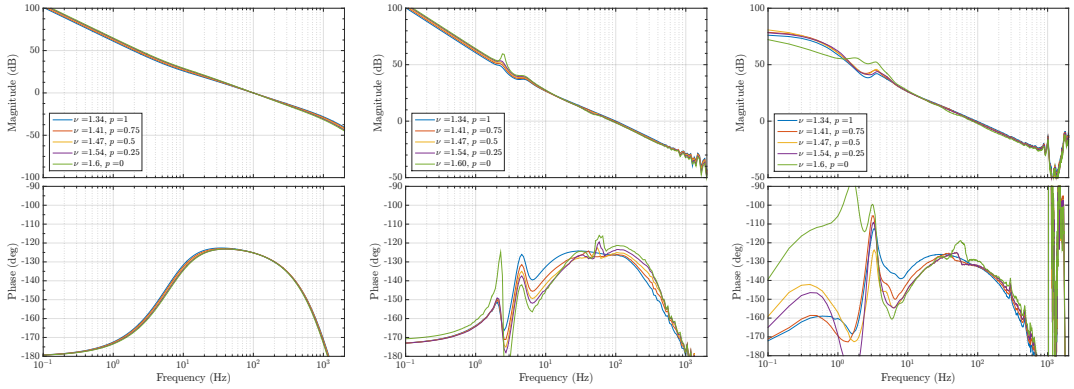

Figure 5.5: Open loop responses for CRONE-2 lag-lead reset for $\gamma = 0.5$ and different values for p. (a) Ideal case, (b) from simulated system response, (c) from experimental measurements.

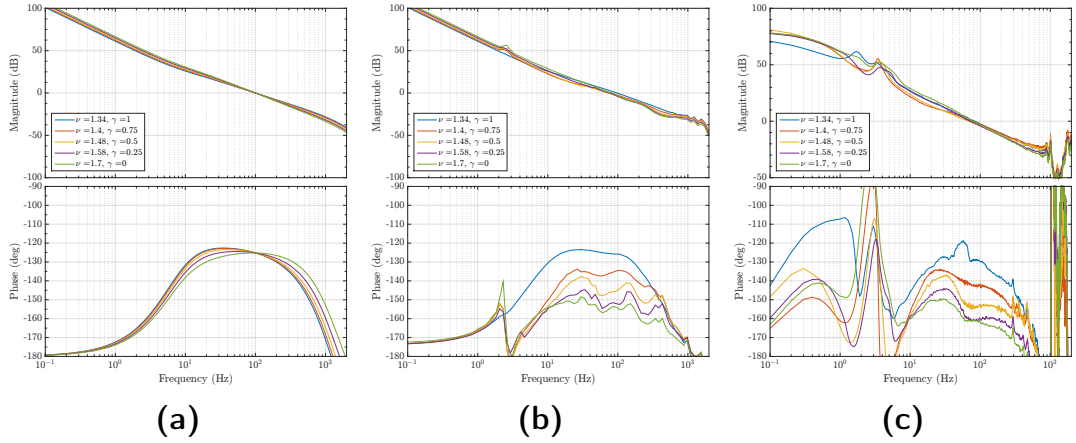

Figure 5.6: Open-loop responses for CRONE-2 lag reset for $p = 0.5$ and different values for γ. (a) Ideal case, (b) from simulated system response, (c) from experimental measurements.

5.2.3. Reduction of reset phase lead due to sampling

In the simulated and practical open-loop responses in figure 5.4 and 5.6 less phase lead is achieved with reset than expected, which decreases phase margin. The hypothesis is that phase reduction is caused by sampling effects. If the sampling frequency is reduced, the reset instant will be delayed. This causes the phase to drop. Simulation results of open-loop response for different sampling frequencies are obtained in figure 5.7. Stronger reduction of reset phase lead is indeed present for lower sampling frequency. Hence in further experimental implementation of CRONE reset controllers maximum sampling frequency of 20 kHz is used.

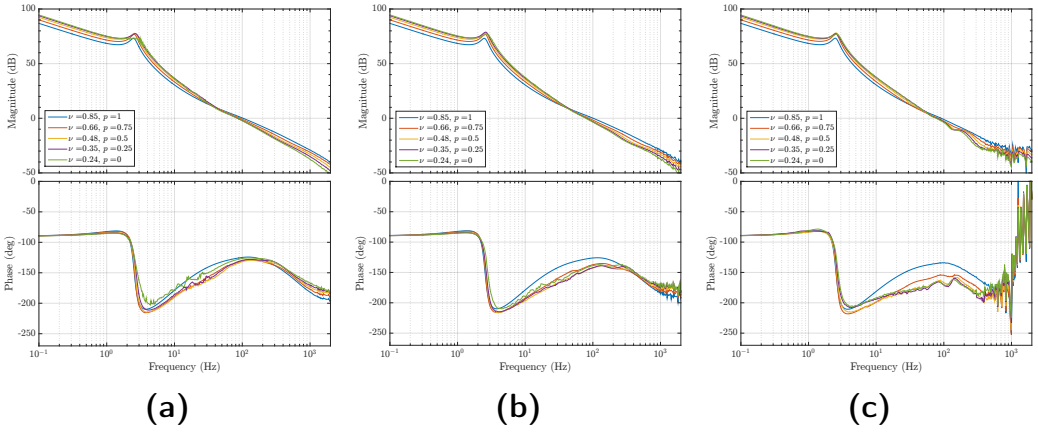

Figure 5.7: Simulated open-loop describing function for CRONE-1 lag reset control with $\gamma = 0$ and sampling frequency of (a)50kHz, (b) 20kHz and (c) 5kHz.

6

Preliminary reset strategy selection

In this chapter a selection of most promising reset strategies is made using both simulated open-loop describing functions and preliminary experimental results. Firstly, using the validated simulation method of previous chapter, open-loop describing functions are computed and compared for the reset strategies of integrator-, lag- and lag-lead filter. Then preliminary results are shown and compared for these three CRONE reset strategies. Finally, the results are summarized and the most promising strategy is chosen.

6.1. Simulated open-loop response

6.1.1. CRONE-1 reset

$\gamma = 0.5$ varying p

Using the validated simulation method, CRONE-1 integrator-, lag- and lag-lead reset are compared to each other for $\gamma = 0.5$ and sampling frequency of 20kHz. The simulated open-loop responses can be found in figure 6.1.

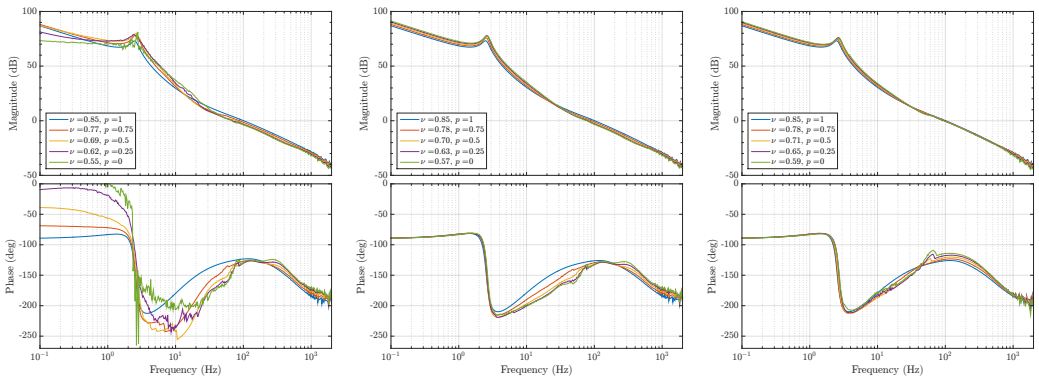

Figure 6.1: Simulated open-loop describing function CRONE-1 (a) integrator reset, (b) -lag reset and (c) -lag-lead reset for $\gamma = 0.5$ and sampling frequency of 20kHz.

$p = 0.5$ varying γ

Open-loop describing functions for CRONE-1 integrator-, lag- and lag-lead reset are compared to each other for $p = 0.5$ and varying γ. The simulated open-loop responses can be found in figure 6.2.

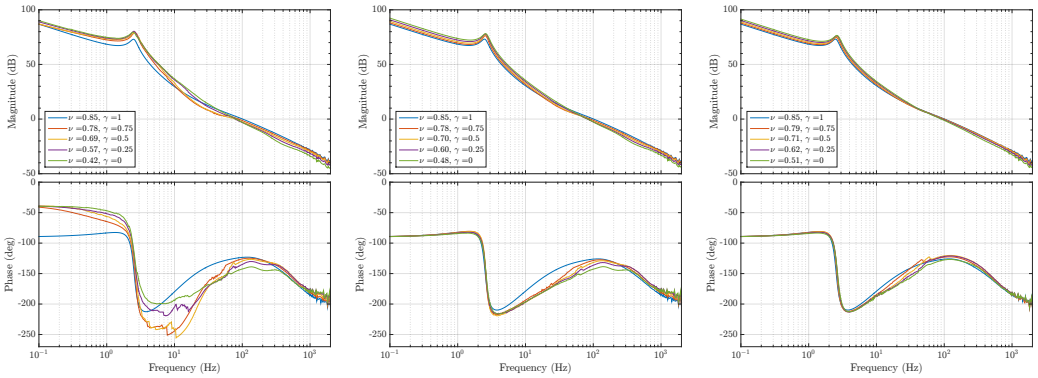

Figure 6.2: Simulated open-loop describing function CRONE-1(a) integrator reset, (b) -lag reset and (c) -lag-lead reset for $p = 0.5$ and sampling frequency of 20kHz.

For the simulated CRONE-1 reset open-loop responses shown in the remainder of this paragraph, for both integrator reset and lag-reset less reset phase lead is achieved than designed for using analytical describing function. This is about 10° less than expected according to theory. In the integrator reset open-loop at low frequencies the gain is even decreasing for more non-linearity, which is exactly opposing the goal of CRONE reset control. Additionally, decrease of phase in the frequency range before bandwidth is observed in both integrator- and lag-reset, degrading robustness of the system. In last figure for lag-lead reset on the other hand, more reset phase lead is created than expected.

6.1.2. CRONE-2 reset

$\gamma = 0.5$ varying p

CRONE-2 integrator-, lag- and lag-lead reset are shown for $\gamma = 0.5$ and varying p in figure 6.3. For integrator reset the low frequency describing functions are not shown. Due to numerical problems in Simulink, infinite responses prohibited the simulations, which are expected to have poor coherence at low frequency anyway.

$p = 0.5$ varying γ

CRONE-2 integrator-, lag- and lag-lead reset are shown for $p = 0.5$ and varying γ in figure 6.4. CRONE-2 integrator reset is shown for frequencies above 10 Hz.

Besides the reduction of phase lead around bandwidth in both integrator reset- and lag reset strategies in CRONE-2 reset open-loop describing functions, another observation is the reduction of phase around plant resonance peak of 2.5 Hz. Increasing non-linearity appears to increase the Q-factor of the plant as the open-loop gain becomes larger, causing the phase to drop.

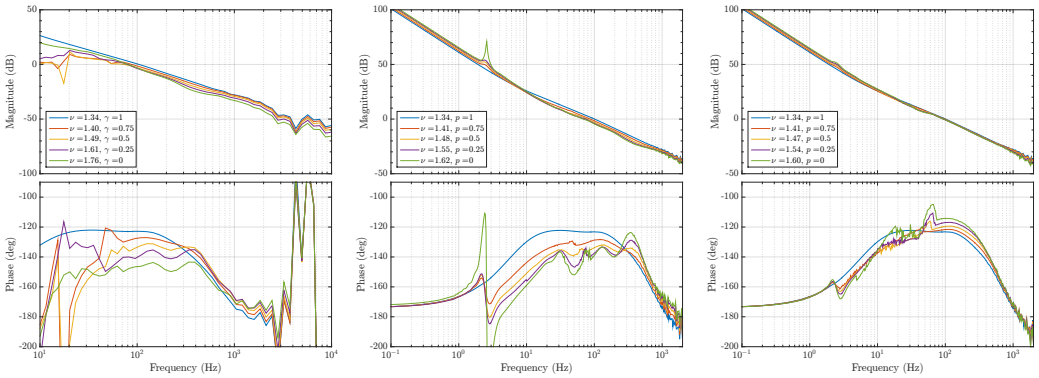

Figure 6.3: Simulated open-loop describing function CRONE-2 (a) integrator reset, (b) -lag reset and (c) -lag-lead reset for $\gamma = 0.5$ and sampling frequency of 20kHz.

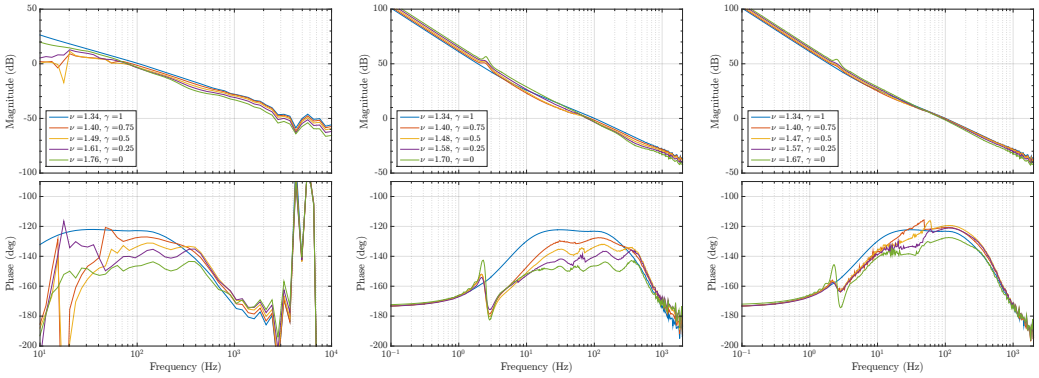

Figure 6.4: Simulated open-loop describing function CRONE-2(a) integrator reset, (b) -lag reset and (c) -lag-lead reset for $p = 0.5$ and sampling frequency of 20kHz.

6.1.3. Additional phase and reduced open-loop gain near reset corner frequency

In previous chapter some remarks have already been made about discrepancy between analytical open-loop describing function and simulated open-loop describing function. It was hypothesized that sampling reduces reset phase lead, which was supported by simulation results that showed phase reduction for lower sampling frequencies.

In the above figures another effect stands out. In the simulated describing functions of open-loop for integrator reset, the reset phase lead is more than expected. Using (3.37) for $\gamma = 0.5$ and $p = 0$ the phase lead is 23° whereas figure 6.1a shows at least 90° phase lead at low frequencies. Also the open-loop gain decreases at low frequency. Similar effects are evident in the lag-lead reset results, where ex-

tra phase lead is achieved around bandwidth with respect to analytical prediction. Some decrease in open-loop gain occurs, particularly in the frequency range between roughly 50 Hz and 90 Hz. This additional phase lead and reduction of loop-gain is hypothesized to be caused as explained in following paragraphs.

For a sinusoidal zero-mean error signal the reset instants are well-defined in open-loop. However, in closed-loop the reset instants depend on system response, which varies for different controller settings and is plant-specific. In closed-loop the main task of the controller is to steer the error between reference and output to zero. The error will therefore fluctuate around zero. This allows for more resets to occur. As delay of reset instants (sampling) is expected to create phase lag, earlier reset instants are thus hypothesized to create additional phase lead.

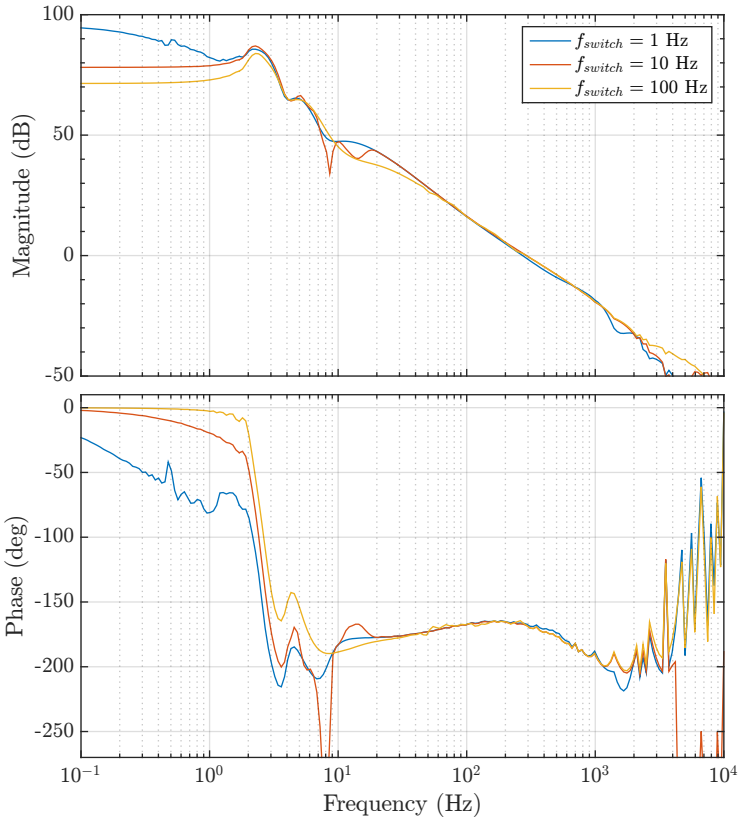

Figure 6.5: Direct open-loop response describing function from simulation for sampling frequency of 20 kHz, γ and different reset switching frequencies (fixed reset times). Higher switching frequencies create additional phase and reduces low frequency open-loop gain.

This hypothesis is tested by implementing fixed-time resets in the direct open-loop simulation for different resetting frequencies. The results are shown in figure 6.5 for CRONE-1 controller with fine stage plant. For increasing resetting frequency, phase

lead is increased and loop-gain is reduced at low frequencies, which is in agreement with given hypothesis. However, further research is required for confirmation.

6.2. Preliminary results

6.2.1. Reference tracking of an input-shaped scanning wave

Fourth-order trajectory planning is applied for computing a smoothed trajectory using [41]. Restrictions on maximal allowed velocity, acceleration and the higher order derivatives jerk and snap are used in generating a motion profile. In the same paper, a fourth-order feedforward is suggested for double mass systems and rigid-body (second-order) feedforward is suggested for improving tracking error. This feedforward provides the necessary DC gain to avoid possible limit cycles as introduced in 2.2.2. As the fine stage shows second-order behaviour, a second-order feedforward is implemented. The transfer function of the feedforward is given as:

$$FF(s) = (m_{fs}s^2 + c_{fs}s + k_{fs})/K_{Lorentz}X_{fs}(s) \tag{6.1}$$

All three reset strategies were implemented on the setup for $\gamma = 0.5$ and $p = 0.25$ in figure 6.6 for similar CRONE-1 base linear controllers. As can be seen in this figure, the control input peaks are the highest for integrator reset, which is as expected since most non-linearity is introduced in integrator reset (most phase lead created in integrator case). In the constant velocity regions of the trajectory some spikes appear in measured position, especially for integrator and lag reset strategies. These are believed to be caused by parasitic non-linearities created by the large control input peaks. Although these tracking results seem optimistic for all three strategies, the next paragraph presents a contrasting picture.

6.2.2. Gaussian input-disturbance rejection

For a zero-mean Gaussian input-disturbance signal with variance of 0.01, the output response and the control input voltage are analysed for the three reset strategies for CRONE-1 reset. In order to make a more fair comparison between the reset strategies, the same value of γ is taken and p is calculated in such a way that the same reset phase lead is achieved according to (3.35) to (3.37). For a reset phase lead of 10 degrees the results are shown in figure 6.7. It can be seen that the control input peaks in CRONE-1 integrator reset are high, some of the peaks even go over 5 V. Thus integrator reset is identified as the least advantageous reset strategy, whereas lag-lead reset is identified as the most advantageous.

6.3. Selected reset strategies

Both from simulated open-loop response and practical results comparing the three reset transfer function parts, the lag-lead reset has been identified as most beneficial reset strategy. In simulations sufficient phase was achieved, taken into account

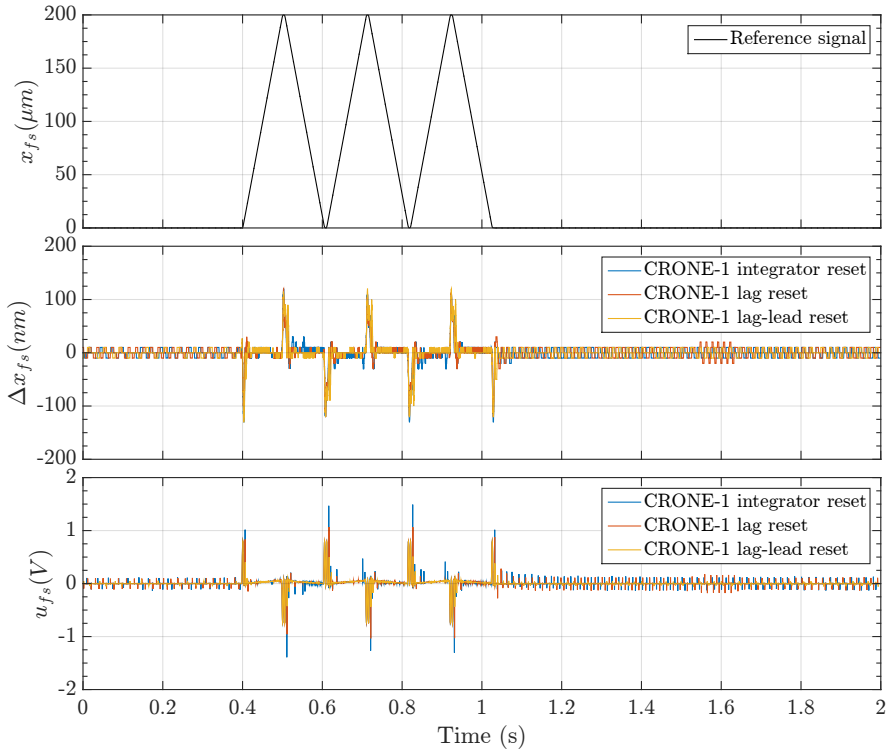

Figure 6.6: Reference-tracking of a triangular scanning motion for CRONE-1 integrator reset, lag reset and lag-lead reset with $\gamma = 0$ and $p = 0.25$.

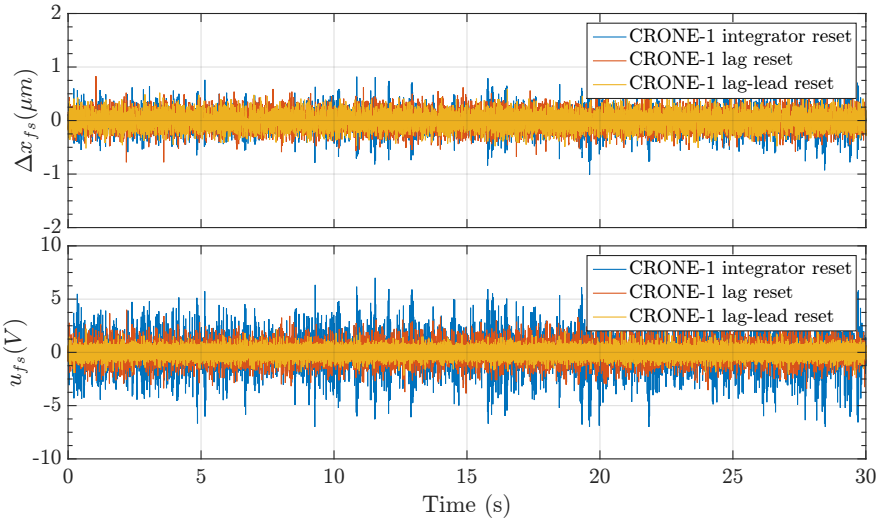

Figure 6.7: Response and control input to a zero-mean Gaussian input disturbance response with variance 0.01 for $\gamma = 0.5$ and reset phase lead of 10°.

the effect of discretization. Furthermore, this reset strategy is identified as the least sensitive to disturbance rejection. Thus for the further investigation of system performance, lag-lead reset will be analysed for both first generation- and second generation CRONE.

For the identified fine stage plant, transfer function of (4.1) is used in the control design of CRONE-1 reset- and CRONE-2 reset controllers. The corresponding open-loop responses of the considered linear CRONE-1 and CRONE-2 controllers are shown in figure 6.8.

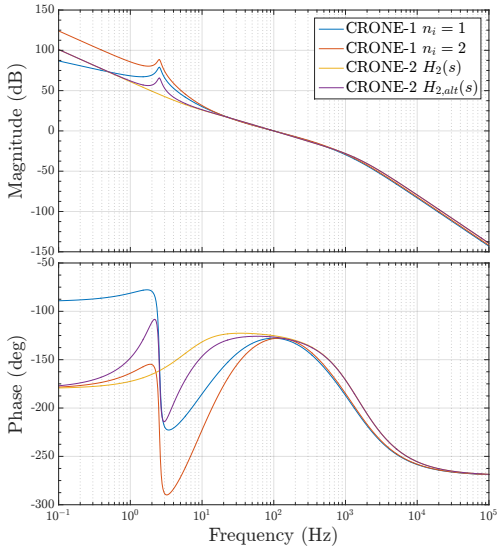

Figure 6.8: Bode-plot of open-loop for linear CRONE-1 and CRONE-2 controllers on which lag-lead reset will be performed.

The selected controller parameters are shown in table 6.1. For CRONE-1 the integrator order $n_i = 1$ is chosen, as $n_i = 2$ decreases robustness for frequencies before bandwidth. In the second generation CRONE design inverse plant is used. The Q-factor is taken lower such that dips caused by model mismatches are avoided. This is explained in the given guidelines in chapter 9.4.2. In (4.1) a damping of $c_{fs} = 10$ is chosen. For this alternative plant transfer function $H_{2,alt}(S)$ and the identified plant transfer $H_2(s)$, the open-loop responses are both shown. From the Bode-plot it appears that CRONE-2 will be more robust than CRONE-1.

Table 6.1: Parameters of base controller CRONE-1 and CRONE-2

Symbol	Parameter	Value CRONE-1	Value CRONE-2
PM	phase margin	55°	55°
ω_{cg}	bandwidth	100 Hz	100 Hz
ω_b	lead corner frequency	12.5 Hz	12.5 Hz
ω_h	lag corner frequency	800 Hz	800 Hz
ω_I	integrator corner frequency	8.33 Hz	8.33 Hz
ω_F	low-pass filter corner frequency	1200 Hz	1200 Hz
n_I	integrator order	1	2
n_F	low-pass filter order	1	3
N	Oustaloup approximation order	4	4

7

Experimental validation: fine stage

In this chapter the performance of the most promising CRONE reset strategy, namely lag-lead reset as shown in chapter 6, is validated on the fine stage. An analysis of reference-tracking performance and noise performance of the CRONE reset controlled systems are presented. Then practical open-loop responses are shown and finally disturbance rejection behaviour is analysed.

7.1. Reference-tracking performance

7.1.1. Frequency domain

Complementary sensitivity function $T(j\omega)$ has been identified using methods as explained in 5.1.2. The identified complementary sensitivity function for a CRONE-1 lag-lead reset controller with $\gamma = 0.5$ and varying parameter p is shown in figure 7.1a for a bandwidth of 100 Hz. The coherence function is shown in 7.1b. It can be seen that the gain at peak has decreased, giving better tracking performance, but the gain has also reduced at high frequencies beyond bandwidth, resulting in better noise performance compared to the linear case.

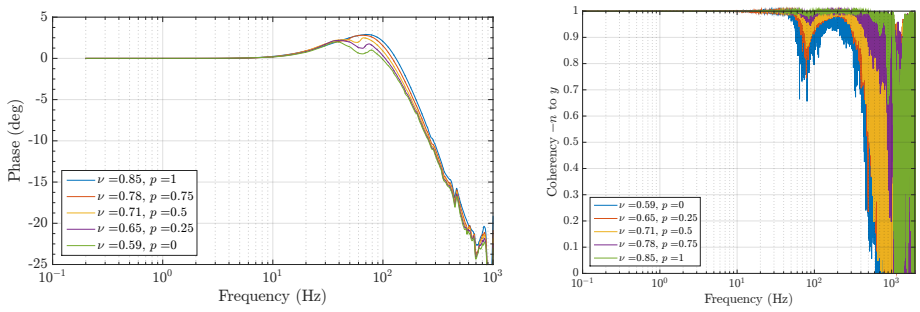

(a) (b)

Figure 7.1: (a) Identified complementary sensitivity $T(j\omega)$ for CRONE-1 lag-lead reset with $\gamma = 0.5$ and varying p.(b) Coherence function from transfer from reference to output signal.

Similar results have been retrieved for a CRONE-2 lag-lead reset controller in figures 7.2a and 7.2b. This is contrasting to what is expected of waterbed effect, that predicts an increase at some other frequency range. Thus some relief has been achieved from waterbed effect.

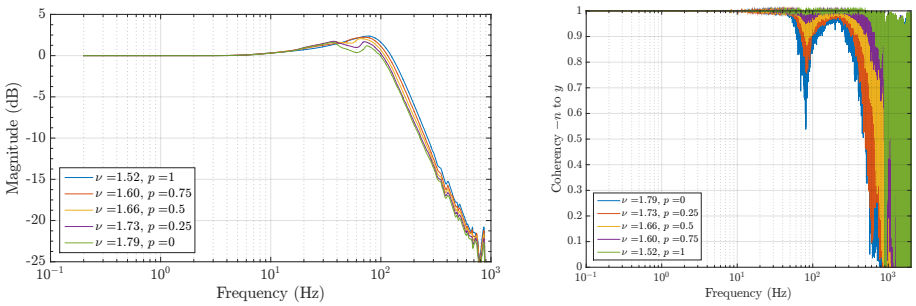

(a) (b)

Figure 7.2: (a) Identified complementary sensitivity $T(j\omega)$ for CRONE-2 lag-lead reset with $\gamma = 0.5$ and varying p. (b) Coherence function from transfer from reference to output signal.

7.1.2. Time domain

Triangular wave reference

A triangular scanning signal with amplitude of 400 µm peak-to-peak is given as a reference signal. The acceleration of this trajectory is limited to $0.25\,\mathrm{m/s^2}$ and velocity to $3\,\mathrm{mm/s}$.

In figure 7.3 it can be seen that the error of the displacement in the fine stage position is reduced for increasing non-linearity. The RMS errors are enlisted in table 7.1a for CRONE-1 lag-lead reset and table 7.1b for CRONE-2 lag-lead reset. In CRONE-1 lag-lead reset control, the RMS error has been reduced from 22.10 nm to 17.92 nm. For CRONE-2 lag-lead reset the RMS error reduces from 70.74 nm to 43.63 nm.

Table 7.1: RMS errors for tracking fourth-order triangular scanning reference with $\gamma = 0.5$ for (a) CRONE-1 lag-lead reset and (b) CRONE-2 lag-lead reset.

(a)

p	RMS error (nm)
1	22.10
0.75	20.42
0.5	19.56
0.25	19.07
0	17.92

(b)

p	RMS error (nm)
1	70.74
0.75	59.86
0.5	52.76
0.25	47.83
0	43.63

Step reference

For a step reference signal with amplitude of 400 µm, maximum acceleration of $0.05\,\mathrm{m/s^2}$ and maximum velocitiy of $75\,\mathrm{mm/s}$, reduction in RMS error is observed as

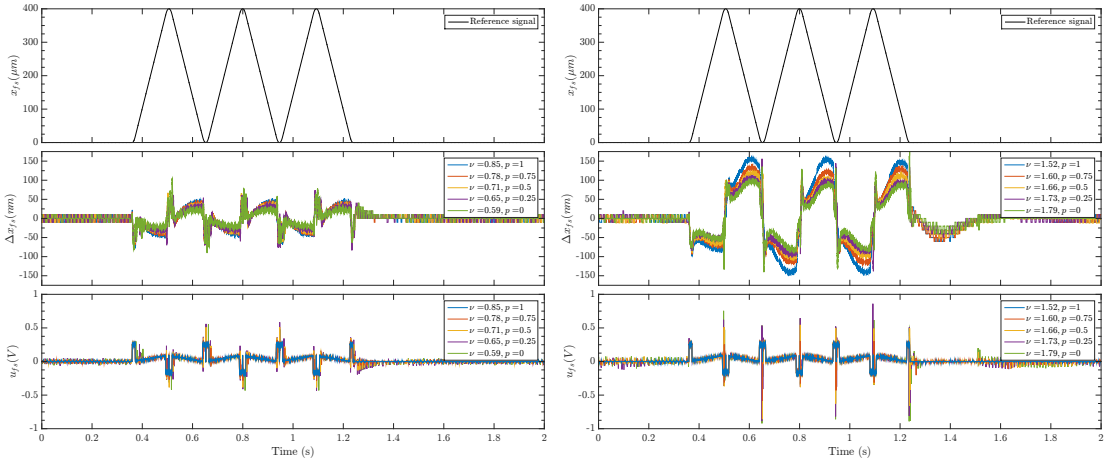

Figure 7.3: Reference-tracking of a fourth-order triangular scanning reference for lag-lead reset with $\gamma = 0.5$ for (a) CRONE-1 and (b) CRONE-2.

well. The measured signals for step reference tracking are shown in figure 7.4. RMS errors for CRONE-1 lag-lead reset control can be found in table 7.2a. The RMS error decreases from 13.04 nm to 9.51 nm for linear to full non-linear with $\gamma = 0.5$. The CRONE-2 lag-lead reset RMS errors are shown in table 7.2b. From this table it it can be seen that the RMS tracking error for linear to fully non-linear with $\gamma = 0.5$ reduces from 18.20 nm to 13.11 nm.

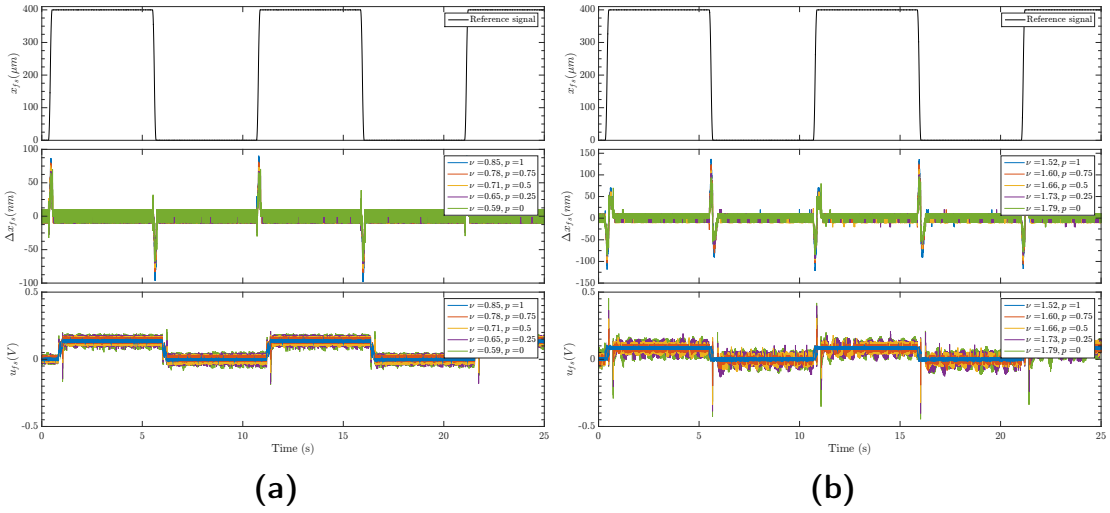

Figure 7.4: Reference-tracking of a fourth-order step reference with second-order feedforward for lag-lead reset with $\gamma = 0.5$ for (a) CRONE-1 and (b) CRONE-2.

The RMS errors for the CRONE-1 lag-lead reset controllers are smaller than for

Table 7.2: RMS errors for tracking fourth-order step reference with second-order feedforward and $\gamma = 0.5$ for (a) CRONE-1 lag-lead reset and (b) CRONE-2 lag-lead reset.

(a)

p	RMS error (nm)
1	13.04
0.75	11.86
0.5	10.94
0.25	10.15
0	9.51

(b)

p	RMS error (nm)
1	18.20
0.75	15.78
0.5	14.52
0.25	13.75
0	13.11

the CRONE-2 lag-lead reset controllers. As the chosen integrator order is larger for CRONE-2, this is contradicting expectations. A possible explanation is that the stiffness of the plant is larger than the identified value. In that case, the inverse of this value decreases open-loop gain at low frequencies. Nevertheless, decrease of RMS error observed for both CRONE-1- as CRONE-2 lag-lead reset controllers. This is sufficient to show effectiveness of the CRONE reset control concept.

7.2. Noise performance

7.2.1. Frequency domain

The identified sensitivity function $S(j\omega)$ has been found with same chirp signal from 0.1 Hz to 2.5 kHz introduced in 5.1.2. For a CRONE-1 lag-lead reset controller with $\gamma = 0.5$ and varying p, the sensitivity function can be found in figure 7.5a and the corresponding coherence function in figure 7.5b. The results for CRONE-2 lag-lead reset can be found in figures 7.6a and 7.6b. Here it can be seen that sensitivity peak reduces when more non-linearity is allowed in the system.

7.2.2. Time domain

Noise power is calculated for sine signals at different frequencies above bandwidth for a duration of 5 s. Reduction of noise is analysed for maximum reset phase lead, thus $\gamma = 0$ and $p = 0$, which is calculated as follows:

$$\frac{\bar{P}_{lin}}{\bar{P}_{non-lin}} = 10\log_{10}\left(\frac{x_{RMS,lin}}{x_{RMS,non-lin}}\right). \tag{7.1}$$

Noise reduction for CRONE-1- and CRONE-2 lag-lead reset with full reset with respect to linear base equivalent is shown in table 7.3. For all considered sinusoidal noise signals more noise reduction has been achieved.

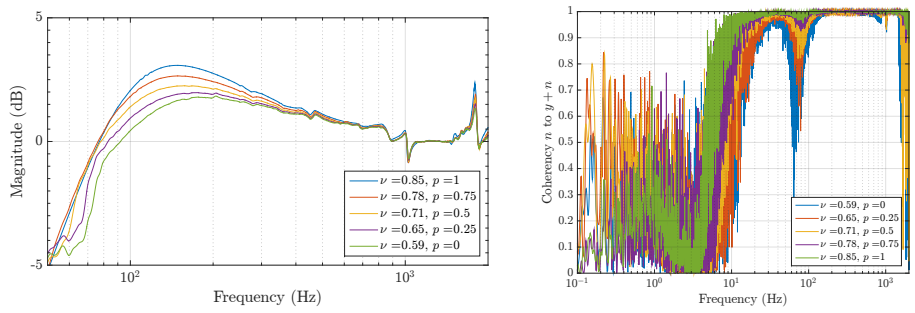

(a) (b)

Figure 7.5: (a) Experimental sensitivity function $S(j\omega)$ for a CRONE-1 lag-lead reset controller with $\gamma = 0.5$ and varying p and (b) the coherence function noise signal n and measured output $y + n$.

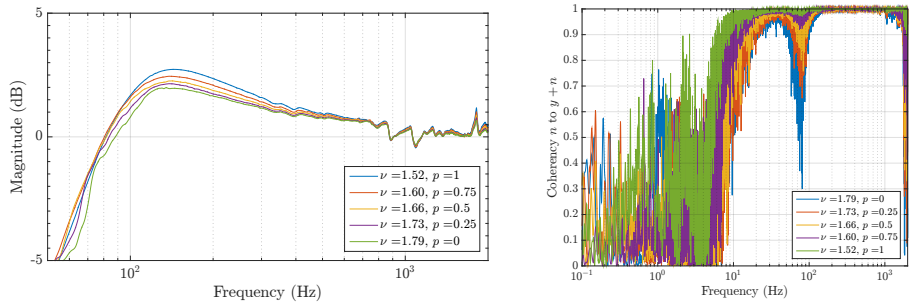

(a) (b)

Figure 7.6: (a) Experimental sensitivity function $S(j\omega)$ for a CRONE-2 lag-lead reset controller with $\gamma = 0.5$. (b) Coherence function between noise n and measurement output $y + n$.

Table 7.3: Noise reduction (a) CRONE-1 lag-lead reset and (b) CRONE-2 lag-lead full reset ($p = 0$, $\gamma = 0$) with respect to linear controllers.

(a)

f (Hz)	Noise reduction (dB)
300	2.46
400	2.74
500	2.72
600	2.98
700	2.66
800	2.57
900	1.79
1000	2.59

(b)

f (Hz)	Noise reduction (dB)
300	2.94
400	3.14
500	3.55
600	3.14
700	3.30
800	3.10
900	3.93
1000	2.92

7.3. Open-loop response

Division of complementary sensitivity and sensitivity function using PSDs as in (5.9) gives the open-loop response in figures 7.7 and 7.8 for CRONE-1 lag-lead reset and CRONE-2 lag-lead reset respectively. The CRONE reset control concept was introduced in 1.1.4 using a three-step procedure. In step 1, the robust linear CRONE controller is designed. These can be found in both subfigures (a) and (b) for $p = 1$. In step 2, reset control was applied to a robust CRONE controller without changing fractional order ν. This is depicted in subfigures (a). In step 3, the additional reset phase leads are used to achieve same phase margin for a better loop shape using a new value ν^*. This is shown in subfigures (b). In figure 7.8a, the smallest value for p chosen is $p = 0.1$ as the controller saturated for $p = 0$.

Because low coherence between signals n and $y + n$ exists in figure 7.7b and figure 7.8b at low frequencies (similar results were retrieved for figures 7.7a and 7.8a as well), the low frequency open-loop response is considered unreliable.

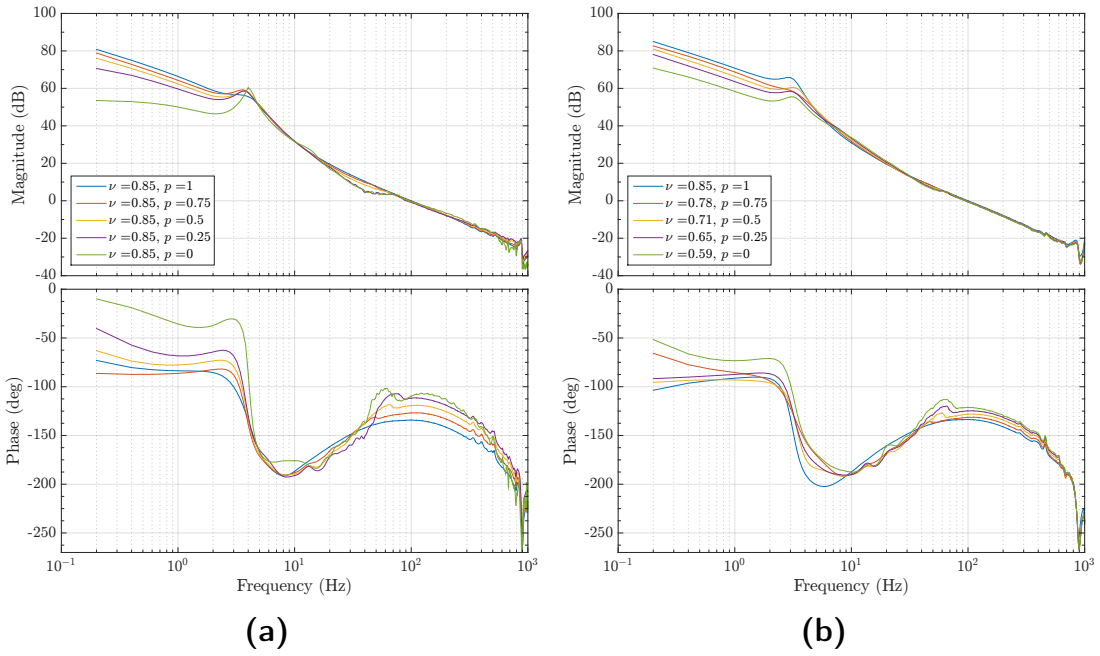

Figure 7.7: Experimental open-loop response for CRONE-1 lag-lead (a) with reset, same ν and (b) CRONE-1 lag-lead reset controller with new ν^* with $\gamma = 0.5$ and varying p.

It can be seen that loop-gain at high frequency becomes slightly worse when only reset is applied in subfigures (a). Then after retuning ν in subfigures (b) this effect is accounted for. Although improvement of the high frequency slope compared to linear case is not significant, still more phase is achieved for similar slopes. As such, relief from Bode's gain-phase relation has been achieved. The cause of additional reset phase and reduction in loop gain was already discussed in 6.1.3 and requires

further investigation. However, sufficient phase margin has been achieved for all CRONE-1 lag-lead reset controllers and CRONE-2 lag-lead reset controllers shown which satisfies design objectives.

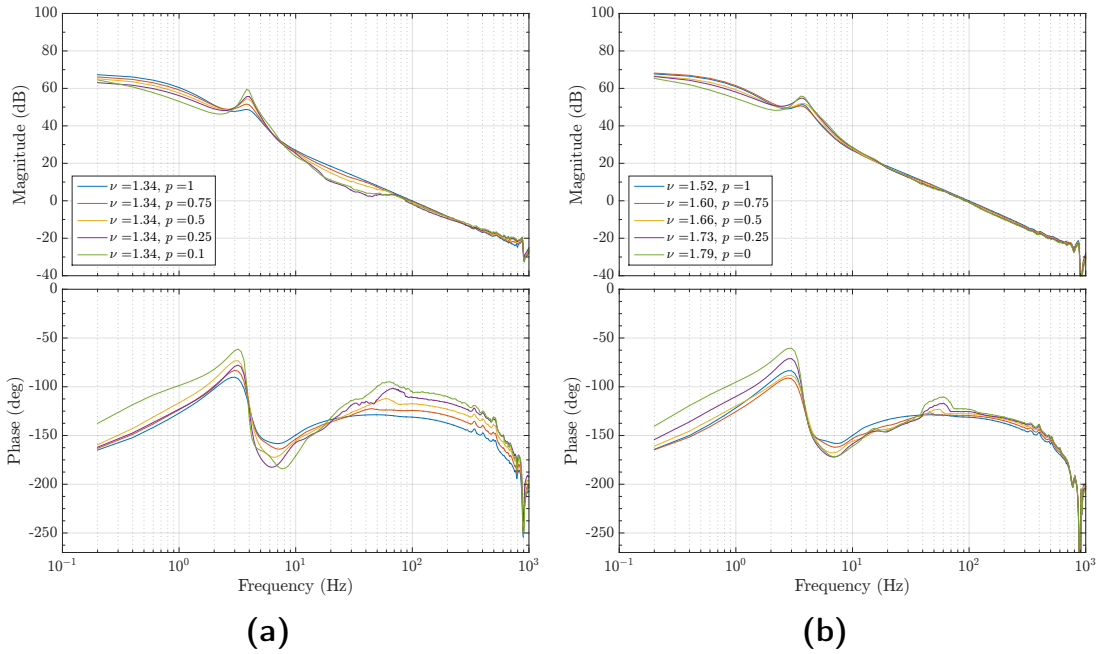

Figure 7.8: Experimental open-loop response for CRONE-2 lag-lead (a) with reset for same ν and (b) CRONE-2 lag-lead reset with $\gamma = 0.5$ and varying p.

Comparing open-loop responses of CRONE-1 lag-lead reset to CRONE-2 lag-reset, it appears that the flat phase behaviour is much more apparent in the CRONE-2 lag-lead reset controlled systems.

7.4. Disturbance rejection

7.4.1. Step disturbance

In figure 7.9 the response to an input step disturbance is shown for CRONE-1- and CRONE-2 lag-lead reset control. The settling time is defined as the time required to decrease to 15% of the maximum peak value. The computed settling times are shown in tables 7.10a and 7.10b for CRONE-1 lag-lead reset and CRONE-2 lag-lead reset respecticvely.

In CRONE-1 lag-lead reset, the settling time increased because secondary (and higher) peaks are created. Despite the fact that these additional peaks are also present in CRONE-2 case, the settling time reduces for increasing non-linearity, which is in line with expectations.

Maximum peak value slightly increased (30nm) in both CRONE-1 and CRONE-2 lag-lead reset.

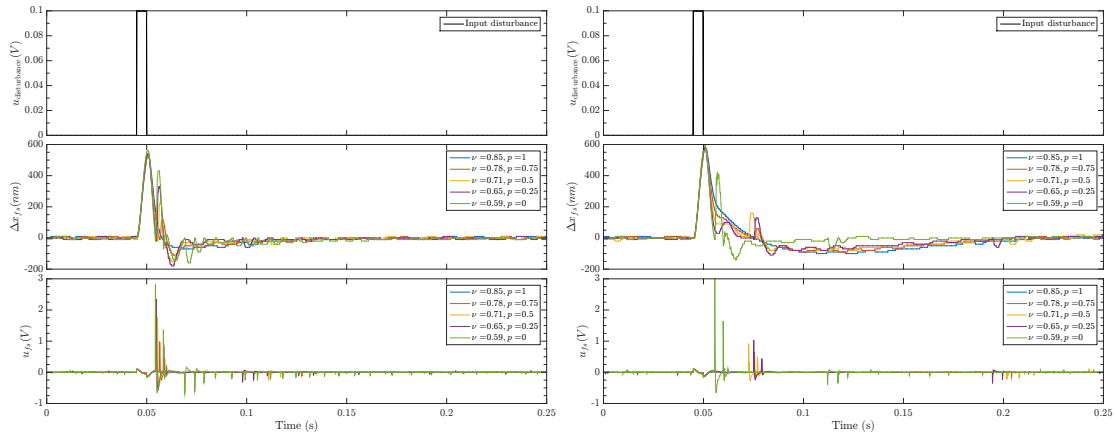

Figure 7.9: Response to a step disturbance for lag-lead reset with $\gamma = 0.5$ for (a) CRONE-1 and (b) CRONE-2.

Figure 7.10: Settling time to reach 15% of maximum peak value $\hat{x}_{fs}$ for (a) CRONE-1 lag-lead reset and (b) CRONE-2 lag-lead reset with $\gamma = 0.5$.

(a)

p	$\hat{x}_{fs}$ (nm)	settling time (ms)
1	530	55.8
0.75	540	65.5
0.5	540	65.5
0.25	550	66.0
0	560	76.8

(b)

p	$\hat{x}_{fs}$ (nm)	settling time (ms)
1	570	146.0
0.75	570	135.7
0.5	570	128.1
0.25	580	125.1
0	600	68.3

7.4.2. Gaussian disturbance

A zero-mean Gaussian disturbance with variance of 0.1 is applied at the control input and measured for a time span of 30 s. The cumulative power spectral density (CPSD) of the measured position is shown in figures 7.11a and 7.11b. In the CPSDs for CRONE-1 lag-lead reset no significant difference is present for different values of p. In figure 7.11b there appears to be slightly better rejection against Gaussian disturbance for increasing non-linearities with the exception of the full non-linear case with $p = 0$, $\gamma = 0.5$. For $p = 0.25$, $\gamma = 0.5$, the disturbance rejection has improved with 1.3 dB compared to linear case. Still, further investigation is required to better understand the effect of non-linear reset, as no systematic improvement in disturbance rejection has been observed with increasing non-linearity.

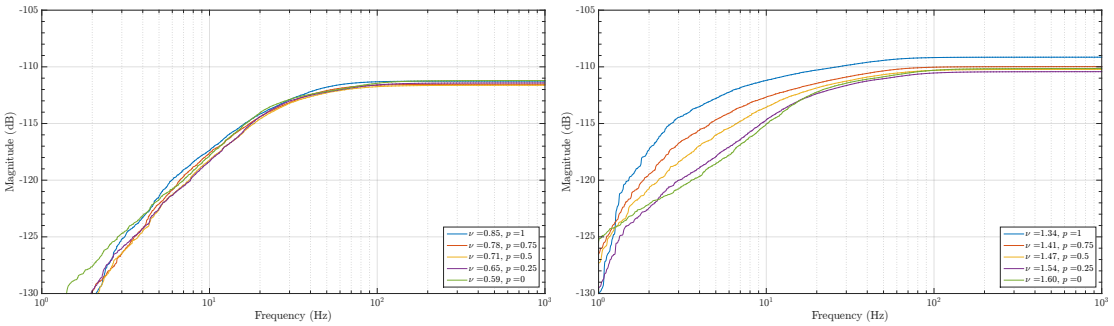

(a) (b)

Figure 7.11: Cumulative power spectral density of the measured response to a zero-mean Gaussian disturbance signal with variance 0.1 for (a) CRONE-1 lag-lead reset and (b) CRONE-2 lag-lead reset with $\gamma = 0.5$.

7.5. Stability analysis

Stability has been evaluated for the designed CRONE-1-/CRONE-2 lag-lead controllers that were practically implemented and shown in the results in this chapter. Both stability conditions given in subsection 3.4.2 are analysed below for the same controller, namely a CRONE-1 lag-lead reset controller with parameters as shown in table 7.4. The code used for implementations can be found in Appendix D.

Table 7.4: Parameter values for CRONE-1 lag-lead controller

Symbol	Parameter	Value
PM	phase margin	55°
ω_{cg}	bandwidth	100 Hz
ω_b	lead corner frequency	12.5 Hz
ω_h	lag corner frequency	800 Hz
ω_I	integrator corner frequency	8.33 Hz
ω_F	low-pass filter corner frequency	1200 Hz
n_I	integrator order	1
n_F	low-pass filter order	1
p	reset percentage	0.5
γ	partial reset	0.5
N	Oustaloup approximation order	4

7.5.1. $|\lambda(A_\rho e^{\frac{\pi}{\omega}A})|$-condition

Stability is firstly analysed using the $|\lambda(A_\rho e^{\frac{\pi}{\omega}A})|$-condition. For this condition the open-loop of reset controller Σ_r in series with non-reset controller Σ_{nr} and plant Σ_p

is considered. The open-loop A-matrix as given in (3.46) for the CRONE-1 lag-lead reset controller then becomes:

$$A_{ol} = \left[\begin{array}{cc|c} \begin{bmatrix} A_r & O \\ B_{nr}C_r & A_{nr} \end{bmatrix} & & O \\ \hline A_p & & B_p \begin{bmatrix} D_{nr}C_r & C_{nr} \end{bmatrix} \end{array}\right]. \tag{7.2}$$

The computed A_{ol} is as follows:

$$A_{ol} = \begin{bmatrix} -0.0002 & -0.0016 & 2.4958 & 1.0585 & 0.3960 & 0.0930 & 0.0309 & 0.0077 & 0.1620 \\ 0.0016 & 0 & 0 & 0 & 0 & 0 & 0 & 0 & 0 \\ 0 & 0 & -1.8695 & -0.7086 & -0.4016 & -0.1610 & -0.0810 & -0.0180 & 0 \\ 0 & 0 & 1.6384 & 0 & 0 & 0 & 0 & 0 & 0 \\ 0 & 0 & 0 & 0.4096 & 0 & 0 & 0 & 0 & 0 \\ 0 & 0 & 0 & 0 & 0.2048 & 0 & 0 & 0 & 0 \\ 0 & 0 & 0 & 0 & 0 & 0.0512 & 0 & 0 & 0 \\ 0 & 0 & 0 & 0 & 0 & 0 & 0.0256 & 0 & 0 \\ 0 & 0 & 0 & 0 & 0 & 0 & 0 & 01 & 0 \end{bmatrix} \times 10^4$$

and reset matrix A_ρ:

$$A_\rho = \text{diag}(0.5, I_8). \tag{7.3}$$

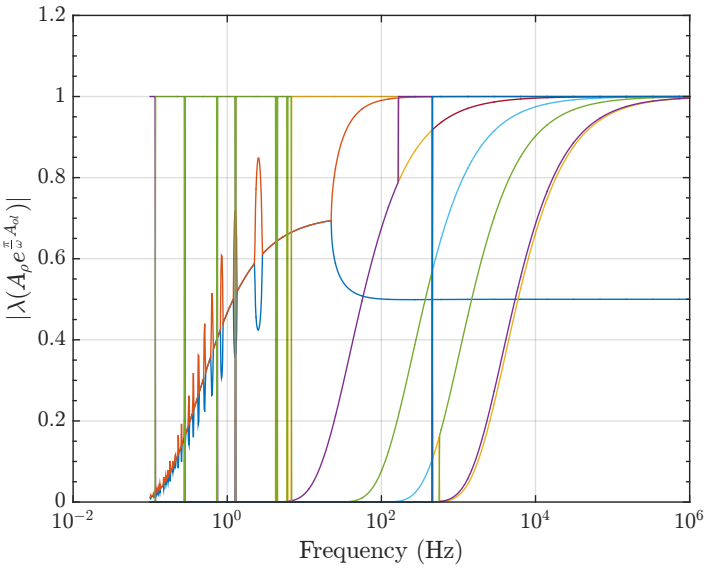

Figure 7.12: Eigenvalues of A_{ol}.

The eigenvalues of this system are plot in figure 7.12 against frequency. It can be seen that the eigenvalues make jumps to 1, showing this condition does not suffice in proving stability of the system.

7.5.2. H_β-condition

For the same CRONE reset controller and plant parameters the H_β-condition is analysed as given in 3.4.2. The normalized A_{cl}- and A^*_ρ-matrix are given by:

$$A_{cl} = \begin{bmatrix} -3.41 & -32.8 & 0 & 0 & 4.29\times10^{11} & 8.26\times10^{14} & 4.23\times10^{17} & 7.35\times10^{19} & 4.71\times10^{21} & \\ 32.8 & 0 & 0 & 0 & 0 & 0 & 0 & 0 & 0 & 0 \\ 0 & -0.491 & -161 & 0 & 0 & 0 & 0 & 0 & 0 & 0 \\ 0 & -0.491 & 0 & -161 & 0 & 0 & 0 & 0 & 0 & 0 \\ 0 & -0.008 & 79.3 & 79.3 & -3.82\times10^{4} & -2.35\times10^{8} & -5.34\times10^{11} & -4.12\times10^{15} & -8.46\times10^{16} & 0 \\ 0 & 0 & 0 & 0 & 2.05 & 0 & 0 & 0 & 0 & 0 \\ 0 & 0 & 0 & 0 & 0 & 2.05 & 0 & 0 & 0 & 0 \\ 0 & 0 & 0 & 0 & 0 & 0 & 2.05 & 0 & 0 & 0 \\ 0 & 0 & 0 & 0 & 0 & 0 & 0 & 2.05 & 0 & 0 \\ 0 & 0 & 0 & 0 & 0 & 0 & 0 & 0 & 2.05 & 0 \end{bmatrix} \times10^{-23}$$

and

$$A^*_\rho = \mathrm{diag}(0.5, I_9) \tag{7.4}$$

respectively.

The LMI as described in Theorem 3 is solved using Yalmip with a Sedumi solver. For $\beta = -8.99\times10^{-12}$ and $P_\rho = 0.98$ a solution has been found for P after normalizing A_{cl}. For the found P-matrix the eigenvalues are 2.88×10^{-11}, 1.70×10^{-3}, 0.98, 1.00, 1.00, 1.00, 1.00, 1.00, 1.00 and 2.00. Because the eigenvalues are all larger than zero, the found P is indeed positive definite. Thus quadratic stability is guaranteed.

8

Practical CRONE reset design: dual precision stage

In this chapter the increased tracking performance of CRONE reset control, which was validated on the fine stage in previous chapter, is used to improve the performance of a typical dual precision stage. Firstly, the implementation methods are explained and then the results are shown and discussed.

8.1. Method

8.1.1. Decoupling dual stage system using feedforward

The dual stage MIMO system is decoupled using feedforward action as in [42]. In this approach cross-coupling is viewed as a source of known disturbance forces. It is explained in for instance [43] that known disturbances can be corrected for, using feedforward control.

Let the transfer functions for i-th input $U_i(s)$ to j-th output be defined as $G_{ji}(s)$. Because of coupling, j-th input $U_j(s)$ also has a contribution to output $Y_i(s)$ as follows:

$$Y_i(s) = G_{ii}(s)U_i(s) + G_{ij}(s)U_j(s) \tag{8.1}$$

The decoupling feedforward transfer function $G_{\mathrm{FF}}^{ji}(s)$ is chosen such that it cancels the second term in (8.1). It is defined as:

$$G_{\mathrm{FF}}^{ji}(s) = -G_{ii}^{-1}(s)G_{ij}(s). \tag{8.2}$$

The block diagram of this decoupling control method can be found in figure 8.1.

8.1.2. Trajectory planning

Fourth-order trajectory planning is applied for computing a smoothed trajectory using [41]. Restrictions on maximal allowed velocity, acceleration and the higher order derivatives: jerk and snap, are used in generating a motion profile. In the same paper, a fourth-order feedforward is suggested for improving tracking error. This feedforward boils down to an inverse of the plant transfer function at DC inputs. As was explained in section 2, an inverse plant DC gain has to be used to avoid limit cycles. So this feedforward suffices as a step-regulation measure assuming the model parameters are known and accurate.

The feedforward controller is implemented as in figure 8.2.

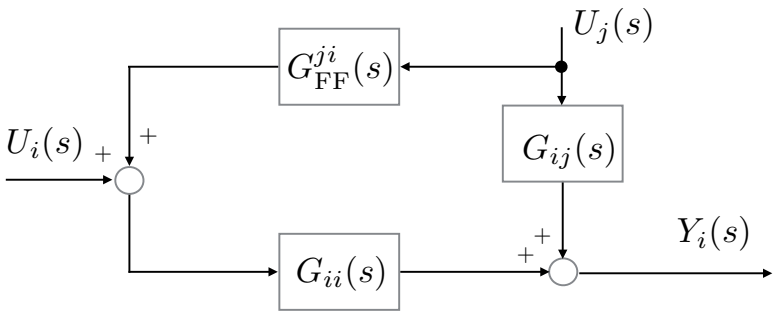

Figure 8.1: Block diagram showing decoupling feedforward. $U_i(s)$ is the input given to G_{ii}. Due to crosstalk, input $U_j(s)$ to G_{jj} also contributes to output $Y_i(s)$. Feedforward controller $G_{FF}^{ji}(s)$ compensates and elevates this contribution.

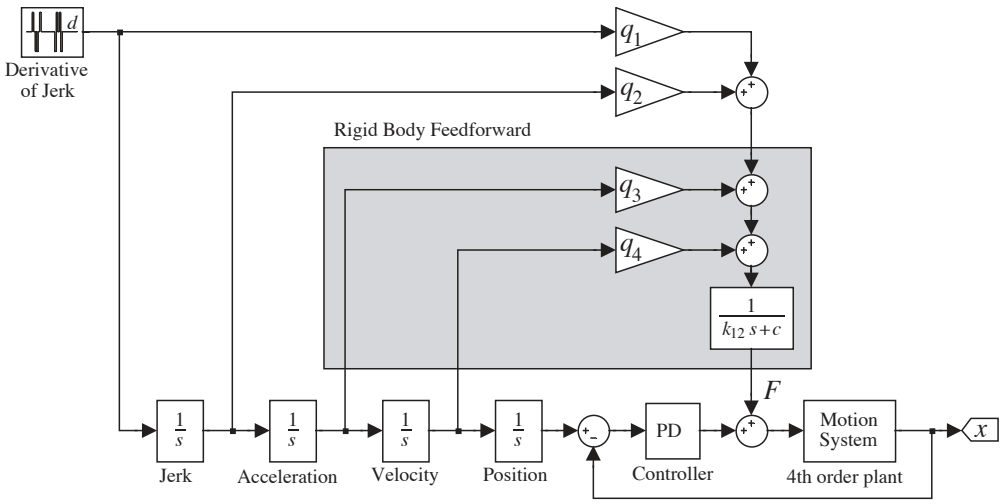

Figure 8.2: Fourth-order feedforward control. Image courtesy of [41]. All continuous-time integrators are replaced for discrete-time integrators. Filter before F is replaced by a discretized filter.

8.1.3. Master/slave configuration

In a master/slave configuration of the MIMO system a reference signal is given for one of the outputs to track and the other outputs have to follow. A master/slave configuration for a 2x2-MIMO system is shown in figure 8.3. This MIMO system $G(s)$ is decoupled into $G_1(s)$ and $G_2(s)$. In this figure $C_1(s)$ is the master controller, as reference signal r is given to $G_1(s)$ to follow. $C_2(s)$ is the slave controller. The second output x_2 is steered to a value such that the error between master and slave becomes zero.

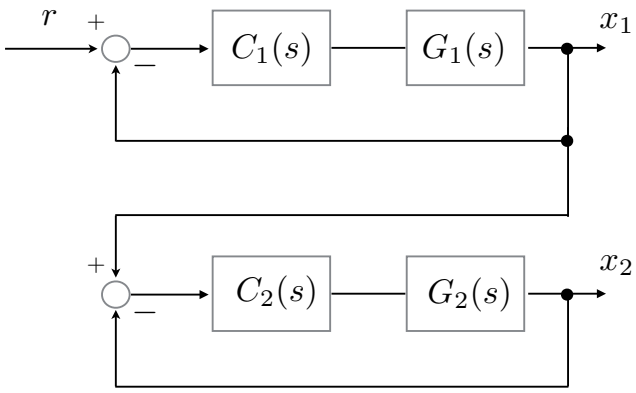

Figure 8.3: Master-slave control scheme. $G_1(s)$ and $G_2(s)$ are the plants to be controlled, $C_1(s)$ is the master controller and $C_2(s)$ is the slave controller.

8.2. Result

8.2.1. Simulated open-loop response

The simulated open-loop response for a CRONE-1 lag-lead reset controller $\gamma = 0$ and varying p on the fine stage plant is shown in figure 8.4. For these open-loop responses, bandwidth and phase margin are shown in table 8.1. Although bandwidth is slightly reduced, it can be seen that open-loop gain at low frequencies increased and gain at high frequencies has reduced. Additionally, similar phase margin has been maintained (maximum reduction of 1.2 degrees). This shows better performance for CRONE-1 lag-lead reset compared to linear CRONE-1 for the same margin.

Table 8.1: Bandwidth and phase margin for CRONE-1 lag-lead reset controller with $\gamma = 0$ on fine stage plant.

p	Bandwidth (Hz)	Phase margin (degree)
1	150.1	52.9
0.5	130.7	51.6
0	124.8	51.7

8.2.2. Practical result

An input-shaped fourth-order triangular wave signal is chosen as a reference with scanning speed of 75 mm/s, maximal acceleration of 0.25 m/s^2 and peak-to-peak distance of 2 cm. In the dual stage the master/slave configuration is used, where the fine stage controller acts as the master and the coarse stage controller acts as a slave. The coarse stage is controlled using a CRONE-2 controller with parameters as shown

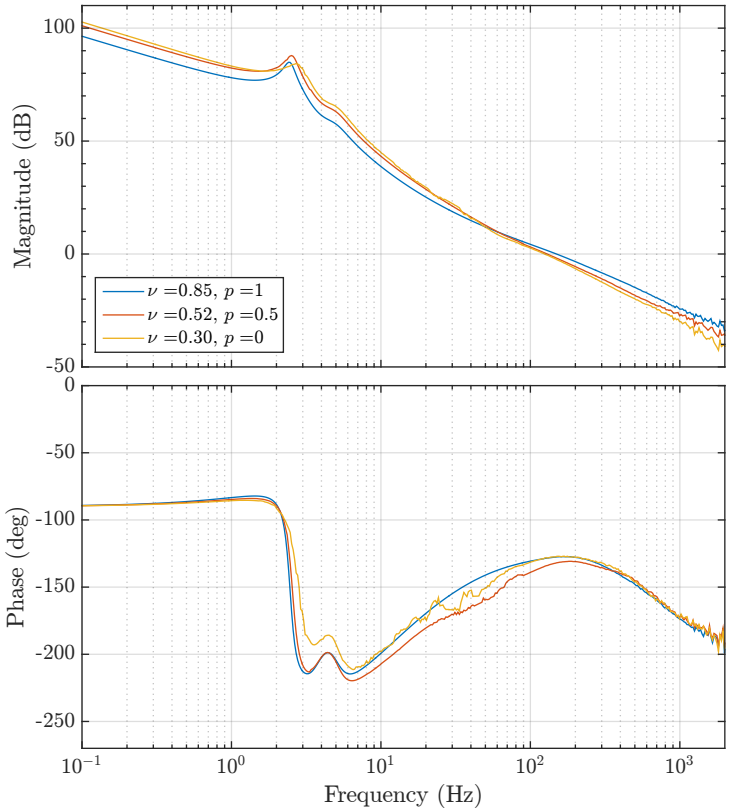

Figure 8.4: Simulated open-loop response for fine stage $H_{22}(s)$ and CRONE-1 lag-lead reset controller with parameters given in table 8.3.

in table 8.2. The CRONE-1 lag-lead reset controller parameters implemented on the fine stage are enlisted in table 8.3.

Table 8.2: Parameter values for coarse stage CRONE-2 controller

Symbol	Parameter	Value
PM	phase margin	50°
ω_{cg}	bandwidth	80 Hz
ω_b	lag corner frequency	10 Hz
ω_h	lead corner frequency	640 Hz
ω_I	integrator corner frequency	6.67 Hz
ω_F	low-pass filter corner frequency	960 Hz
n_I	integrator order	2
n_F	low-pass filter order	3

The output, error and control input to the fine stage are shown in figure 8.5 with

Table 8.3: Parameter values for fine stage CRONE-1 lag-lead reset controller

Symbol	Parameter	Value
PM	phase margin	55°
ω_{cg}	bandwidth	150 Hz
ω_b	lag corner frequency	18.75 Hz
ω_h	lead corner frequency	1200 Hz
ω_I	integrator corner frequency	12.5 Hz
ω_F	low-pass filter corner frequency	1800 Hz
n_I	integrator order	1
n_F	low-pass filter order	1
γ	reset fraction	0

RMS errors as shown in table 8.4.

It can be seen that the RMS error is reduced from 929.8 nm to 443.7 nm for full reset with respect to the linear controller. This is in accordance with results obtained in previous chapters. $p = 0.5$ gives a reduction of RMS error to 540.3 nm. It can be seen that the control input peaks slightly decrease for $p = 0.5$ compared to the full-reset case.

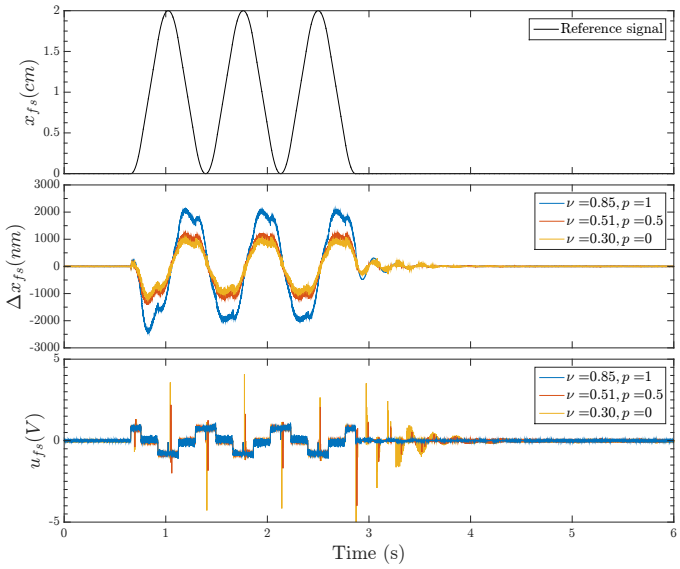

Figure 8.5: CRONE-1 lag-lead reset triangular scanning motion tracking for $\gamma = 0$ and varying p.

Table 8.4: RMS values tracking error for CRONE-1 lag-lead reset $\gamma = 0$ and varying p.

p	RMS (nm)
1	929.8
0.5	540.3
0	443.7

9 Toolbox

In this chapter, the CRONE reset control structure that is computed with the developed toolbox in MATLAB/ Simulink is explained. Additionally, a set of guidelines for CRONE reset control design is given. This chapter is written as a quick-start guide for future projects.

9.1. Installation

1. Double click `CRONE reset toolbox.mlappinstall` to install toolbox.
2. Click CRONE reset toolbox under the *App*-tab in MATLAB to include all m-files and slx-files to search path.

9.2. Overview

The toolbox contains following functions:

- `crone1reset.m`: computes First Generation CRONE controller as a continuous time state-space model.
- `crone2reset.m`: computes Second Generation CRONE controller as a continuous time state-space model.
- `openloopTSDF.m`: runs `GenerateDescribingFunction.slx` and computes describing function of complementary sensitivity $T(j\omega)$, sensitivity $S(j\omega)$ and generates the open-loop response as a pointwise division of the two.
- `croneresetexample.m`: shows an example control design of digital CRONE-1 reset and CRONE-2 reset. Defines discrete state-space matrices used in the CRONE reset control state-space block.
- `zz.m`: computes the Oustaloup approximated fractional lead-lag-/lag-lead filter.

and following Simulink models:

- `CRONEresetlib.slx`: Library that contains a subsystem block of a discrete reset state-space system. This block is used for discrete CRONE controller and can be dragged in your own Simulink file.

- `GenerateDescribingFunction.slx`: Generates the describing function of complementary sensitivity function $T(j\omega)$ and sensitivity function $S(j\omega)$. From this the open-loop response can be approximated.

9.3. Digital controller implementation in Simulink

The generalized state-space model of the combined reset- and non-reset controller is discretized and implemented in Simulink. The corresponding impulsive differential equations are as in equation 5.1. The corresponding Simulink model is depicted in figure 9.1. A subsystem is created of this model and it can be found in the CRONE Reset Toolbox library. An additional shift operator 'Delay2' is added to avoid algebraic loops.

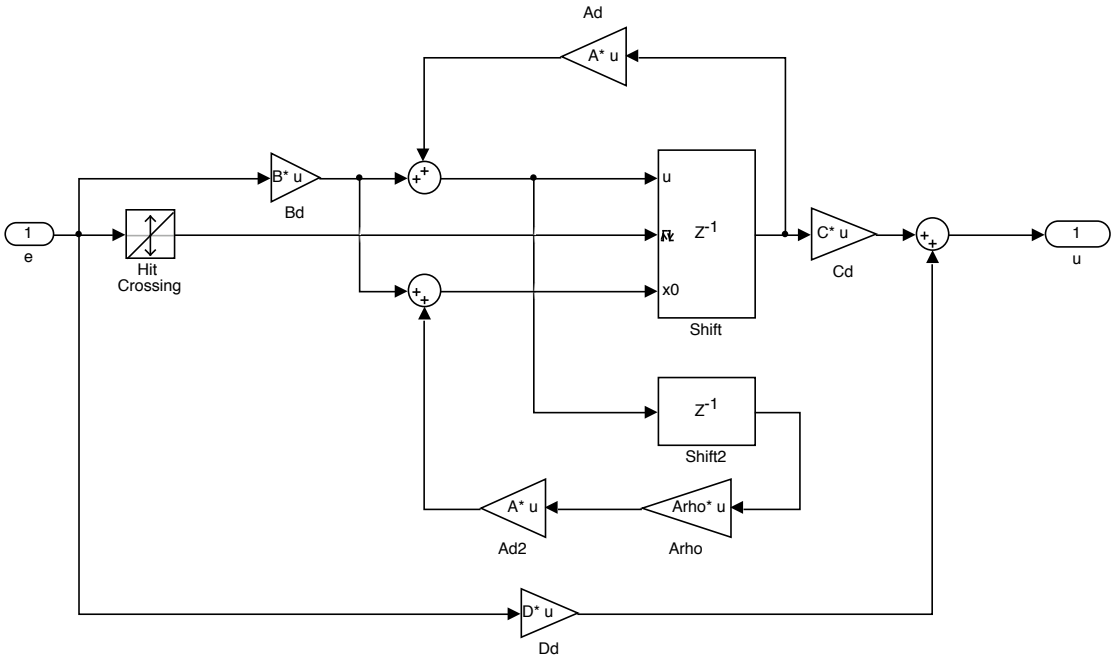

Figure 9.1: Diagram showing discrete implementation of the CRONE reset controller in Simulink.

9.4. Design considerations

9.4.1. Describing function from Simulink model

Discrepancy simulated describing function direct open-loop and using closed-loop results

As discussed in 5 discrepancy exists between simulated describing function of the open-loop response when using Simulink model in figure 5.2 for direct approximation

of the open-loop response and the open-loop response computed through division of PSDs using (5.9). It was shown in previous section that the latter corresponded well with practical measurements. We hypothesize that closed-loop performance cannot be accurately derived from open-loop behaviour for a non-linear reset controller, since linear fundamental restrictions do not apply.

Effect of sampling time on amount of reset phase lead

Because it was observed that limited sampling frequency negatively affected the amount of reset phase lead, the maximal sampling frequency that was possible on the experimental set-up, namely 20kHz, was used for all experiments. Sampling time therefore is an important factor to take into account.

9.4.2. Inverse plant alternatives

Because uncertainties between identified plants and real system always exist, difficulties may arise when taking plant inverse. The result of mismatches of resonance frequency and Q-factor to the open-loop response can be found in figure 9.2. For the open-loop response a -2 slope across all frequencies is taken for simplicity. If there are resonance peaks present before bandwidth, it is wise to avoid dips in the open-loop, otherwise the system will have lesser rejection of disturbance and worse reference tracking. For resonance peaks after bandwidth it is preferable to take measures against peaks in open-loop that may reduce gain margin.

To limit complications some measures can be taken, these will be discussed below.

Resonance frequency mismatch

To limit the dips in the open-loop response, the Q-factor of the plant resonance can be taken lower. After bandwidth to limit peaks, the Q-factor can be taken higher, or the range of the peak in identified plant can be taken wider.

Q-factor mismatch

If the Q-factor is taken too small, a peak will be visible in the open-loop response. If the Q-factor is taken too large, a dip will occur in the open-loop response. Too avoid dips a smaller Q-factor can be taken than identified as a precaution. After bandwidth, in order to avoid peaks a larger Q-factor can be taken.

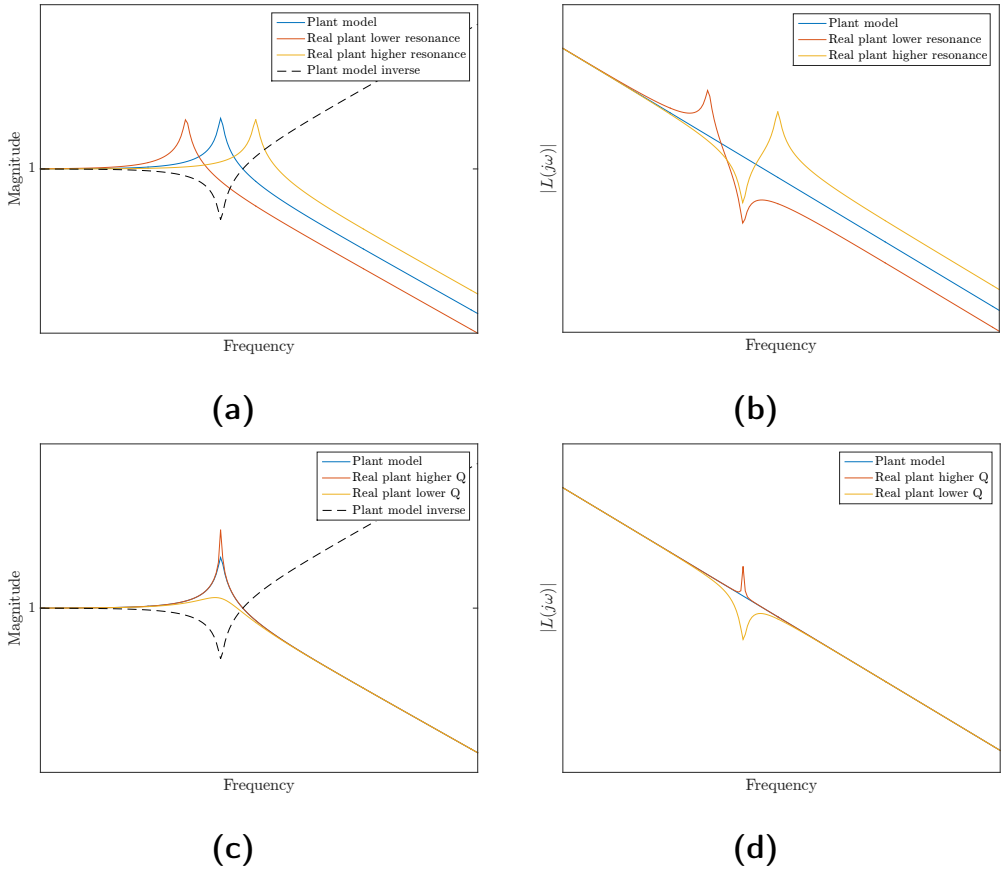

Figure 9.2: Results of mismatch in (a) resonance frequency and (b) its effect on open-loop. In (c) mismatch in Q-factor is shown and (d) the effect on open-loop.

10 Conclusion

10.1. General conclusion

General design rules for CRONE reset control have been developed in this thesis. Using describing function analysis, the reset phase lead is approximated and used for achieving a better open-loop shape. The reset phase lead has been derived and used for modification of existing CRONE control design rules.

Within the project three different control strategies have been investigated: integrator reset, lag reset and lead-lag/lag-lead reset. For these controllers, a two-degree-of-freedom non-linearity tuning CRONE reset structure has been proposed. This control structure has been successfully designed digitally within a MATLAB/Simulink environment and implemented on a Lorentz-actuated (dual) precision stage via a dSPACE DS1103 interface. For the implemented controllers sufficient quadratic stability has been satisfied using the H_β-condition. A MATLAB toolbox has been created for the CRONE reset control methods which can be used for further (CRONE) reset control development.

Frequency domain identification methods have been used to identify complementary sensitivity-, sensitivity function and open-loop response. The proposed open-loop simulation method using closed-loop simulation results corresponded well with experimental results. With this simulation method it was also observed that reducing sampling frequency has malignant effects on the amount of achieved reset phase lead. From both simulated open-loop response and preliminary time domain results for reference-tracking and disturbance rejection, it was shown that the lag-lead reset approach was most promising compared to integrator reset and lag-reset. For the discretized CRONE lag-lead reset controller, more reset phase lead was achieved in these simulations, whereas the discretized CRONE-integrator reset and CRONE-lag reset showed less phase. This is hypothesized to be caused by increase of reset instants when applying negative feedback and closing the loop. This hypothesis requires further research.

Using CRONE-1 lag-lead reset and CRONE-2 lag-lead reset together with the developed design rules, it was shown that in general better performance can be achieved while maintaining similar phase margins. As such, relief from Bode's gain-phase relation has been accomplished. Analysis of the complementary sensitivity function showed decrease of both peak and high frequency transfer. This portrays some relief from waterbed effect. Noise reduction between 1.79 dB and 3.93 dB have been achieved at distinct frequencies above bandwidth for CRONE-1 lag-lead reset- and

CRONE-2 lag-lead reset control. In measured open-loop response the improvement of noise attenuation is smaller than expected. This could be due to the hypothesis raised in previous paragraph: namely, a decrease of loop gain as a consequence of increase of reset instants when closing control loop. Further research is needed . Additionally, further investigation of CRONE reset control behaviour to disturbances should be done. It was observed that secondary peaks were present increasing non-linearity to the system in the presence of input disturbances, which could negatively affect settling time. Moreover, the CPSD results of position displacement for Gaussian disturbances, comparing CRONE reset control to linear CRONE, were inconclusive.

In time domain reference tracking of a fourth-order input-shaped reference signal (with second-order- and fourth-order feedforward for fine stage configuration and dual stage configuration respectively) CRONE reset control showed improvement compared to linear CRONE. In the individual fine stage configuration, RMS errors decreased for both triangular wave and step reference. In triangular wave scanning with peak-to-peak amplitude of 400 µm, RMS error was reduced from 22.10 nm to 17.92 nm when going from linear CRONE-1 to CRONE-1 lag-lead reset with $p = 0$ and $\gamma = 0.5$. RMS error from linear CRONE-2 to CRONE-2 lag-lead reset with similar p and γ, reduced from 70.74 nm to 43.63 nm. For step reference-tracking similar results were observed. RMS error decreased from 13.04 nm to 9.51 nm for CRONE-1 lag-lead reset and from 18.20 nm to 13.11 nm for CRONE-2 lag-lead reset. In the decoupled dual stage, tracking performance of a linear CRONE controller has been investigated using a triangular scanning reference. In both cases the same CRONE-2 controller with a bandwidth of 80 Hz and phase margin of 55° was applied to the coarse stage. On the fine stage a CRONE-1 lag-lead controller was applied with a bandwidth of 150Hz and a phase margin of 55°. RMS error for a triangular scanning wave with maximal acceleration of 0.25 m/s^2 and maximal velocity of 75 mm/s over a stroke of 2 cm peak-to-peak, was reduced from 929.8 nm to 443.7 nm.

10.2. Recommendations

Taking into account several topics within this research, few recommendations are presented which could contribute to further development of CRONE reset control, fractional reset control and reset control in general.

10.2.1. Use cases for describing function simulations

It was observed that the proposed simulation method of open-loop describing function corresponded well to practical results. This can be exploited in CRONE reset control design: reset phase lead from simulation can be used in calculation of fractional order ν instead of the algebraically derived reset phase lead. In this manner, reduction as a result of discretization can be taken into account. Furthermore, the simulation method can be used for general reset controllers to predict practical system behaviour.

In light of the above it would be good to have a faster and more efficient simulation method. At the moment the simulations are ran at a range of frequencies for three times the period, this means that especially for lower frequencies the simulation is very slow.

10.2.2. Higher-order describing function analysis

Furthermore it might be interesting to extend the describing function analysis to higher order. At the moment the first Fourier coefficient of a Fourier series is used to approximate describing function. The filtered practical results correspond well but also here higher harmonics are disregarded. Including higher-order Fourier coefficients might help improving our understanding of higher harmonic behaviour in reset control systems.

10.2.3. Sampling frequency

Maximum sampling frequency of 20 kHz could be implemented on the set-up. This is very high compared to practical required bandwidths. Therefore it is interesting to investigate whether the minimum sampling frequency can be reduced. In the lag-lead reset controllers more phase lead was achieved then calculated using the analytical phase lead formula. Here for example some reduction in sampling frequency is allowed to decrease reset phase lead to the desired amount.

10.2.4. Lag-lead reset element

Additionally, a new reset element could be proposed alongside common reset elements such as the Clegg integrator and FORE. From the retrieved results in this thesis, it was observed that the lag-lead reset filter provided sufficient phase lead even under influence of sampling, whereas this was not achieved resetting integrator or lag filter part of the transfer function.

Bibliography

[1] Ø. N. Dahl. (2014). Learn what an integrated circuit does to your circuit, [Online]. Available: https://www.build-electronic-circuits.com/integrated-circuit/.

[2] J. Sabatier, P. Lanusse, P. Melchior, and A. Oustaloup, *Fractional Order Differentiation and Robust Control Design: CRONE, H-infinity and Motion Control*. Springer Publishing Company, Incorporated, 2015.

[3] A. Baños and A. Barreiro, *Reset control systems*. Springer Science & Business Media, 2011.

[4] C. Schwartz and R. Gran, "Describing function analysis using MATLAB and Simulink", *IEEE Control Systems*, vol. 21, no. 4, pp. 19–26, 2001.

[5] A. Baños, J. Carrasco, and A. Barreiro, "Reset times-dependent stability of reset control systems", *IEEE Transactions on Automatic Control*, vol. 56, no. 1, pp. 217–223, 2011.

[6] L. Zaccarian, D. Nesic, and A. R. Teel, "Set-point stabilization of SISO linear systems using first order reset elements", in *2007 American Control Conference*, 2007, pp. 5808–5809.

[7] R. A. Z. Daou, X. Moreau, and F. Christophy, "Temperature control of a finite diffusive interface medium applying CRONE second generation", in *Advances in Computational Tools for Engineering Applications (ACTEA), 2016 3rd International Conference on*, IEEE, 2016, pp. 26–31.

[8] J. Sabatier, P. Lanusse, B. Feytout, and S. Gracia, "CRONE control based anti-icing/deicing system for wind turbine blades", *Control Engineering Practice*, vol. 56, pp. 200 –209, 2016.

[9] X. Moreau, A. Rizzo, and A. Oustaloup, "Application of the CRONE control-design method to a low-frequency active suspension system", *International Journal of Vehicle Autonomous Systems*, vol. 7, no. 3/4, p. 172, 2009.

[10] R. A. Z. Daou, X. Moreau, and C. Francis, "Control of hydro-electromechanical system using the generalized PID and the CRONE controllers", *IFAC Proceedings Volumes*, vol. 44, no. 1, pp. 15037 –15 042, 2011, 18th IFAC World Congress.

[11] A. Oustaloup, B. Mathieu, and P. Lanusse, "The CRONE control of resonant plants: Application to a flexible transmission", *European Journal of Control*, vol. 1, no. 2, pp. 113 –121, 1995.

[12] B. Feytout, P. Lanusse, J. Sabatier, and S. Gracia, "Robust CRONE design for a variable ratio planetary gearing in a variable speed wind turbine", *Asian Journal of Control*, vol. 15, no. 3, pp. 806–818, 2013.

[13] V. Pommier-Budinger, Y. Janat, D. Nelson-Gruel, P. Lanusse, and A. Oustaloup, "CRONE control of a multivariable lightly damped plant", in *MELECON 2008 - The 14th IEEE Mediterranean Electrotechnical Conference*, 2008, pp. 54–60.

[14] M. Moze, J. Sabatier, and A. Oustaloup, "Air-fuel ratio control of an internal combustion engine using CRONE control extended to LPV systems", in *New Trends in Nanotechnology and Fractional Calculus Applications*. Dordrecht: Springer Netherlands, 2010, pp. 71–86.

[15] J. Sabatier, A. Oustaloup, A. G. Iturricha, and F. Levron, "CRONE control of continuous linear time periodic systems: Application to a testing bench", *ISA Transactions*, vol. 42, no. 3, pp. 421 –436, 2003.

[16] S. H. HosseinNia, R. Ghaderi, A. Ranjbar N, M. Mahmoudian, and M. S., "Sliding mode synchronization of an uncertain fractional order chaotic system", *Computers & Mathematics with Applications*, vol. 59, no. 5, pp. 1637 –1643, 2010, Fractional Differentiation and Its Applications.

[17] S. H. HosseinNia, I. Tejado, and B. M. Vinagre, "Basic properties and stability of fractional-order reset control systems", in *Control Conference (ECC), 2013 European*, IEEE, 2013, pp. 1687–1692.

[18] B. M. Vinagre, I. Petráš, I. Podlubny, and Y. Q. Chen, "Using fractional order adjustment rules and fractional order reference models in model-reference adaptive control", *Nonlinear Dynamics*, vol. 29, no. 1, pp. 269–279, 2002.

[19] O. Altet, X. Moreau, M. Moze, P. Lanusse, and A. Oustaloup, "Principles and synthesis of hydractive CRONE suspension", *Nonlinear Dynamics*, vol. 38, no. 1, pp. 435–459, 2004.

[20] P. Lanusse and J. Sabatier, "PLC implementation of a CRONE controller", *Fractional Calculus and Applied Analysis*, vol. 14, no. 4, p. 505, 2011.

[21] B. M. Vinagre, I. Podlubny, A. Hernandez, and V. Feliu, "Some approximations of fractional order operators used in control theory and applications", *Fractional calculus and applied analysis*, vol. 3(3), pp. 231–248, 2000.

[22] Y. Li, G. Guo, and Y. Wang, "Reset control for midfrequency narrowband disturbance rejection with an application in hard disk drives", *IEEE Transactions on Control Systems Technology*, vol. 19, no. 6, pp. 1339–1348, 2011.

[23] H. Li, C. Du, and Y. Wang, "Discrete-time H_2 optimal reset control with application to HDD track-following", in *2009 Chinese Control and Decision Conference*, 2009, pp. 3613–3617.

[24] L. Hazeleger, M. Heertjes, and H. Nijmeijer, "Second-order reset elements for stage control design", in *2016 American Control Conference (ACC)*, 2016, pp. 2643–2648.

[25] J. Zheng, Y. Guo, M. Fu, Y. Wang, and L. Xie, "Development of an extended reset controller and its experimental demonstration", *IET Control Theory & Applications*, vol. 2, 866–874(8), 10 2008.

[26] M. A. Davó and A. Baños, "Reset control of a liquid level process", in *2013 IEEE 18th Conference on Emerging Technologies Factory Automation (ETFA)*, 2013, pp. 1–4.

[27] F. Perez, A. Baños, and J. Cervera, "Periodic reset control of an in-line pH process", in *ETFA 2011*, 2011, pp. 1–4.

[28] S. J.L. M. Van Loon, K. G. J. Gruntjens, M. F. Heertjes, N. Van de Wouw, and W. P.M. H. Heemels, "Frequency-domain tools for stability analysis of reset control systems", *Automatica*, vol. 82, pp. 101–108, 2017.

[29] H. Li, C. Du, and Y. Wang, "Optimal reset control for a dual-stage actuator system in HDDs", *IEEE/ASME Transactions on Mechatronics*, vol. 16, no. 3, pp. 480–488, 2011.

[30] J. Carrasco, A. Baños, and A. van der Schaft, "A passivity-based approach to reset control systems stability", *Systems & Control Letters*, vol. 59, no. 1, pp. 18 –24, 2010.

[31] S. H. HosseinNia, I. Tejado, D. Torres, B. M. Vinagre, and V. Feliu, "A general form for reset control including fractional order dynamics", *IFAC Proceedings Volumes*, vol. 47, no. 3, pp. 2028–2033, 2014.

[32] N. Saikumar and S. H. HosseinNia, "Generalized fractional order reset element (GFrORE)", in *9th European Nonlinear Dynamics Conference (ENOC)*, 2017.

[33] S. H. HosseinNia, I. Tejado, and B. M. Vinagre, "Fractional-order reset control: Application to a servomotor", *Mechatronics*, vol. 23, pp. 781–788, 2013.

[34] S. H. HosseinNia, I. Tejado, B. M. Vinagre, and Y. Chen, "Iterative learning and fractional reset control", in *Volume 9: 2015 ASME/IEEE International Conference on Mechatronic and Embedded Systems and Applications*, ASME, 2015.

[35] Y. Guo, Y. Wang, and L. Xie, "Frequency-domain properties of reset systems with application in hard-disk-drive systems", *IEEE Transactions on Control Systems Technology*, vol. 17, no. 6, pp. 1446–1453, 2009.

[36] Janssen Precision Engineering. (2017). Flexure guiding – 2 leaf springs in parallel, [Online]. Available: http://www.janssenprecisionengineering.com/page/flexure-guiding-2-leaf-springs-in-parallel/.

[37] B. Joziasse, "Nanometer precision scanning dual stage with reduced joule heating in the fine stage actuator", Master's thesis, Delft University of Technology, 2017.

[38] Aerotech, Inc. (n.d.). ABL1000 Series product sheet, [Online]. Available: https://www.aerotech.com/media/440262/abl1000.pdf.

[39] J. Carrasco and E. M. Navarro-López, "Towards $\mathcal{L}_2$-stability of discrete-time reset control systems via dissipativity theory", *Systems & Control Letters*, vol. 62, no. 6, pp. 525 –530, 2013.

[40] Mechatronics Academy B.V., *Motion control tuning - module 6: FRF measurements*, n.d.

[41] P. Lambrechts, M. Boerlage, and M. Steinbuch, "Trajectory planning and feedforward design for electromechanical motion systems", *Control Engineering Practice*, vol. 13, no. 2, pp. 145–157, 2005.

[42] G. A. Dumont, *Decoupling control of MIMO systems*, Department of Electrical and Computer Engineering University of British Columbia, 2011.

[43] R. M. Schmidt, G. Schitter, A. Rankers, and J. Van Eijk, *The Design of High Performance Mechatronics: High-Tech Functionality by Multidisciplinary System Integration*, 2nd. Amsterdam, The Netherlands, The Netherlands: IOS Press, 2014.

[44] K. Aström and R. Murray, *Feedback Systems: An Introduction for Scientists and Engineers*. Princeton University Press, 2010, pp. 315–317.

A

Background: Linear Feedback Control

This appendix chapter provides background information about linear feedback control. Stability margins are discussed and loop shaping fundamentals are explained.

A.1. Introduction

The main purpose of adding a controller to a system is to control the system output to prescribed reference values. Using feedback, the error between output and reference value is used to compute a control input that decreases the error to zero. A control feedback diagram can be found in figure A.1. $G(s)$ is the system or plant that is controlled, $C(s)$ is the feedback controller giving control input u to the system to get system output y to follow reference value r. e is the error with $e = y - r$. The system is affected by disturbance signal d and noise signal n.

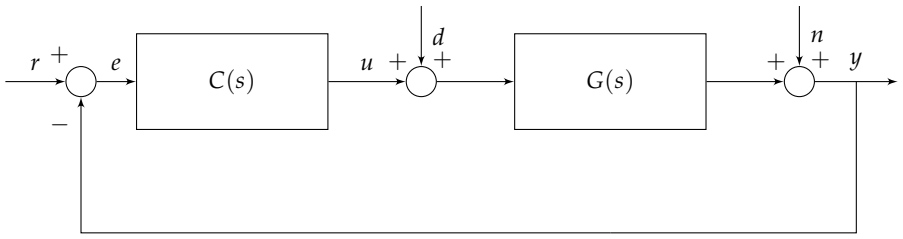

Figure A.1: Feedback control diagram

The transfer of external signals r, d and n to the output y can be described by using a set of four transfer functions given below, also referred to as "*Gang of Four*" [44].

$$S(s) = \frac{Y(s)}{N(s)} = \frac{1}{1 + G(s)C(s)}, \quad \text{sensitivity function,}$$

$$T(s) = \frac{Y(s)}{R(s)} = \frac{G(s)C(s)}{1 + G(s)C(s)}, \quad \text{complementary sensitivity function,}$$

$$G(s)S(s) = \frac{Y(s)}{D(s)} = \frac{G(s)}{1 + G(s)C(s)}, \quad \text{load sensitivity function,}$$

$$C(s)S(s) = \frac{U(s)}{N(s)} = \frac{C(s)}{1 + G(s)C(s)}, \quad \text{noise sensitivity function}$$

A.2. Stability margins

Methodologies exist for controller synthesis using a frequency domain approach. In these methods, Bode plot, Nyquist plot and Nichols plot act as useful tools for visualizing and evaluating system behaviour. In a Bode plot the magnitude and phase of the transfer function are shown as a function of frequency. In a Nyquist plot the real part of the transfer function is plot against its imaginary part. Finally, a Nichols plot displays the magnitude of the transfer function against its phase. These plots can be used to visualize stability margins.

The stability margins to quantitatively describe performance are:

- Phase margin: how much phase can be subtracted to destabilize the system.
- Gain margin: how much gain can be added to make the system go unstable.
- Modulus margin: how much uncertainty makes the system unstable.
- Time-delay margin: how much time-delay makes the system unstable.

Stability margins can be visualized in the Bode- (figure A.2), Nyquist- (figure A.3) and Nichols (A.4) plots of the open loop of the system, in which the open loop is given by $L(s) = C(s)G(s)$. An exception is the modulus margin in the Bode plot of figure A.2, that is visualized with the sensitivity function of the system rather than the open loop.

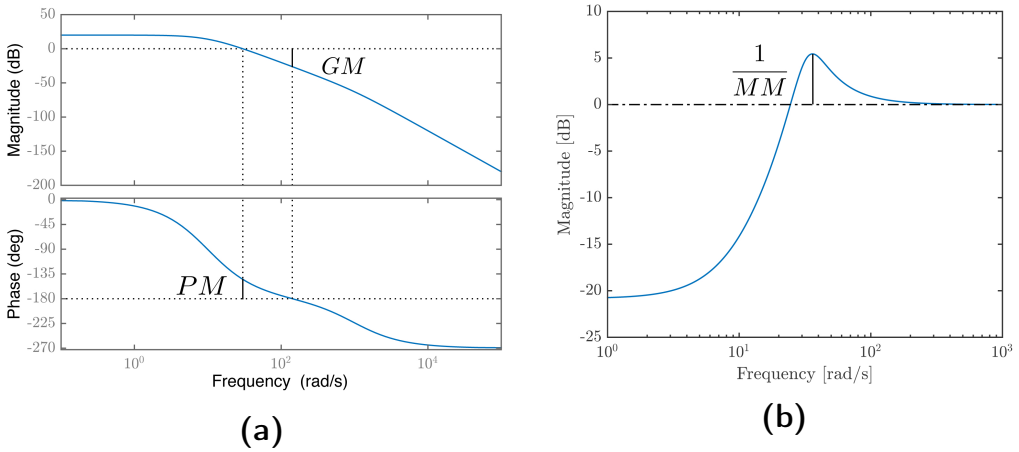

Figure A.2: a)Example Bode plot for $L(j\omega) = C(j\omega)G(j\omega)$. PM is the phase margin, GM is the gain margin. b) Example Bode magnitude plot for sensitivity function $S(j\omega)$ in which MM is the modulus margin.

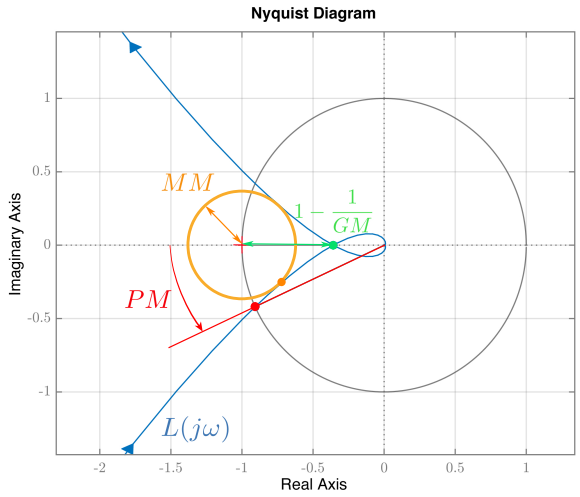

Figure A.3: Nyquist plot with stability margins: GM, PM and MM being the gain margin, phase margin and modulus margin respectively.

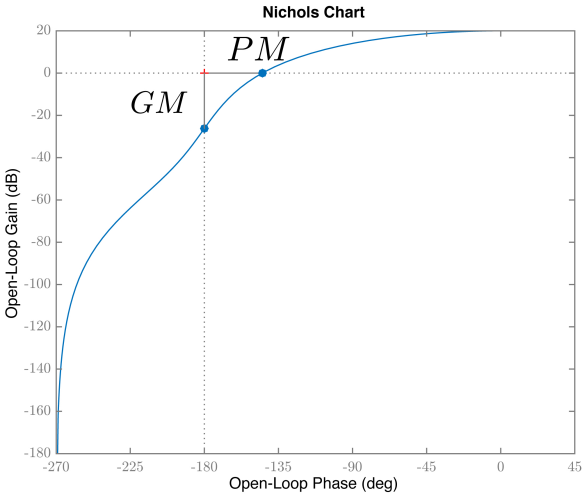

Figure A.4: Nichols plot showing stability margins: gain margin GM and phase margin PM.

A.3. Loop shaping

The idea of loop shaping is based on the fact that by changing the open loop $L(s) = C(s)G(s)$, reference-tracking, noise attenuation and disturbance rejection properties of the closed-loop system can be altered and stability margins are adjusted.

An open-loop response ideally has high open-loop gain at low frequencies and

low open-loop gain at high frequencies. This can be reasoned using the sensitivity function and complementary sensitivity functions given in section **??**. The noise transfer in a system can be described by its sensitivity function and the transfer from reference to output by its complementary sensitivity function. For effective reference tracking and proper noise rejection, the open-loop gain at lower frequencies should be very high ($|L(j\omega)| \to \infty$) such that $\frac{Y(s)}{R(s)} = |T(j\omega)| \approx 1$ and $\frac{Y(s)}{N(s)} = |S(j\omega)| \ll 1$. Contrarily at high frequencies the open-loop gain should be low ($|L(j\omega)| \ll 1$) to stop tracking such that $|T(j\omega)| \ll 1$.

An ideal Bode open-loop can be approximated with an ν-order integrator of the form [2]:

$$L = \left(\frac{\omega_{cg}}{s}\right)^{\nu} \tag{A.1}$$

in which ω_{cg} is the bandwidth frequency. This loop shape satisfies high gain at low frequencies and low gain at high frequencies as described above.

For a second order plant (mass system) under unity feedback an approximated ideal Bode open-loop would be: $L = \left(\frac{\omega_{cg}}{s}\right)^2$. This open-loop gives zero-phase margin and hence is marginally stable. Phase margin can be increased by adding phase in the frequency band around bandwidth as can be seen in figure A.5 using derivative action:

$$C_D(s) = \frac{1 + \frac{s}{\omega_d}}{1 + \frac{s}{\omega_t}} \tag{A.2}$$

with ω_d and ω_t being the lower and higher corner frequencies of the frequency band in which derivative action $C(s) = s$ is active.

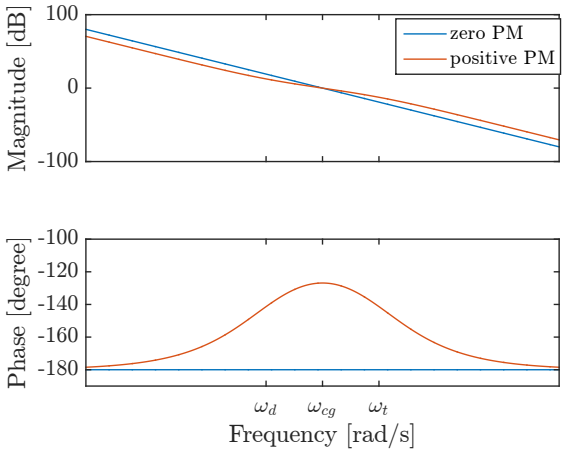

Figure A.5: Open-loop response with and without phase margin. The latter has desired gain behaviour but is marginally stable, former is stable in return for reduced gain behaviour.

B

Derivation first order reset phase lead $\Phi_r(\omega)$

In this appendix chapter first order reset phase lead for a lead-lag-/lag-lead filter in (3.35) is derived from the describing function.

B.1. Describing function formulation

The general describing function of a reset system as defined in [35] is given by:

$$G_{\text{DF}}(j\omega) = C(j\omega I - A)^{-1}B(I + j\Theta_D(\omega)) + D \tag{B.1}$$

in which A, B, C, D are the base state-space matrices and $\Theta_D(\omega)$ is defined as:

$$\Theta_D(\omega) = -\frac{2\omega^2}{\pi}\Delta(\omega)[\Gamma_D(\omega) - \Lambda^{-1}(\omega)] \tag{B.2}$$

The additional phase at cross-over frequency is given by $\Phi_r(\omega_{cg})$, which is calculated from:

$$\Phi_r(\omega) = \angle G_{\text{DF}}(j\omega) - \angle G(j\omega) \tag{B.3}$$

A first order lead-lag-/lag-lead filter has following frequency response:

$$H_{\text{ll}}(j\omega) = \frac{1 + \frac{j\omega}{a}}{1 + \frac{j\omega}{b}} \tag{B.4}$$

where a and b are appropriate corner frequencies.

Then the state space matrices are:

$$\begin{cases} A = -b \\ B = 1 \\ C = \frac{b(a-b)}{a} \\ D = \frac{b}{a} \end{cases} \tag{B.5}$$

The set of equations used in (B.2) for this system is given by:

$$\begin{cases} \Lambda(\omega) = \omega^2 I + A^2 = \omega^2 + b^2 \\ \Delta(\omega) = I + e^{\frac{\pi}{\omega}A} = 1 + e^{-\pi\frac{b}{\omega}} \\ \Delta_D(\omega) = I + A_\rho e^{\frac{\pi}{\omega}A} = 1 + \gamma e^{-\pi\frac{b}{\omega}} \\ \Gamma_D(\omega) = \Delta_D^{-1}(\omega)A_\rho\Delta(\omega)\Lambda^{-1}(\omega) = \frac{\gamma}{1+\gamma e^{-\pi\frac{b}{\omega}}}\frac{1+e^{-\pi\frac{b}{\omega}}}{\omega^2+b^2} \end{cases}$$

B.2. Computation $\Theta_D(\omega)$

Filling the functions above into (B.2) gives:

$$\begin{aligned}
\Theta_D(\omega,b,\gamma) &= -\frac{2\omega^2}{\pi}(1+e^{-\pi\frac{b}{\omega}})\Big(\frac{\gamma}{1+\gamma e^{-\pi\frac{b}{\omega}}}\frac{1+e^{-\pi\frac{b}{\omega}}}{\omega^2+b^2}-\frac{1}{\omega^2+b^2}\Big)\\
&= -\frac{2\omega^2}{\pi}\frac{1+e^{-\pi\frac{b}{\omega}}}{\omega^2+b^2}\Big(\frac{\gamma(1+e^{-\pi\frac{b}{\omega}})}{1+\gamma e^{-\pi\frac{b}{\omega}}}-1\Big)\\
&= \frac{2}{\pi}\frac{1+e^{-\pi\frac{b}{\omega}}}{1+(\frac{b}{\omega})^2}\Big(1-\frac{\gamma(1+e^{-\pi\frac{b}{\omega}})}{1+\gamma e^{-\pi\frac{b}{\omega}}}\Big)\\
&= \frac{2}{\pi}\frac{1+e^{-\pi\frac{b}{\omega}}}{1+(\frac{b}{\omega})^2}\Big(\frac{1+\gamma e^{-\pi\frac{b}{\omega}}}{1+\gamma e^{-\pi\frac{b}{\omega}}}-\frac{\gamma(1+e^{-\pi\frac{b}{\omega}})}{1+\gamma e^{-\pi\frac{b}{\omega}}}\Big)\\
&= \frac{2}{\pi}\frac{1+e^{-\pi\frac{b}{\omega}}}{1+(\frac{b}{\omega})^2}\frac{1-\gamma}{1+\gamma e^{-\pi\frac{b}{\omega}}}
\end{aligned} \tag{B.6}$$

B.3. Describing function of $H_{\text{ll}}(j\omega)$

The describing function of $H_{\text{ll}}(j\omega)$ is $H_{\text{DF,ll}}(j\omega)$, found by substituting state-space matrices from (B.5) in (B.1), simplifies to:

$$\begin{aligned}
H_{\text{DF,ll}}(j\omega) &= \frac{1+j\frac{\omega}{a}+j\Theta_D(\omega,b,\gamma)(1-\frac{b}{a})}{1+\frac{j\omega}{b}}\\
&= \frac{1+\frac{j\omega}{a}}{1+\frac{j\omega}{b}}\Big(1+\frac{j\Theta_D(\omega,b,\gamma)(1-\frac{b}{a})}{1+\frac{j\omega}{a}}\Big)\\
&= \frac{1+\frac{j\omega}{a}}{1+\frac{j\omega}{b}}\Big(\frac{1+(\frac{\omega}{a})^2+\Theta_D(\omega,b,\gamma)(1-\frac{b}{a})\frac{\omega}{a}+j\Theta_D(\omega,b,\gamma)(1-\frac{b}{a})}{1+(\frac{\omega}{a})^2}\Big)\\
&= H_{\text{ll}}(j\omega)\Big(\frac{1+(\frac{\omega}{a})^2+\Theta_D(\omega,b,\gamma)(1-\frac{b}{a})\frac{\omega}{a}+j\Theta_D(\omega,b,\gamma)(1-\frac{b}{a})}{1+(\frac{\omega}{a})^2}\Big)
\end{aligned} \tag{B.7}$$

B.4. Describing function for convex combination structure

$$
\begin{aligned}
H^*_{\mathrm{DF}}(j\omega) &= (1-p)H_{\mathrm{DF,ll}}(j\omega) + pH_{\mathrm{ll}}(j\omega) \\
&= (1-p)H_{\mathrm{ll}}(j\omega)\Big(\frac{1+(\frac{\omega}{a})^2+\Theta_D(\omega,b,\gamma)(1-\frac{b}{a})\frac{\omega}{a}+j\Theta_D(\omega,b,\gamma)(1-\frac{b}{a})}{1+(\frac{\omega}{a})^2}\Big) \\
&\quad + pH_{\mathrm{ll}}(j\omega) \\
&= H_{\mathrm{ll}}(j\omega)\Big(1+(1-p)\frac{\Theta_D(\omega,b,\gamma)(1-\frac{b}{a})\frac{\omega}{a}+j\Theta_D(\omega,b,\gamma)(1-\frac{b}{a})}{1+(\frac{\omega}{a})^2}\Big) \\
&= H_{\mathrm{ll}}(j\omega)\Big(\frac{1+(\frac{\omega}{a})^2+(1-p)\frac{\omega}{a}\Theta_D(\omega,b,\gamma)(1-\frac{b}{a})+j(1-p)\Theta_D(\omega,b,\gamma)(1-\frac{b}{a})}{1+(\frac{\omega}{a})^2}\Big)
\end{aligned}
\tag{B.8}
$$

B.5. Phase lead

Using the result of (B.8), the phase lead for the considered first order lead-lag-/lag-lead filter as a function of frequency, partial reset γ and reset percentage p can be computed with:

$$
\Phi_{r,\mathrm{ll}}(\omega) = \arctan\left(\frac{(1-p)\Theta_D(\omega,b,\gamma)(1-\frac{b}{a})}{1+(\frac{\omega}{a})^2+(1-p)\frac{\omega}{a}\Theta_D(\omega,b,\gamma)(1-\frac{b}{a})}\right) \tag{B.9}
$$

C

Derivation state-space and reset matrix

This appendix chapter shows the derivation of the CRONE reset control state-space description using two system interconnections and derivation of the reset matrix.

C.1. Introduction

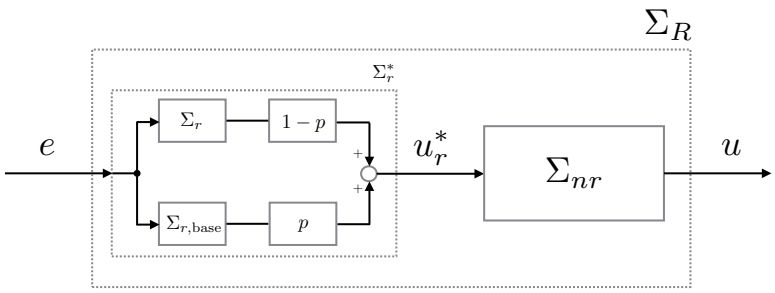

Figure C.1: Block diagram of the CRONE reset controller parts.

In figure C.1 the block diagram of a CRONE reset controller is depicted. The CRONE reset controller with state description Σ_R consists of a reset part Σ_r^* and a non-reset part Σ_{nr}. Furthermore, within the reset part, a convex combination is taken of the reset system and its base linear system. Interconnection of the latter will be handled firstly below.

C.2. Convex combination of the reset controller using parallel interconnection

$$\Sigma_{r,1-p}: \begin{cases} \dot{x}_{r,1-p} = A_r x_{r,1-p} + B_r e, & \text{if } e \neq 0, \\ x_{r,1-p}(t^+) = A_\rho x_{r,1-p}, & \text{if } e = 0, \\ u_{r,1-p} = (1-p)C_r x_{r,1-p} + (1-p)D_r e \end{cases} \tag{C.1}$$

$$\Sigma_{r,p}: \begin{cases} \dot{x}_{r,p} = A_r x_{r,p} + B_r e \\ u_{r,p} = pC_r x_{r,p} + pD_r e \end{cases} \tag{C.2}$$

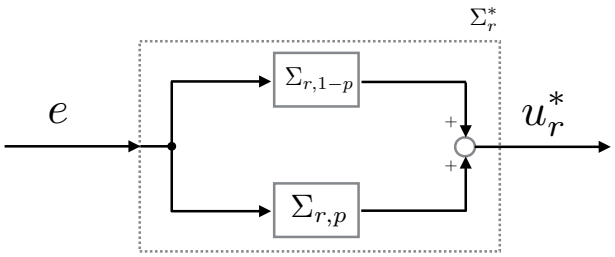

Figure C.2: Block diagram of convex combination structure.

The parallel interconnected system of $\Sigma_{r,1-p}$ and $\Sigma_{r,p}$ gives the following state-space for $\xi = \left[x_{r,1-p}^T, x_{r,p}^T\right]^T$

$$\Sigma_r^* : \begin{cases} \dot{\xi} = \underbrace{\begin{bmatrix} A_r & 0 \\ 0 & A_r \end{bmatrix}}_{\bar{A}} \xi + \underbrace{\begin{bmatrix} B_r \\ B_r \end{bmatrix}}_{\bar{B}} e, & \text{if } e \neq 0, \\ \xi(t^+) = \underbrace{\begin{bmatrix} A_\rho & 0 \\ 0 & I \end{bmatrix}}_{\bar{A}_\rho} \xi, & \text{if } e = 0, \\ u_r^* = \underbrace{\begin{bmatrix} (1-p)C_r & pC_r \end{bmatrix}}_{\bar{C}} \xi + D_r e \end{cases} \tag{C.3}$$

C.3. Series connection reset- and non-reset controller

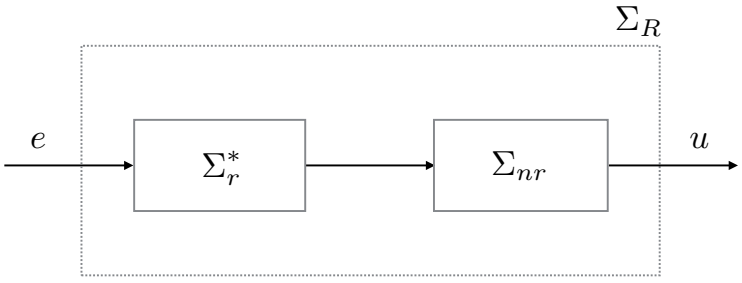

Figure C.3: Block diagram of series interconnection reset- and non-reset part of controller

The state-space system of the non-reset part of the controller is given by:

$$\Sigma_{nr}: \begin{cases} \dot{x}_{nr} = A_{nr}x_{nr} + B_{nr}e \\ u_{nr} = C_{nr}x_{nr} + D_{nr}e \end{cases} \tag{C.4}$$

Then the series interconnection of system Σ_r^* and Σ_{nr} gives:

$$\Sigma_R: \begin{cases} \dot{\phi} = \underbrace{\begin{bmatrix} \bar{A} & 0 \\ B_{nr}\bar{C} & A_{nr} \end{bmatrix}}_{A_R} \phi + \underbrace{\begin{bmatrix} \bar{B} \\ B_{nr}\bar{D} \end{bmatrix}}_{B_R} e, & e \neq 0 \\ \phi(t^+) = \underbrace{\begin{bmatrix} \bar{A}_\rho & 0 \\ 0 & I \end{bmatrix}}_{A_\rho^*} \phi, & e = 0 \\ u_c = \underbrace{\begin{bmatrix} D_{nr}\bar{C} & C_{nr} \end{bmatrix}}_{C_R} \phi + D_{nr}\bar{D} \end{cases} \tag{C.5}$$

where $\phi = [x_{r,1-p}^T, x_{r,p}^T, x_{nr}^T]^T$

The final state-space and reset matrices can be found by substituting equations C.3 in C.5:

$$\begin{cases} A_R = \left[\begin{array}{cc|c} \multicolumn{2}{c|}{\begin{bmatrix} A_r & O \\ O & A_r \end{bmatrix}} & O \\ \hline B_{nr}\begin{bmatrix} (1-p)C_r & pC_r \end{bmatrix} & & A_{nr} \end{array}\right] \\ A_\rho^* = \begin{bmatrix} \bar{A}_\rho & 0 \\ 0 & I \end{bmatrix} \end{cases} \tag{C.6}$$

D

MATLAB code

This appendix chapter presents the MATLAB code used for stability analysis. Two stability conditions have been checked in this thesis: the H_β-condition and the $|\lambda(A_\rho e^{\frac{\pi}{\omega}A_{ol}})|$-condition.

D.1. H_β-condition

```
%--------------------------------------------------------------------------
% Check Hbeta-condition using LMI
%--------------------------------------------------------------------------

% Plant transfer function
load Hindividual

% Compute CRONE-1 reset controller
% Initialize parameters
PM=55;
wcg=200*pi;
N=4;
scale1=8;
scale2=12;
ni=1;
nf=1;

%     p=1:-0.25:0;
p=0.5;
gamma=0.5;

for l=1:length(p)
    % Compute CRONE reset controller
    [Cf,Arho,nu,Lreset,C_r,C_nr] = crone1reset('ll',PM,wcg,N,scale1,scale2,...
        ni,nf,H2,gamma,p(l));


    % Initialize LMI
    % Compute closed loop system
    syscl=feedback(series(Cf,ss(H2)),1);
    Acl=syscl.a;                % Closed loop A-matrix
    A=Acl/norm(Acl);            % Preprocess A-matrix

```

```
34
35      % Initialize dimensions
36      nrho=1;                         % number of controller reset states
37      nrhobar=size(Cf.a,1)-nrho;      % number of controller non-reset states
38      np=size(ss(H2).a,1);            % number of plant states
39
40      % Compute C0 and B0
41      Cp=ss(H2).c;
42      beta=sdpvar(1,1,'full','real');
43      Prho=sdpvar(1,1,'full','real');
44      B0=[zeros(np,nrho);zeros(nrhobar,nrho);ones(nrho,nrho)];
45      C0=[beta*Cp zeros(nrho,nrhobar) Prho];
46      P=sdpvar(size(syscl.a,1),size(syscl.a,1),'symmetric');
47
48      % Solve LMI
49
50      lmi=A'*P+P*A<=0;
51      eps=1e-14;
52      constr=[P>=eps*eye(size(syscl.a,1)), B0'*P==C0];
53      ops=sdpsettings('solver','sedumi','verbose',0);
54
55      F=solvesdp([lmi constr],0,ops);
56
57
58      if F.problem==0
59
60          display(strcat('Solution found for: p=',num2str(p(l))))
61
62      end
63
64  end
```

D.2. $|\lambda(A_\rho e^{\frac{\pi}{\omega}A_{ol}})|$-condition

```
1  %-------------------------------------------------------------------------
2  % |lambda(Arho*exp(pi/w*Aol)|
3  %-------------------------------------------------------------------------
4
5  % Plant transfer function
6  load Hindividual
7  f=logspace(-1,6,1e3);
8
9
10 % Initialize parameters
11 gamma=0.5;
12 p=0.5;
13 N=4;
14 ni=1;
15 nf=1;
```

```
scale1=8;
scale2=12;


for j=1:length(p)

    for k=1:length(gamma)
        % Compute CRONE controller
        [Cf,~,~,~,Cr,Cnr]=crone1reset('ll',55,200*pi,N,scale1,scale2,ni,...
            nf,H2,gamma(k),p(j));

        % Compute open-loop
        Cs=ss(series(Cr,Cnr));
        P=ss(H2);
        L=series(Cs,P);

        n=size(Cs.a,1);          % number of controller states
        m=size(P.a,1);           % number of plant states

        eigenval=zeros(n+m);     % initialize

        % Compute reset matrix
        Arhostar=eye(n);
        Arhostar(1)=gamma(k);
        Arho=blkdiag(Arhostar,eye(2));

        % Calculate eigenvalues
        for i=1:length(f);
            w=2*pi*f(i);
            term=Arho*(expm(pi/w*L.a));

            if sum(sum(isnan(term)))==0;
                eigenval(:,i)=abs(eig(term));
            end
        end

        semilogx(f,eigenval)
        hold on
    end
end

% Plot figure
ylabel('$|\lambda(A_\rho e^{\frac{\pi}{\omega} A_{ol}})|$')
xlabel('Frequency (Hz)')
grid on
set(gca,'YMinorTick','on')
```